Stability and self-repair of amorphous cobalt/nickel oxyhydroxides for electrocatalytic water oxidation investigated by electrochemical protocols combined with X-ray absorption spectroscopy

by

Mohammad Reza Mohammadi

A dissertation submitted to the Department of Physics of

Freie Universität Berlin for the degree of

Dr. rer. nat.

Berlin, March 2019

Stability and self-repair of amorphous cobalt/nickel oxyhydroxides for electrocatalytic water oxidation investigated by electrochemical protocols combined with X-ray absorption spectroscopy

Mohammad Reza Mohammadi

Department of Physics, Freie Universität Berlin

First advisor: Prof. Holger Dau

Second advisor: Prof. Peter Strasser

Date of defense: 2019/05/17

Abstract

Any attractive system for efficient light-driven water splitting needs to involve water-oxidation catalysts, which ideally are based on earth-abundant chemical elements only. Prime candidates are oxides of first-row transition metals, in particular the elements manganese to copper. In 2008, Kanan and Nocera described electrodeposition of an amorphous cobalt-based oxide film (CoCat) in phosphate buffer, which promotes water oxidation in the neutral pH regime and excels by self-healing properties. In this thesis, stability and self-healing of a cobalt catalyst (CoCat), a nickel catalyst (NiCat) and a nickel-iron catalyst (NiFeCat) were investigated at various electrochemical potentials. Cyclic voltammograms were measured every 30 min, to diagnose the catalytic activity and loss in redox-active cobalt ions. Furthermore, X-ray absorption spectroscopy is used for assessment of structural changes at the atomic level.

The optimal electric potential window for having a comparably stable (> 80 %) CoCat sample is 1.1 < V vs. NHE < 1.35, where reasonable activity (> 65 %) is maintained after 24 hours operation in Co-free phosphate buffer (0.1 M KPi, pH 7). On the other hand, operation in Co-contaning buffer results in an almost stable performance (in terms of current density per geometrical surface area), but the film thickness is growing significantly. Thus, self-assembly of CoCat is not well described as self-healing.

Structural analysis of CoCat operated in 20 µmol L^{-1} Co-containing KP_i buffer for 24 hours at catalytic potential (1.3 V vs. NHE) exhibit small, but significant changes in EXAFS spectra because long time operation results in increasingly ordered structure or enhanced CoCat fragment size, which cause a drop in the activity of the CoCat. XAS *In-situ* measurements show a slowdown of redox kinetics of the CoCat after being operated for 24 hours. This finding can be attributed to charge transport limitations in the thicker film, operated for 24 hours, and a different kinetic response of the Co-oxide fragment.

One-week operation of NiCat in Ni-free buffer at non-catalytic and catalytic potentials in glass container reveals that the redox charge drastically decreases within the first day of operation and then reaches a stable condition. However, the catalytic current has a different behavior, means that first it drops and reach a minimum amount and then continuously increased. The steady increase of catalytic current is related to Fe contamination of glassware because operation in a plastic container or Fe-containing buffer confirmed that. TXRF result also confirmed that the ratio Fe:Ni increases after the operation. The Tafel slope of NiCat after one-week operation is lower than as-deposited sample, meaning that lower overpotential is needed for operated sample to increase the reaction rate.

XAS measurements show that the minimum catalytic activity of NiCat operated at non-catalytic potentials (0.8 and 0.9 V vs. NHE, 11 hours) is related to a rather ordered amorphous nickel-oxide. However, after 48 hours of operation at these potentials, the catalyst is more disordered. On the other hand, operation at catalytic potential (1.4 V vs. NHE) induces a structure similar to γ-NiOOH, which is majorly stable over electrolysis time. Furthermore, long-time operation of a NiCat results in a shift of the edge position towards higher energies, which corresponds to higher oxidation state.

XAS *In-situ* measurements show that the derivative of the CVs fluorescence data matches very closely to the reductive wave of the CV, meaning that mostly related to redox and structural changes of the Ni metal centers and not to changes in other species (no formation of peroxides or superoxides for example).

Zusammenfassung

Für ein attraktives System zur effizienten, lichtgetriebenen Wasserspaltung müssen Wasseroxidationskatalysatoren verwendet werden, die im Idealfall nur auf der Erde vorkommenden chemischen Elementen basieren. Spitzenkandidaten sind Oxide von Übergangsmetallen der ersten Reihe, insbesondere der Elemente Mangan bis Kupfer. Im Jahr 2008 beschrieben Kanan und Nocera die elektrolytische Abscheidung eines amorphen Oxidfilms auf Cobaltbasis (CoCat) in Phosphatpuffer, der die Wasseroxidation im neutralen pH-Bereich fördert und sich durch selbstheilende Eigenschaften auszeichnet.

In dieser Arbeit wurde die Stabilität und Selbstheilung von Kobaltkatalysator (CoCat), Nickelkatalysator (NiCat) und Nickel-Eisen-Katalysator (NiFeCat) bei verschiedenen elektrochemischen Potentialen untersucht. Zyklische Voltammogramme wurden alle 30 Minuten gemessen, um die katalytische Aktivität und den Verlust an redoxaktiven Kobaltionen zu diagnostizieren. Außerdem wurde die Röntgenabsorptionsspektroskopie zur Beurteilung von Strukturveränderungen auf atomarer Ebene eingesetzt.

Das elektrische optimale Potentialfenster für eine weitgehend stabile (> 80%) CoCat-Probe beträgt 1,1 < V vs. NHE < 1,35, wobei nach 24-stündigem Betrieb in Co-freiem Phosphatpuffer (0,1 M) eine vertretbare Aktivität (> 65%) aufrechterhalten wird (KPi, pH 7). Auf der anderen Seite führt der Betrieb in Co-haltigem Puffer zu einer nahezu stabilen Leistung (in Bezug auf die Stromdichte pro geometrischer Oberfläche), aber die Filmdicke wächst signifikant. Daher ist die Selbstorganisation von CoCat keine erschöpfende Selbstheilung.

Die Strukturanalyse von CoCat, das in 20 µmol L^{-1} Co-haltigem KPi-Puffer für 24 Stunden bei einem katalytischen Potential (1,3 V vs. NHE) betrieben wurde, zeigt kleine, aber signifikante Änderungen in den EXAFS-Spektren, da der Betrieb bei langer Zeit eine zunehmende Ordnung oder eine potenziell gesteigerte CoCat-Fragmentgröße ergibt, die zu einer Abnahme der Aktivität von CoCat führt. XAS-In-situ-Messungen zeigen eine Verlangsamung der Redox-Kinetik von CoCat nach 24 Stunden Betrieb. Dieser Befund kann auf Ladungstransportbeschränkungen in der dickeren Schicht, die 24 Stunden lang betrieben wurde, und auf eine unterschiedliche kinetische Antwort des Co-Oxid-Fragments zurückgeführt werden.

Einwöchiger Betrieb von NiCat in Ni-freiem Puffer bei nichtkatalytischen und katalytischen Potentialen in Glasbehältern zeigt, dass die Redoxladung innerhalb des ersten Betriebstages drastisch abnimmt und dann einen stabilen Zustand erreicht. Der katalytische Strom zeigt jedoch ein anderes Verhalten, d.h. er fällt ab, erreicht ein Minimum und steigt dann kontinuierlich an. Der stetige Anstieg des katalytischen Stroms hängt mit der Fe-Kontamination von Glasgeräten zusammen, was der Betrieb in Kunststoffbehältern oder in Fe-haltigem Puffer bestätigt. Das TXRF-Ergebnis bestätigte auch, dass das Verhältnis Fe zu Ni nach dem Betrieb zunimmt. Die Tafel-Steigung von NiCat nach einer einwöchigen Operation ist geringer als bei der abgeschiedenen Probe, was bedeutet, dass eine niedrigere Überspannung für die operierte Probe erforderlich ist, um die Reaktionsgeschwindigkeit zu erhöhen.

XAS-Messungen zeigen, dass die minimale katalytische Aktivität von NiCat, das bei nichtkatalytischen Potentialen (0,8 und 0,9 V vs. NHE, 11 Stunden) betrieben wird, mit einem eher geordneten amorphen Nickeloxid zusammenhängt. Nach 48 Stunden Betrieb bei diesen Potentialen ist der Katalysator jedoch ungeordneter. Andererseits führt der Betrieb bei einem katalytischen Potential (1,4 V vs. NHE) zu einer γ-NiOOH-ähnlichen Struktur, die über die Elektrolysezeit weitgehend stabil ist. Darüber hinaus führt ein Langzeitbetrieb eines NiCats zu einer Verschiebung der Flankenposition in Richtung höherer Energien, was einem höheren Oxidationszustand entspricht.

XAS - In - situ - Messungen zeigen, dass die Ableitung der Fluoreszenzdaten der CVs sehr eng mit der reduktiven Welle des CV übereinstimmt, was bedeutet, dass dies hauptsächlich auf Redox - und Strukturänderungen der Ni - Metallzentren und nicht auf Änderungen in anderen Spezies zurückzuführen ist (keine Bildung von Peroxiden oder Superoxiden zum Beispiel).

Glossary

BESSY	Berliner Elektronenspeicherring-Gesellschaft für Synchrotronstrahlung
Bi	Borate buffer pH 9.2
CoCat	The cobalt oxide catalyst, deposited in KPi (0.1 M, pH7)
CoPi	The cobalt oxide catalyst, deposited or operated in KPi (0.1 M, pH7)
CV	Cyclic voltammetry or cyclic voltammogram
E_0	Energy shift in EXAFS simulations
EXAFS	Extended X-ray absorption fine-structure
FT	Fourier-transform
FEFF	The program used for calculation of phase functions
ICR	In-coming rate
ITO	Indium tin oxide
J	Current density
KPi	Potassium phosphate buffer pH 7
N	Coordination number
NHE	Normal hydrogen electrode
NiCat	The nickel oxide catalyst, deposited in Bi (0.1 M, pH 9.2)
OCP	Open circuit potential
OCR	Out-coming rate
OER	Oxygen evolution reaction
PSII	Photosystem II
q	Charge in general
RHE	Reversible hydrogen electrode
RFF	Fit quality of EXAFS simulations
σi	Debye-Waller parameter in EXAFS simulations
$S0^2$	Amplitude reduction factor in EXAFS simulations
SEM	Scanning electron microscopy
TOF	Turnover frequency
TXRF	Total reflection X-ray fluorescence
XANES	X-ray absorption near-edge structure
XAS	X-ray absorption spectroscopy
$\chi(E)$	EXAFS fine-structure function

Table of contents

Chapter 1

Introduction and Motivation

Since 1930 and after the discovery of oil, the supply of cheap energy has been possible. On the other hand, fossil fuels change the earth’s atmosphere and have some damaging effects on ecosystems. The effects are: warming of air and ocean, rising sea level, the ocean is becoming more acidic. Such cases damage our health. Since the late 1700s, the amount of carbon dioxide in the air was increased by 40 percent. Carbon dioxide and other greenhouse gases have warmed the surface, increase evaporation, which increases humidity, average rainfall, and heavy rainstorms in some places, but contributes to drought in others (Amendola and Meneghetti 2009). Reacting with water, Carbon dioxide forms carbonic acid, so the oceans are becoming more acidic. The Pacific Ocean has become about 25 percent more acidic in the past three centuries. Such acidity is suggested to increase another 40 to 50 percent by 2100 (Amendola and Meneghetti 2009).

Rising temperatures have even more effect on human health. High air temperatures can affect heat stroke, dehydration, affect people’s cardiovascular and nervous systems.

Unfortunately, global industrial emissions of carbon dioxide rose by 2.7% in 2018. Although, the deployment of renewable energies is increasing, such development is not fast enough. Besides, fossil fuels are too economically valuable to be burn.

Renewable energy resources, such as sunlight, are not always available. For a society to completely transition from fossil fuels to renewable energy, it is necessary to develop large-scale storage systems, which allow a constant usage of these resources.

Although, sustainable energy can be captured and directly converted into electrical energy, excess electricity should be stored for future supply. Notably, solar energy is intermittent and, to be used on a large scale, it needs an equally large capacity for energy storage.

Hydrogen fuel can be one of the best alternatives to fossil fuels because it could reduce the release of climate-changing gases and harmful compounds to human health. There are three methods of hydrogen production: fossil fuels, nuclear energy, and renewable energies. Hydrogen production is a promising material to store renewable energies. Water splitting can store energy in the form of fuel (H_2) and oxidant (O_2) and is among the most promising methods to produce hydrogen. Although the cathodic reaction to form hydrogen is of significant interest, water oxidation than water reduction is a bottleneck in water splitting. High overpotentials are often necessary to perform water oxidation at reasonable rates. Such overpotential represents an energy loss of 25% or more in water oxidation. Thus, the water-oxidizing catalysts that can be applied in electrolyzers, or photoelectrochemical devices is very promising. Despite recent success in the development of such catalysts, a stable, efficient and low-cost catalyst is rare. Especially, for reactions such as water-oxidation, which need a multi-electron transfer, both thermodynamic and kinetic limitations are essential. Research on water oxidation has focused on decrease overpotentials, cost and stability of catalysts. In addition, to synthesize a stable catalyst, the phenomenon such as self-healing is promising to have a stable catalyst. The protons and electrons from water-oxidation reaction could also be used to produce hydrocarbons and alcohols from CO_2 or ammonia from N_2.

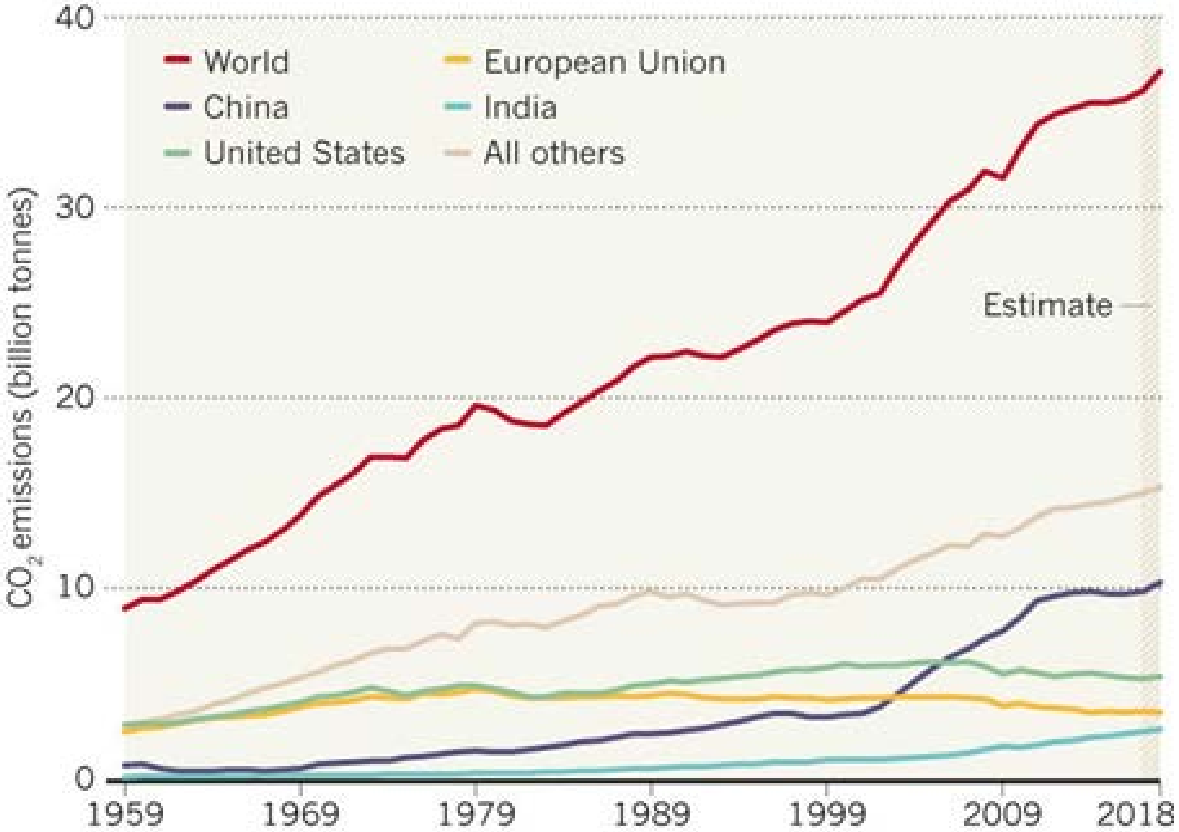

Figure 1.1. Annual industrial carbon dioxide (CO_2) emissions of the world and some industrial countries. Image reprinted from: https://www.nature.com/articles/d41586-018-07666-6

Water is a thermodynamically very stable compound. At 2200 °C, only 8% of the water molecules are split, and 50% at 3000 °C. Thus, an efficient and stable water-oxidizing catalyst is essential for water-splitting systems. In addition to generate a stable catalyst with self-healing properties are very promising. When self-healing is performed, the catalysts can work for a very long time. Such a phenomenon is highly critical for both industrial and biological applications.

To quantify the decomposition, Nosonovsky used the entropy conception(Nosonovsky and Bhushan 2009). According to this study, the decomposition results in a net increase in entropy, but reorganization and self-healing decrease entropy. Where the system works far from equilibrium, a decrease in entropy production occurs. Self-organization and self-healing are important phenomena and necessary to maintain the equilibrium using a moderating frictional force. If the system is performed under a metastable state, self-organization is vital to force the system toward its stable equilibrium state. In some cases, self-healing could be increased using heating, electricity or light (Nosonovsky and Bhushan 2009).

To our discussion, below phenomena should be defined*:*

- Self-healing (Self-repair, autonomic healing, and autonomic repair): *self-recovery of a compound following damage caused by the external environment or internal stresses* (Amendola and Meneghetti 2009, Fedrizzi, Fürbeth et al. 2011).
- Self-assembly: *occurs when a disordered system of pre-existing components forms an organized structure without external direction (Hill and Zhang 1995, Costentin and Nocera 2017).*
- Self-replication: *any behavior of a system that yields construction of an identical copy of itself (Amendola and Meneghetti 2009).*

Self-healing increases the lifetime of a compound and has been divided into several classes. The first class can perform an autonomous self-healing and need no external trigger to restore the damage, such as many biological systems (Wool 2008, Yuan, Yin et al. 2008, Murphy and Wudl 2010, Amendola and Meneghetti 2011).

The second group, which needs an external trigger to repair the system are non-autonomous self-healing systems (Ghosh 2009).

Some strategies have been used to generate self-healing compounds (Ghosh 2009). One strategy (Olugebefola, Aragón et al. 2010) used epoxy compounds as a healing polymer. During the damage, the capsules contain healing compounds such as a monomer fracture and a healing compound is released, which then heals into the crack and then reacts with a catalyst in the matrix, and forms the cross-linking to seal the crack (Rule, Brown et al. 2005, Youngblood and Sottos 2008). Another strategy is based on incorporating the healing agent into the system to start healing (Amendola and Meneghetti 2009, Potier, Guinault et al. 2014). Self-healing for nanomaterials is more important than bulk material because faster degradation and structural damage during usage (Amendola and Meneghetti 2011). On the other hand, the biological systems use different self-healing mechanisms than the self-healing in materials (Amendola and Meneghetti 2011).

Water oxidation is a four-electron reaction with high complexity. The reaction usually runs under harsh conditions. Thus, the related catalysts are typically prone to decomposition under the oxidation reaction.

1-1 Self-healing processes in the biological water-oxidizing complex

The water-oxidizing complex in Photosystem II could be described as a distorted cubic structure formulated as $Mn_4CaO_5(H_2O)_4$ cubane-like structure. There are 30 proteins in Photosystem II, but only D1 protein and rarely the reaction center D2 are extent prone to damage and are replaced by a newly synthesized one within a complicated mechanism (Aro, Virgin et al. 1993).

1-2 Self-healing processes for water-oxidizing catalysts

The self-healing in water-splitting systems is a recent interest. Nocera group in 2008 introduced the self-healing for cobalt-oxide based catalyst under water oxidation (Kanan and Nocera 2008, Lutterman, Surendranath et al. 2009). Then, other systems were investigated by other research groups (Najafpour, Kompany-Zareh et al. 2013, Najafpour, Sedigh et al. 2013, Huynh, Bediako et al. 2014).

In the following sections, we discuss the self-healing for cobalt, nickel - and manganese oxide.

1-2-1 Cobalt Oxides

In 1968, cobalt oxides in the presence of a solution of Ce(IV) perchlorate as an oxidant were reported as the water-oxidizing catalyst (Glikman and Shcheglova 1968). In the 1990s, cobalt oxide by the electrodeposition of Co(II) solution onto Ni mesh or Ti foil substrates was reported as a water-oxidizing catalyst in alkaline condition (Jiang, Chen et al. 1990, Jiang and Tseung 1991).

Self-healing properties for Co oxides were first reported in 2008 (Kanan and Nocera 2008, Lutterman, Surendranath et al. 2009). An amorphous CoO_x catalyst film (CoCat) was electrodeposited in the presence of cobalt and phosphate ions at neutral pH. Co(II), Co(III), and Co(IV) ions are important species during water oxidation (McAlpin, Surendranath et al. 2010). Cobalt and phosphate ions were tracked during water oxidation using radiolabelled ^{57}Co and ^{32}P isotopes (Lutterman, Surendranath et al. 2009). At open circuit potential, the catalyst was gradually dissolved, but under a potential bias of 1.3 V vs. NHE, no film dissolution was observed. This reaction is partially reversed in the presence of buffer electrolyte, which is described as a self-healing phenomenon (Figure1.2). In the absence of buffer, the film irreversibly degraded. Furthermore, without buffer, a decrease in pH results to even faster dissolution of cobalt ions.

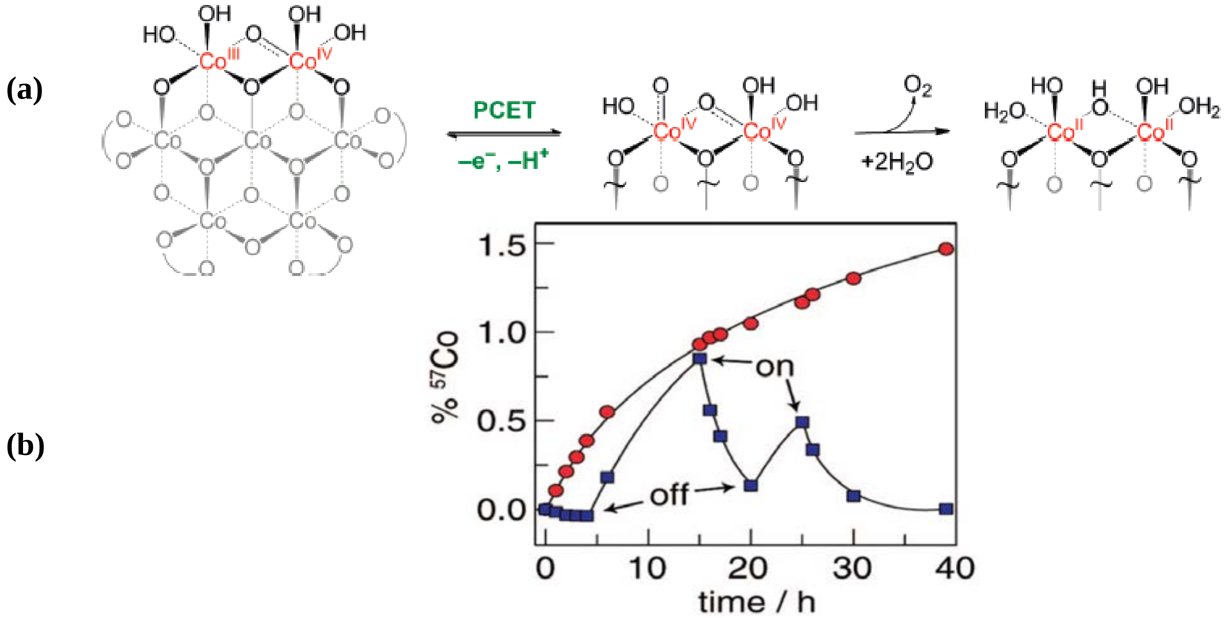

Figure 1.2. Proposed catalytic mechanism of the CoCat. Proton-coupled electron (PCET) equilibrium step: [Co(III)-OH] ↔ [Co(IV)-O] + H^+ + e^-. Rate-limiting step: O-O bond formation (a). Image (a) reprinted from (Surendranath, Kanan et al. 2010) with permission from American Chemical Society. Amounts of ^{57}Co leached from films of the Co-Pi catalyst on an electrode: with a potential bias of 1.3 V vs. NHE (blue squares) turned on and off at the designated times and held at open circuit potential (red circles). At open circuit potential, high amounts of Co ions were released from CoCat. After only 39 h, ~1.5% of the cobalt ions were observed in the solution. However, under a potential bias after 14 h, only 0.002% Co was detected in the solution. Image (b) reprinted from (Lutterman, Surendranath et al. 2009) with permission from the American Chemical Society.

Dau and co-workers used X-ray absorption spectroscopy (XAS) to determine the atomic structure and oxidation state of the cobalt oxide (Risch, Khare et al. 2009). This data showed that the active sites of CoCat are interconnected complete or partial Co(III) cubane clusters. Interestingly, the possible ligation with K^+-ions forms $Co_3K(\mu\text{-}O)_4$ cubanes, similar to the $Mn_3Ca(\mu\text{-}O)_4$ cubane in the water-oxidizing complex (WOC) in PSII.

Tiede group used Pair distribution function analysis to determine structure of the cobalt oxide-based water-oxidizing catalyst by high energy X-ray scattering. The experiments showed that the catalyst composes of a cobalt dioxide lattice sheet structure containing a Co_4O_4 cubane-type "defect." It consists of 13-14 cobalt ions with distorted coordination geometries. Phosphate ions are disordered components in the structure of catalyst (Du, Kokhan et al. 2012). Electrokinetic studies showed that in the absence of the buffer, the Tafel slope significantly increased.[29] However, A low concentration of phosphate (0.03 M) is enough to increase a Tafel slope of 59 mV/decade, but a higher concentration of buffer does not affect the rate of water-oxidation. One proton and one electron ($AH \leftrightarrow A^- + e^- + H^+$) reversible equilibrium, followed by a rate-limiting step was proposed as a mechanism for water oxidation. The equilibrium step was proposed to be a proton-coupled electron transfer (PCET) between Co(III)-OH and Co(IV)-O species, in the presence of phosphate as the proton acceptor. O-O bond formation is the chemical rate-limiting step, see Figure 1-a.

1-2-1-1 Self-healing of cobalt catalyst (CoCat)

Recently, Nocera's team presented the principles to design self-healing water-oxidizing catalysts using a chemical model (Kanan, Yano et al. 2010, Surendranath, Kanan et al. 2010, Farrow, Bediako et al. 2013, Costentin and Nocera 2017). They found that self-healing could be detected if the catalysts show self-assemble at applied potentials less than the potential for water oxidation. pH is a significant parameter to control both the self-healing and water oxidation.

An important parameter to determine the catalysis performance is the turnover number (TON, Figure 1.3). Catalysis was performed by a true catalyst state, which is produced from a precatalysis. During the reaction, the catalyst is decomposed to an inactive form, which may be regenerated to form the pre-catalyst by a chemical process (Costentin and Nocera 2017). For the cobalt-oxide system, the pre-catalyst formation usually involves the dissolution of cobalt ions into the buffer. In the water-oxidation reaction in the basic solution, hydroxide neutralizes the released protons. However, at pH 7 the concentration of OH^- is low and the strongest base in water is therefore the cobalt oxide itself. The reaction of the released protons with the cobalt oxides leads to corrosion and leaching of cobalt ions. This corrosion in water balances with self-assembly in the presence of phosphate or borate anions. The self-healing catalyst is found by infinite turnover number because the catalyst can heal itself (Costentin and Nocera 2017).

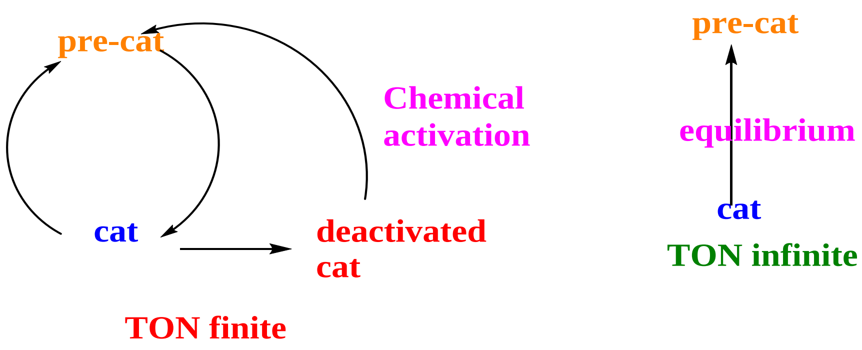

Figure 1.3. A catalyst that is repaired versus self-healing. For a catalyst, which shows self-healing, infinite stability and thus an infinite TON could be observed. Image reprinted from (Costentin and Nocera 2017) with permission from the National Academy of Sciences of the United States of America.

1-2-1-2 A qualitative model for self-healing

The active sites for CoCat are Co(IV) species (McAlpin, Surendranath et al. 2010, Ullman, Brodsky et al. 2016, Brodsky, Hadt et al. 2017). Isotopic oxygen labeling and other investigations have displayed that the active sites are edge sites of the clusters. A dicobalt site could be a structural unit for water oxidation (Figure 1.4) (Winkler and Gray 2011).

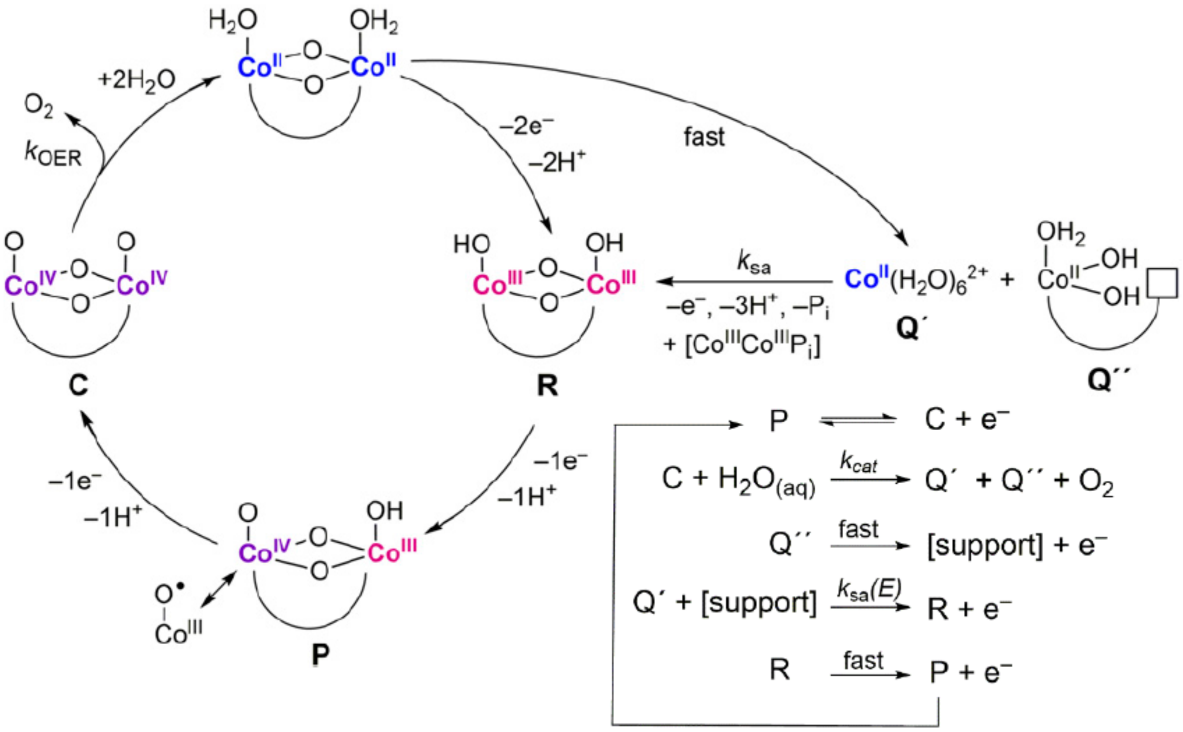

Figure 1.4. Water-oxidation pathway for CoCat suggested by electrochemical kinetics, electron paramagnetic resonance, and XAS studies. Curved lines are connecting Co active site, phosphate or OH_x terminal or bridging ligands. The path on the far right is the self-assembly pathway to reconstitute the catalyst. The [Co(III)Co(III)Pi] species represents Co(III)edge active sites. Image reprinted from (Costentin and Nocera 2017) with permission from the National Academy of Sciences of the United States of America.

1-2-1-3 A quantitative model for Self-healing of CoCat

The catalyst forms from a Co(III) Co(IV) pre-catalyst (P) as shown by electrochemical kinetics, EPR, and XAS studies (Ullman, Brodsky et al. 2016). The “Co(IV)” or Co(III)–O• oxyl radical is necessary for water oxidation (Winkler and Gray 2011). The rate law for water oxidation by the CoCat was extracted from the Tafel slope (Costentin and Nocera 2017):

$$j = 4F\Gamma_{CoP_i}k_0^{OER}\frac{1}{[H^+]}exp\left[\frac{FE}{RT}\right] \qquad (1.1)$$

j: is the current density,

F: Faraday’s constant,

Γ_{CoP_i}: the surface concentration of CoCat deposited onto the electrode from potassium phosphate buffer (CoPi)

k_0^{OER}: is proportional to the exchange current density.

The rate law can indicate a $1e^-/1H^+$ PCET minor equilibrium to generate the active “Co(IV) Co(IV)” catalyst (C), which is critical to O-O bond formation.

Self-healing in CoPi occurs at a catalytic potential where water oxidation happens. At this potential catalyst is self-assemble. For CoPi catalyst, self-assembles from phosphate buffer and Co(II) ions at potentials 0.2 V lower than the potential needed for water oxidation (Costentin and Nocera 2017). Under this condition, Co(II) ions are oxidized to inert Co(III) ions, resulting in deposition of the film.

The Tafel plot indicates a one-electron reversible equilibrium is preceding a chemical rate-limiting step to catalyst formation for the catalyst assembly mechanism. The first-order dependence on Co(II) concentration may show a reversible one-electron equilibrium involved Co(II) ion in the solution (Costentin and Nocera 2017). An electrochemical rate law for catalyst formation and growth was obtained as:

$$j = Fk_0^{sa} \frac{[Co^{2+}]}{[H^+]^3[P_i]} exp\left[\frac{FE}{RT}\right] \qquad (1.2)$$

where k_0^{sa} is related to the exchange current density for the electrodeposition self-assembly reaction. A model based on this rate law is shown in Figure 1.5.

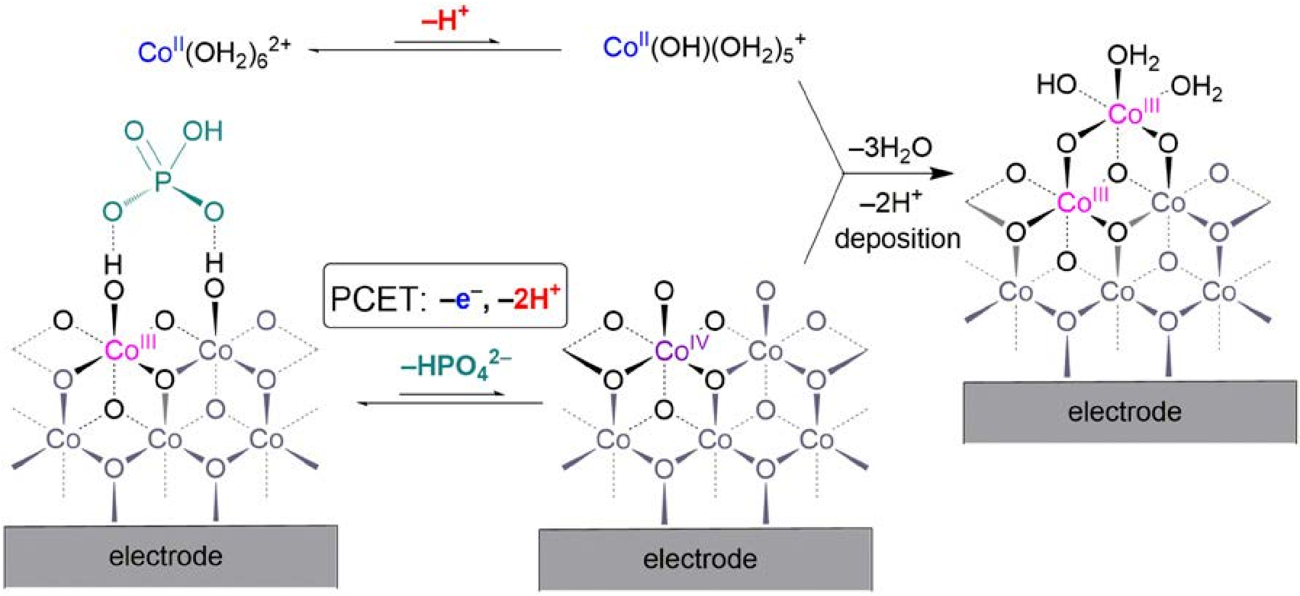

Figure 1.5. The proposed mechanism of CoCat catalyst self-assembly. Self-healing in the cobalt-based catalyst is performed at the potential at which water oxidation occurs vs. the potential at which the catalyst self-assembles. The catalyst self-assembles in the presence of phosphate solution containing Co^{2+} ions upon the application of applied potentials 0.2 V negative of the potential needed for water splitting.
Image reprinted from (Costentin and Nocera 2017) with permission from the National Academy of Sciences of the United States of America.

Water oxidation and self-assembly for CoPi may be found from the $\partial E/\partial pH$ dependence for these two reactions as shown by Eqs. 1 and 2 (Costentin and Nocera 2017). The critical factor for self-healing is that the electrodeposition reaction shows an inverse third-order dependence on proton activity, whereas water oxidation indicates the first-order dependence on proton activity. Thus, the self-assembly occurs much more rapidly with decreasing pH compared with that for water oxidation. The nucleation and growth for the catalyst are below the potentials for water oxidation, and as long as the catalyst is operated in the green zone, the CoPi is indefinitely stable in water using self-healing (Fig. 1.6).

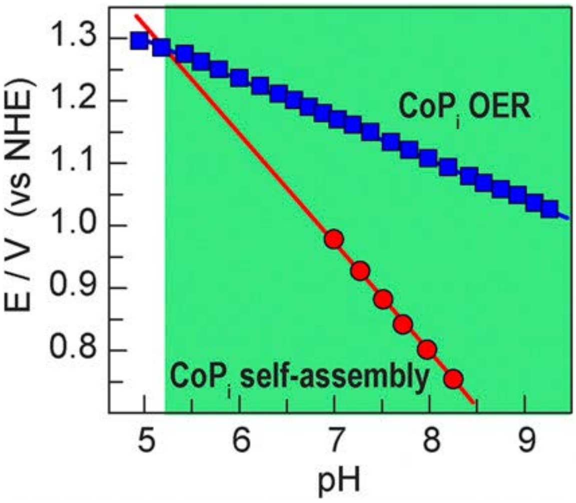

Figure 1.6. Pourbaix diagram for the catalyst (blue squares) and self-assembly (red circles) at j = 30 μA·cm^{-2}. Image reprinted from (Costentin and Nocera 2017) with permission from the National Academy of Sciences of the United States of America.

The released Co(II) ions (Q′) can reincorporate into the catalyst by the self-assembly process shown in Figure 1.4 and characterized by an overall apparent rate constant, k_{sa}^{0}. The rate for self-assembly without buffer is:

$$k_{sa}(E) = k_{sa}^{0}\frac{(C_0)^4}{[H^+]^3[P_i]}exp\left[\frac{FE}{RT}\right] \qquad (1.3)$$

C_0: is a normalization concentration for cobalt ion in solution.

k_{sa}^{0}: the intrinsic rate constant.

Similarly, the rate constant for water oxidation catalysis is:

$$k_{OER}(E) = k_{OER}^{0}\frac{C_0}{[H^+]}exp\left[\frac{FE}{RT}\right] \qquad (1.4)$$

C_0: a normalization concentration.

k_{OER}^{0}: the intrinsic catalytic rate constant.

The ratio of $k_{sa}(E)$ to $k_{OER}(E)$ is related to the electrochemical cell parameters (such as dimensions, etc.). If the CoCat catalyst is operated at a constant potential E in a solution containing a highly concentrated buffer and Co(II) ions:

$$\tau = \frac{1 + \frac{k_{sa}(E)}{D/\delta}}{k_{OER}(E) + \frac{k_{sa}(E)}{V/S}} \qquad (1.5)$$

V: the volume of the solution.

S: the electrochemical electrode surface area.

D: is the $Co(H_2O)_6^{2+}$ diffusion coefficient.

δ: the size of the diffusion layer

A steady-state condition is observed when t >> τ . For the steady-state condition, the fraction of the remaining active film can be written as:

$$\frac{\Gamma_{CoP_i}^{active}}{\Gamma_{CoP_i}^{0}} = \frac{\frac{k_{sa}^0}{\frac{V}{S}k_{OER}^0}}{\frac{[H^+]^2[P_i]}{(C^0)^3} + \frac{k_{sa}^0}{\frac{V}{S}k_{OER}^0}} \qquad (1.6)$$

This fraction depends on a geometrical parameter V/S as well as on intrinsic properties of the catalyst, k_{sa}^0/k_{OER}^0. Especially, the fraction in Eq. 1.6 depends on the self-assembly elements of pH and buffer concentration

1-2-2 Self-healing for Ni oxide

Nickel oxide in energy-storage systems has been applied for many years (Halpert 1984). Nickel electrodes are used in batteries (Merrill and Dougherty 2008). Nickel oxide/hydroxides (Appleby, Crepy et al. 1978, Hall 1983) and mixed nickel oxides, and Ni complexes have been extensively reported as water oxidizing catalysts.

Corrigan and co-workers reported that Fe-impurities in Ni oxides improves water oxidation (Corrigan 1987). It is interesting that even 0.01% of iron could significantly decrease overpotential for water oxidation. The effect of Co, Cr, Mn, and Cu incorporation on Ni oxide toward water oxidation were also considered by Pletcher and co-workers (Li, Walsh et al. 2011). The addition of Mn and Cu decrease water oxidation by $Ni(OH)_2$. However, Cr improved water oxidation.

Ni oxides are very promising catalysts for water oxidation (Dincă, Surendranath et al. 2010). Self-repair of nickel oxide has not been significantly considered so far because of the stability of this metal oxide under water oxidation (Dincă, Surendranath et al. 2010). Based on the Pourbaix diagram for nickel, below pH 9, nickel ion (Ni^{2+}) is the stable ion in over a wide range of potentials. Below pH 9, nickel oxide dissolves and it depends on the structure and component of the electrolyte (Dincă, Surendranath et al. 2010). Even at a high potential, no re-deposition is observed. Under alkaline electrolysis, and based on the mechanistic studies by Nocera and co-workers, all Ni oxides are insoluble in water (Huynh, Bediako et al. 2014). Long-Term stability was observed under this condition for nickel oxide (Singh, Chang et al. 2013, Gao, Sheng et al. 2014). Incorporation of Fe into nickel oxide has a significant role at self-healing reaction.

1-2-3 Manganese oxides

Glikman, Shcheglova (Glikman and Shcheglova 1968) and Morita (Morita, Iwakura et al. 1977, Morita, Iwakura et al. 1979) were the first groups to consider water oxidation by Mn oxides. Mn is low-cost and environmentally friendly. Besides, Nature uses an Mn catalyst to oxidize water. Thus, Mn compounds are interesting for water oxidation.

Hocking *et al.* used $[Mn_4O_4L_6]^+$ complex to oxidize water (Hocking, Brimblecombe et al. 2011). The complex was dissociated in Nafion yielding uncomplexed Mn(II) ions which were transformed into a disordered Mn(III/IV) oxide phase under water oxidation. They proposed that illumination of Mn(III/IV) oxide results in oxygen evolution and photoreduction to Mn(II) species which are transformed into Mn oxide under electrochemical condition (Figure 1.7). They considered the regenerate of the catalyst as self-heal, which needs the potential to perform (Hocking, Brimblecombe et al. 2011).

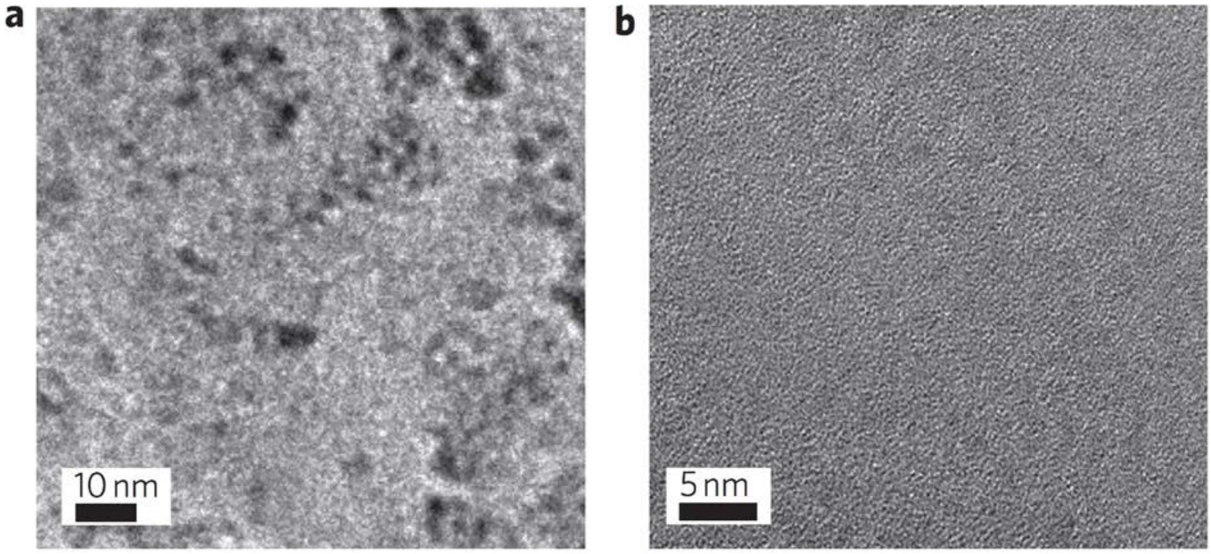

Figure 1.7. High-resolution transmission electron microscopy image of Nafion film indicating the presence of nanoparticles of MnO_x formed by the electro-oxidation of $[Mn_4O_4L_6]^+$ at 1.0 V (versus Ag/AgCl) (a). High-resolution transmission electron microscopy image of Nafion film after the introduction of $[Mn_4O_4L_6]^+$ into the film. No nanoparticles are evident, but the presence of Mn^{2+} in Nafion was confirmed by XAS (b). Image reprinted from (Hocking, Brimblecombe et al. 2011) with permission from McMillan publication.

Another self-healing reaction was also reported for Mn oxide in the presence of $(NH_4)_2Ce(NO_3)_6$ (Ce(IV)) under the water-oxidation reaction.[22] Under this condition, MnO_4^- is formed, which is the product of the decomposition of the catalyst. However, MnO_4^- reacts with Mn(II) or Mn(III) to regenerate Mn oxide. It is interesting that the Mn oxide could be stable even after 15 days in the presence of Ce(IV).

Nocera's group in 2014 reported a self-healing mechanism for MnO_x under the water-oxidation condition (Huynh, Bediako et al. 2014). Under acidic conditions, a high slope of the Tafel (653 mV/decade), zeroth-order dependence on phosphate buffer and zero order dependence on H_3O^+.

Such high slope more (than 120 mV/decade) are known as quasi-infinite and are corresponded with an initial turnover-limiting chemical step. The stability of the first-row metal oxide is an issue under acidic condition. The local metal centers have t_{2g}^* and, e_g^*, which are antibonding, and an increase in the number of electrons in these orbitals weaken the metal-oxygen and thus the metal-oxide structure and finally lead to more facile oxide degradation (Huynh, Bediako et al. 2014). Early first-row transition metal oxides with lower electrons in t_{2g}^* and e_g^* orbitals, such as Mn oxide, are more stable acidic condition than the late first-row metal oxides.

However, the four-electron chemistry of water oxidation causes Mn oxide to cycle to Mn(II), which is labile and easily leaks from the structure (Huynh, Bediako et al. 2014). Using the potential Mn oxide is deposited, and as long as Mn oxide deposition occurs at a potential below those required for water oxidation, the films will remain stable through self-repair owing to the re-oxidation of Mn ions in the solution.

1-2-4 Another strategy

Ventosa's group (Barwe, Masa et al. 2017) reported a new strategy to obtain a stable catalyst with self-healing activity based on self-assembly process of catalyst particles during electrolysis. The particles are added to the electrolyte and are pumped toward the electrolyzer. Based on their charges, particles stick onto the anode or the cathode. The self-assembled catalyst showed self-healing when sufficient catalyst particles are present in the electrolyte. The approach could help for an "operando" modification of electrodes while the electrolyzer is performing, using electrostatic interaction between the electrode and the particles. The document for self-healing was obtained in an alkaline electrolyzer using NiFe-LDH and Ni_xB catalyst powders for anode and cathode, respectively. The nanoparticle films formed on electrodes and were stable for at least 22 days of continuous electrolysis in the range of 50-100 mA/cm^2.

As we discussed, self-healing for water-oxidizing catalysts is a new finding and some issues regarding the phenomenon should be clarified. An important issue is a long-term operating for self-healing. Long-term operation conditions for an electrodeposited cobalt oxide catalyst for electrochemical water oxidation at neutral pH was not considered so far.

1-3 Scope and organization of the thesis

The main scope of this thesis is the identification of stability and self-healing of first-row transition metal oxides catalyst like cobalt oxide (CoCat), nickel oxide (NiCat) and nickel-iron (NiFe) films for water splitting by addressing some important questions such as:

"Which interval potential is the optimal condition for stability of catalyst?", "Is the re-assembling process of a catalyst also a self-healing process?", "Does the structure of the catalyst change after operation?", moreover, "How fast oxidation state changes kinetic is?" are addressed in this work.

The chapters are organized as follows:

Chapter 2	examines the stability of cobalt catalyst (CoCat) in Co-free buffer as well as the optimal potentials for long term operating.
Chapter 3	investigates the self-healing process of cobalt catalyst operated in cobalt-containing buffer as well as understanding the catalytic mechanism of samples operated in Co-free and Co-containing buffer by Tafel slope analysis.
Chapter 4	interrogates the structures of fresh CoCat and of CoCat films operated for 24 hours in Co-free and Co-containing buffer using X-ray absorption spectroscopy (XANES, EXAFS). Increasing fragment size and a higher degree of order in the Co-oxide framework is observed in CoCats operated for 24 hours. *In-situ* X-ray fluorescence spectroscopy reveals slower redox kinetics in samples operated for 24 hours in Co^{2+}-containing buffer.
Chapter 5	addresses the stability and self-healing of a nickel-based catalyst (NiCat) operated in Ni-free and Ni-containing buffer. The exact amount of nickel was determined by TXRF. The catalytic mechanism was investigated by Tafel slope analysis. The effect of iron contamination on NiCat activity is also studied.
Chapter 6	investigates oxidation state and structural changes of NiCat after the long-time operation at catalytic and non-catalytic electrode potentials. The effect of operation time on the oxidation state of NiCat is addressed. To provide evidence for changes in the redox kinetics of NiCat, time-resolved XAS experiments were conducted.
Chapter 7	examines the self-repair of nickel-iron catalyst (NiFeCat) at different potentials in neutral and alkaline pH for two days.

Chapter 2

Stability of cobalt oxide catalyst (CoCat) in Co-free buffer

Long-term operating conditions for an electrodeposited cobalt oxide catalyst (CoCat) for electrochemical water oxidation at neutral pH in Co-free buffer (0.1 M, KP_i, pH 7) are discussed and self-repair concepts are considered. Herein, CoCat was operated at several selected catalytic and non-catalytic potentials for 24 hours. Cyclic voltammograms (CV, 0.65 – 1.40 V vs. NHE) with a scan rate of 20 mVs^{-1} were run every 30 minutes to diagnose losses in redox-active cobalt ions and catalytic activity.

Electrochemical results show that the activity drops higher than 50 % when CoCat is operated in Co-free buffer at low potentials (< 1.0 V vs. NHE) and elevated potentials (> 1.3 V vs. NHE). Therefore a narrow potential range (1.1 < V vs. NHE < 1.35) is suggested as an optimal window for having a comparably stable CoCat, where reasonable activity maintains after 24 hours.

Portions of chapters 2, 3 and 4 have been prepared for publication:

Mohammad Reza Mohammadi, Stefan Loos, Petko Chernev, Chiara Pasquini, Ivelina Zaharieva, Diego Gonzalez-Flores, Paul Kubella, Katharina Klingan, Rodney D. L. Smith, Holger Dau

M. R. Mohammadi performed all experiments and the results are shown in chapters 2, 3 and 4.

S.Loos, P.Chernev, C.Pasquini, I.Zaharieva, D.Gonzalez-Flores, P.Kubella, K.Klingan, R.D. L. Smith assisted in synchrotron measurements and by valuable discussions.

H. Dau supervised.

2.1. Experimental Section

2.1.1 Materials

Reagents: $Co^{II}(OH_2)_6(NO_3)_2$ (Sigma Aldrich, ≥ 99.9%), H_2KPO_4 (Roth, ≥ 99%), K_2HPO_4 (Roth, ≥ 99%),

All reagents where used without further purification. Solutions were prepared with 18.2 MΩ·cm Milli-Q water.

2.1.2 Electrodeposition of Co oxide Catalyst (CoCat)

All potentials are given relative to the potential of a normal hydrogen electrode (NHE).

All solutions were prepared from purified, deionized water (18.2 MΩ·cm Milli-Q water).

KP_i was prepared as a mixture of approximately 40% KH_2PO_4 and 60% K_2HPO_4 at a total KP_i concentration of 0.1 M. The pH of the buffer has been verified by adjusting the pH to 7.00 +/- 0.05; fine adjustment of the pH was achieved by addition of small aliquots of KH_2PO_4 (0.1 M) to K_2HPO_4 (0.1 M).

For electrodeposition, concentrated $Co^{II}(NO_3)_2 \cdot 6\ H_2O$ (50 mmol L^{-1}) solution was added to the KP_i buffer such that the final concentration of the Co-electrolyte solution was 0.5 mmolL^{-1}. The working electrodes (indium tin oxide on glass, Visiontek Systems Ltd) have been cleaned with Ethanol and MilliQ water. A platinum mesh (25×25 mm^2) served as a counter electrode and an Ag/AgCl-electrode (≈200 mV vs. NHE, Metrohm) as a reference electrode. The cell geometry was roughly the same for all the following electrochemical characterizations (distance between working and reference electrode ~0.5 cm).

10 $mCcm^{-2}$ have been deposited at a potential of 1.05 V vs. NHE. After electrodeposition, all glassware has been cleaned with diluted nitric acid and Millipore MilliQ water.

Cobalt oxide deposition and electrochemical analyses were performed in a single-compartment, three-electrode setup controlled by a Gamry potentiostat (Gamry Interface 1000^{TM}, Warminster, USA) with 8 potentiostats, having in total 10 channels (10 simultaneous experiments; Figure 2.1), each one in a three-electrode setup.

Active IR-drop compensation is not possible with this type of potentiostat, so for both, deposition and operation, no IR-compensation was performed. The uncompensated resistance (R_u) was about 40 Ω.

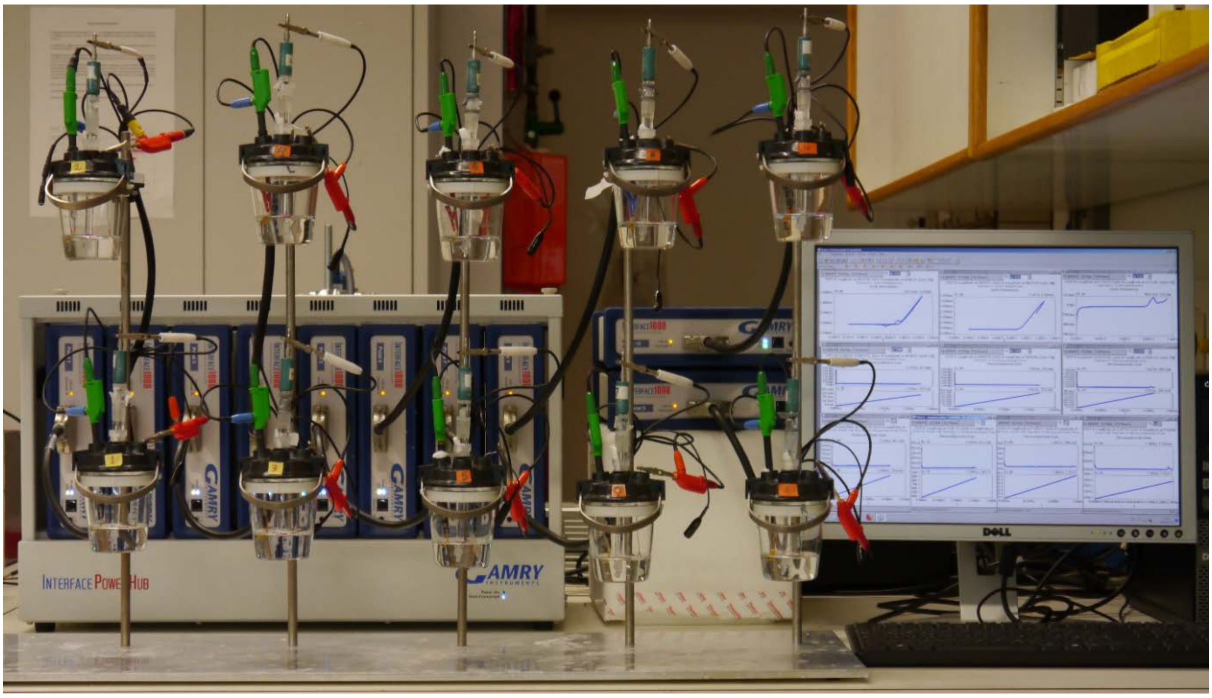

Figure 2.1. Ten parallel Gamry potentiostats (Gamry Interface 1000^{TM}, Warminster, USA) for electrochemical experiments (deposition and operation) control ten single-compartment electrochemical cells with each three electrodes.

2.1.3 Electrochemical Characterization

After electrodeposition, counter and reference electrodes were cleaned with 30% nitric acid and MilliQ water (18.2 MΩ). Then the catalyst, the Co oxide film (CoCat) was operated in Co-free buffer (0.1 M KPi, pH 7) at several selected catalytic and non-catalytic potentials for 24 hours. Cyclic voltammograms (CV, 0.65 – 1.40 V vs. NHE) with a scan rate of 20 mVs^{-1} were run every 30 minutes to diagnose losses in redox-active cobalt ions and catalytic activity (Figure 2.3). The second CV scan is analyzed.

2.1.4 Evaluation of deposited material by TXRF

Chemical analysis was conducted using a total reflection X-ray fluorescence (TXRF) instrument (PicoFox, Bruker). Quartz glass substrates have been cleaned following a protocol (see appendix). The cobalt oxide films were dissolved in 500 µL of 30% HCl, and 500 µL of diluted Ga standard ($Ga(NO_3)_3$, 1000 mgL^{-1}, Fluka TraceCert) was added. For all prepared solutions the final Ga standard concentration was 5 mgL^{-1} and 10 µL of the mixture was immobilized on a silicon coated quartz glass sample plate for quantification. A drop of the analyte solution was slowly evaporated on a silicone-coated quartz glass disk. The TXRF acquisition time was 30 minutes per sample.

2.1.5 UV-Vis spectroscopy

Optical absorption spectra were recorded on a Cary 50 UV-Vis spectrophotometer (Varian GmbH, Waldbronn, Germany).

10 $mCcm^{-2}$ cobalt catalyst were deposited on an ITO/glass substrate (KP_i, 0.1 mol L^{-1}, pH 7; cobalt concentration: 0.5 mmol L^{-1}). Afterward CoCats were operated in Co-free KP_i buffer for 24 hours. All samples were dried under ambient conditions for about six hours then the UV-Vis absorption experiments were conducted to compare the amount of cobalt ions of the samples.

2.2 Results and Discussions

2.2.1 Stability of CoCat at open circuit potential (OCP) condition

It is interesting to study the stability of cobalt catalyst in the buffer (0.1 M KPi, pH 7) while any external potential applied, meaning that there is no current but the potential difference between two electrodes could be recorded (OCP). To investigate this, after electrodeposition and proper cleaning, open circuit potential for 24 hours was applied. Cyclic voltammograms (0.65 – 1.40 V vs. NHE) with scan rates of 20 mVs^{-1} were run every 30 minutes to diagnose losses in redox-active cobalt ions and catalytic activity (Figure 2.2). This Figure shows a typical CV of as-deposited cobalt film. The thermodynamic equilibrium potential (E_0) was shown in CV. Figure 2.2 demonstrate that below 0.9 V the current is zero and at 0.95 V Co^{2+} converted to Co^{3+} while about 1.12 V is needed for cobalt oxidation state from Co^{3+} to Co^{4+}. The negative area of CV (colored part) illustrates the redox-active cobalt ions.

As the oxidation wave of Co^{2+}/Co^{3+} in the anodic sweep is merged with oxygen evolution, the cathodic branch is evaluated instead. To ensure appropriate assessment, data are presented normalized to 1 to have an estimate of the relative changes of the catalytic activity and redox-activity. This is necessary to even out slight variations (<10%) in current density and redox charges at the very beginning (t=0). Figure 2.3 shows that after 24 hours more than 80 % of the initial amount of cobalt is dissolved. It means that the CoCat is not stable when no current is flowing.

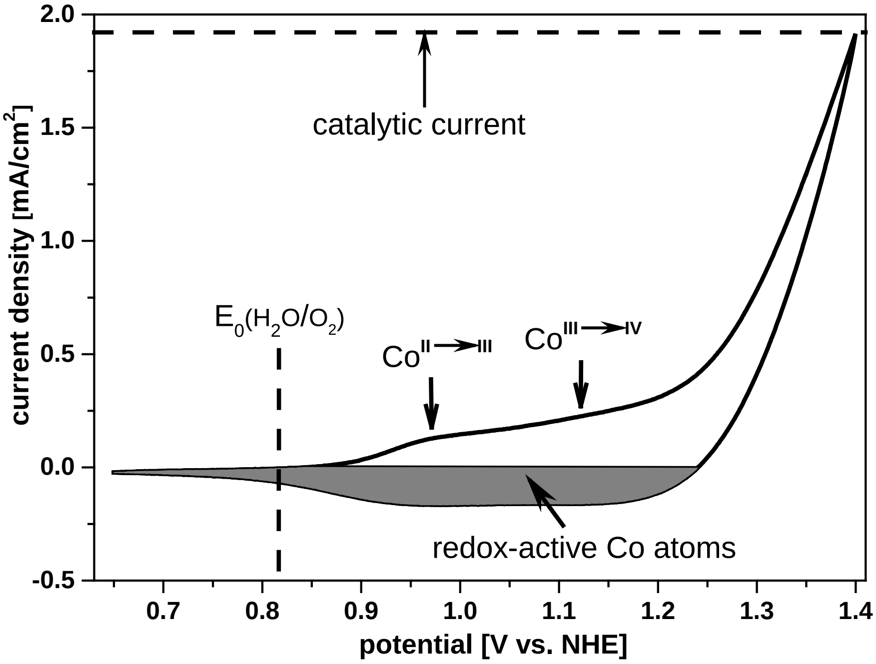

Figure 2.2. A typical cyclic voltammogram (CV) for CoCat as prepared in 0.1 M KP_i buffer at pH 7. The current density has been taken at the vertex of the CV. As the Co-oxidation peak at ~1.1 V cannot completely be separated from water oxidation, the number of redox active cobalt atoms is derived from the integrated area between the curve and the voltage axis in the reverse scan.

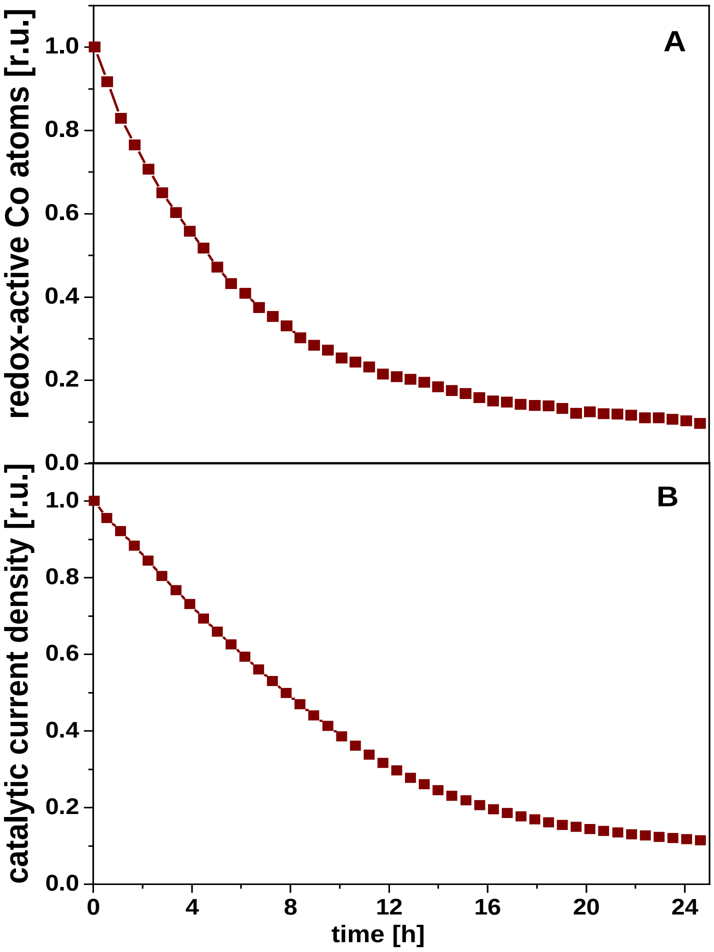

Figure 2.3. Number of normalized redox-active cobalt ions (A) and catalytic current density (B) from CoCat sample when no current is flowing (OCP). The redox-charge and the catalytic current density of the initial CV were 3.7 mC/cm^2 and 2.1 mA/cm^2, respectively. Lines added in between the data points serve to guide the eye.

2.2.2 Stability of CoCat at catalytic and non-catalytic electrode potentials

Figure 2.2 shows that the first cobalt oxidation state changes (Co$^{II\rightarrow III}$) occur around 0.95 V vs. NHE. Therefore non-catalytic and catalytic potentials were selected in between 0.65 to 1.5 V vs. NHE. To monitor the amount of cobalt and the catalytic activity of each sample, cyclic voltammogram was recorded every 30 minutes and the redox-activity and the catalytic activity normalized to the initial CV. The results were presented in Figures 2.4 and 2.5.

As indicated by Figures 2.4 and 2.5, the amount of redox active cobalt atoms (A), as well as the catalytic current density (B), strongly depend on the applied potential. Starting with 0.85 V vs. NHE more and more Co ions can undergo reversible redox changes. For potentials above 1.25 V vs. NHE the opposite occurs, the redox activity is decreasing with further increasing potentials of operation. Almost identical behavior holds for the catalytic current density due to oxygen evolution. Potentials between 1.1 and 1.3 V vs. NHE lead to 55% to 65% of the initial activity level after 24 hours.

From these observations we derive: (1) the capability to undergo oxidation state changes is strongly coupled with the catalytic current density and the films tend to dissolve for lower and higher potentials. (2) Intermediate overpotentials ((300 – 500) mV) are optimal for stable CoCat performance (more than 55% after 24 h), shown in Figures 2.4 and 2.5.

To obtain a reasonable current density, it is necessary to have the operating potential close to 1.3 V vs. NHE for further investigations. The results are presented in two Figures and panels (A and B to make the trend better visible.

To assess how fast the CoCat dissolves under open circuit conditions, the 24-hour protocol was applied and the redox charge, as well as the catalytic current, were obtained from the CVs taken every 30 minutes. The results are shown in Figure 2.4. These results indicate that those samples operated at potentials below 0.95 V vs. NHE are dissolving even faster than without any potential applied.

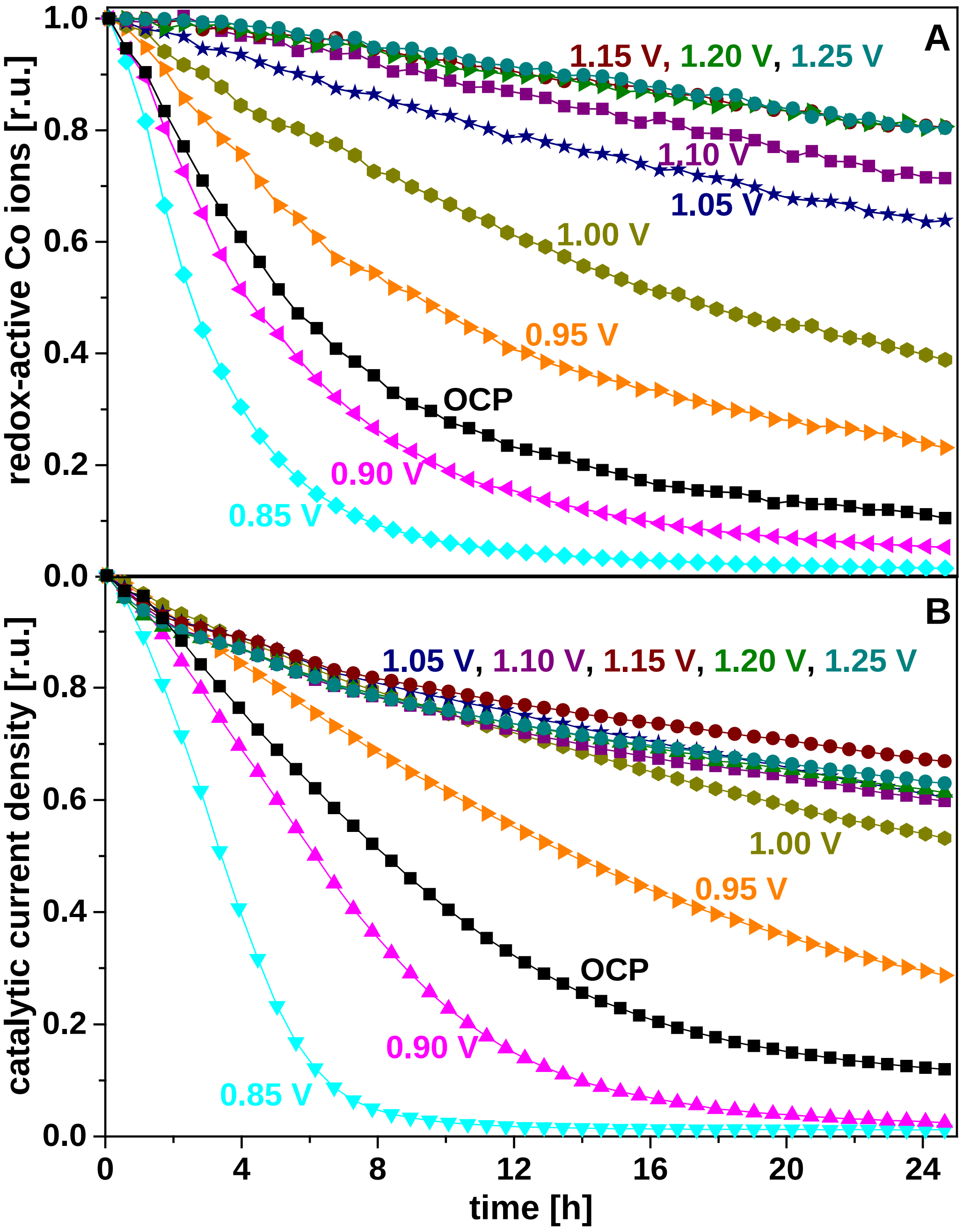

Figure 2.4 Amount of redox-active cobalt ions normalized to the initial CV (A) and catalytic current density normalized to the initialCV (B) from different CoCat samples, each operated at a certain potential vs. NHE in Co-free KP_i buffer at pH 7 for 24 hours. For low overpotentials (< 200 mV) the amount of redox active Co-ions is drastically decreasing. The results of samples operated at potentials below 0.85 V vs. NHE were similar to the 0.85 V sample and are not shown here. For intermediate overpotentials (200 – 500 mV, 1.05 – 1.35 V vs. NHE) the catalyst maintains more than 50 % of the initial activity. The catalytic current density is only reasonably stable (> 55 %) for intermediate overpotentials. The mean value of the redox-charge and the catalytic current density of the initial CV of all samples were about 3.5 mC/cm^2 and 2 mA/cm^2, respectively.

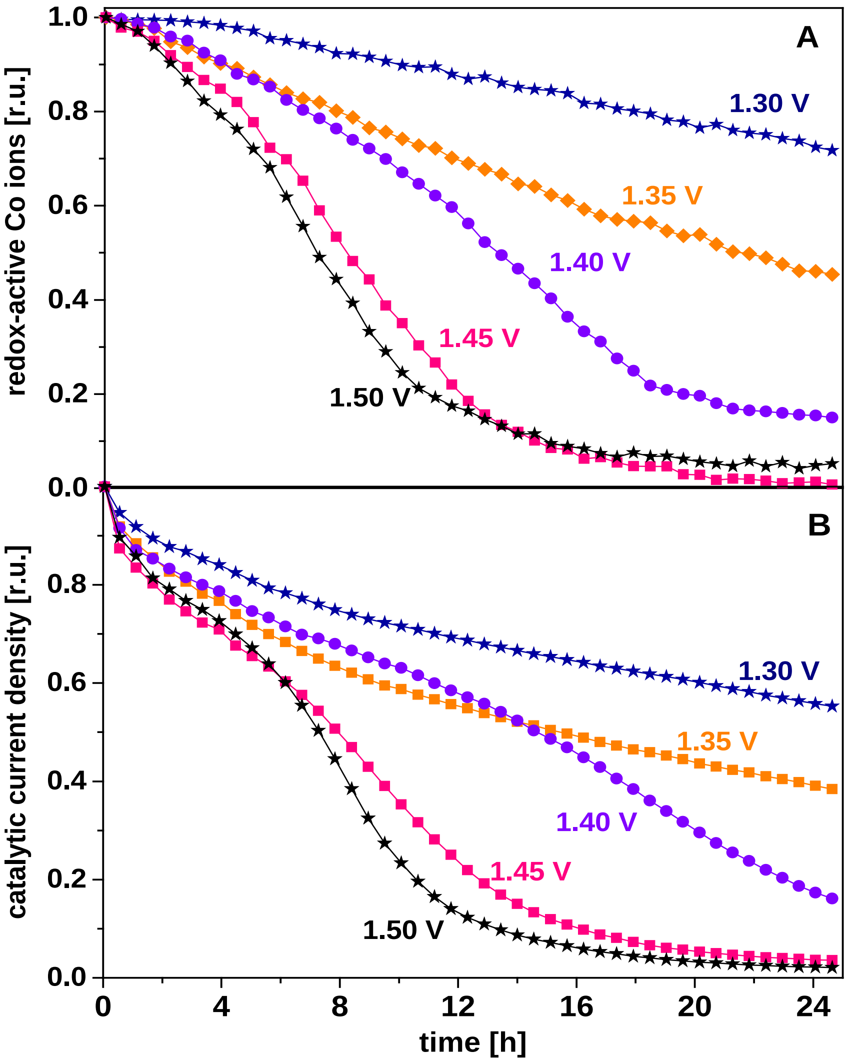

Figure 2.5. Amount of redox active cobalt ions (A) normalized by initial CV and catalytic current density (B) of different CoCat samples, each operated at a certain potential vs. NHE in Co-free KP$_i$ buffer at pH 7 for 24 hours. For high overpotentials (> 500 mV) the amount of redox active Co-ions is drastically decreasing. The mean value of the redox-charge and the catalytic current density of the initial CV of all samples were about 3.5 mC/cm^2 and 2 mA/cm^2, respectively.

The previous Figures could suggest that all redox active Co-atoms of the film are catalytically active as catalytic current and redox activity follow the same trend. This is in line with previous findings that provided evidence for bulk activity (Klingan, Ringleb et al. 2014). The loss in activity we observe, could be related to the loss of Co ions (e.g. dissolving), accordingly.

TXRF analysis was carried out to determine the exact amount of cobalt of each operated sample. This was performed for non-catalytic and catalytic electrode potentials (0.65 – 1.5 V vs. NHE). As the films operated at very low overpotentials (0.65 – 1.00 V vs. NHE), most parts of catalyst are dissolved and only very few cobalt atoms remain after 24 hours, so TXRF analysis was carried out after 3 hours of operation for these samples. The TXRF results were shown in Figure 2.6. The left Y-axis shows the absolute amount of cobalt atoms, while right Y-axis presents the redox active cobalt atoms were extracted from CV after 24 hours operation. This Figure (A: after 3 hours and B: 24 hours of operation) reveals that the absolute amount of cobalt present is following the trend of the redox activity.

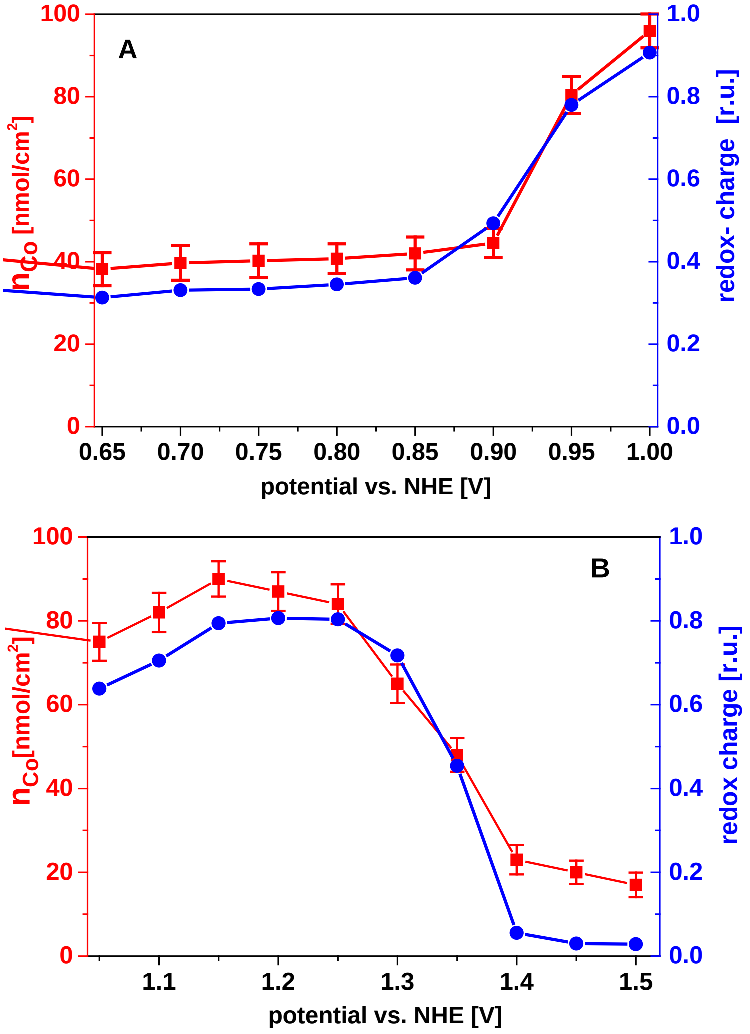

Figure 2.6. Electrochemical potential vs. redox-charge (blue) and the amount of Co ions after operation of the CoCat for 3 hours (A) or 24 hours (B). The number of cobalt ions (nmol/cm²) was extracted by chemical analyses of catalysts after operated with TXRF. The redox-charge was normalized to initial CV. The initial amount of cobalt atoms in the as-deposited film was 100 nmol/cm^2. The initial transferred redox-charge during the cathodic scan of the first CV was approximately 3.5 mC/cm^2. Lines added to the Figures are a guide to the eye.

After CoCats were operated in Co-free buffer for 3 hours at non-catalytic potentials and 24 hours at catalytic potentials, all samples were dried at ambient conditions (temperature and pressure). Then UV-Vis absorption experiments were conducted. Figure 2.7 demonstrates that the absorption at 450 nm is proportional to the amount of cobalt ions present in the film.

To have a visible comparison of the exact amount of samples with UV-Vis, the result was plotted in Figure 2.8. This outcome supports that sample has more cobalt atoms, the amount of its absorption is higher.

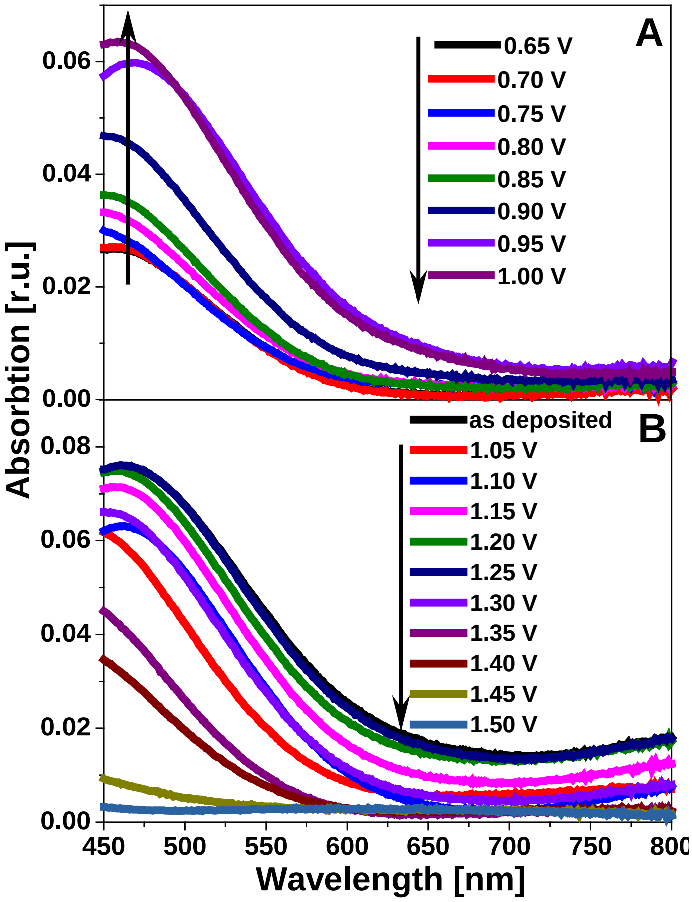

Figure 2.7. UV-vis absorption spectra of CoCat samples after operation at non-catalytic (A: 3 hours) and catalytic (B: 24 hours) potentials indicate differences in the Co concentration. After operation, all samples were dried in air. UV-vis spectra were recorded at open circuit potential in 0.1 M KP_i pH 7.

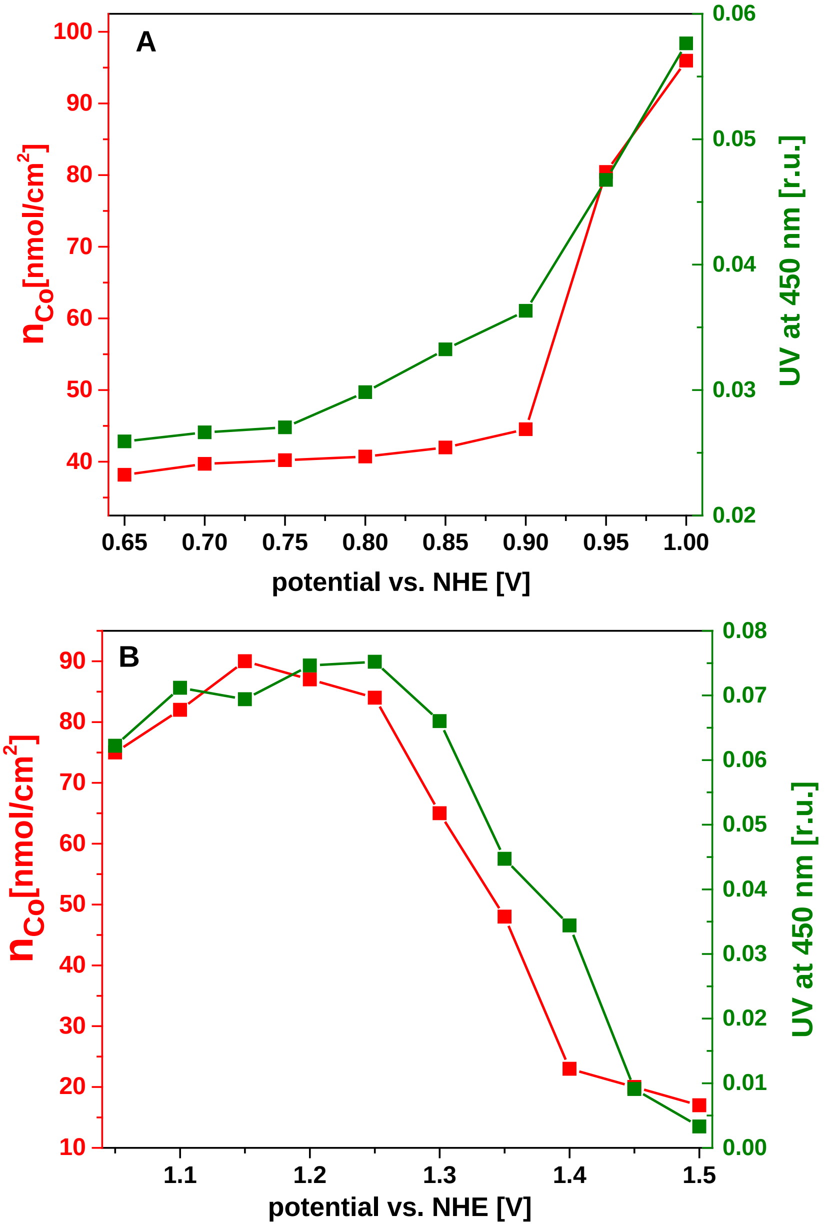

Figure 2.8. Quantification of CoCat samples (left axis) operated for 3 hours (A) and 24 hours (B) were measured by TXRF compared to the UV-vis absorption spectra (right axis). These data were extracted from Figures 2.6 and 2.7. After operation, all samples were dried in air. UV-vis spectra were recorded at open circuit potential in 0.1 M KP_i pH 7.

To exclude possible artifacts and/or electrochemical changes induced by the CVs (taken every 30 minutes) on the number of redox-active cobalt atoms and the catalytic current density, the protocol was run without intermittent cyclic voltammetric scans for selected potentials (Co-free electrolyte, 24 hours). The results in Figure 2.9 state that such effects are small.

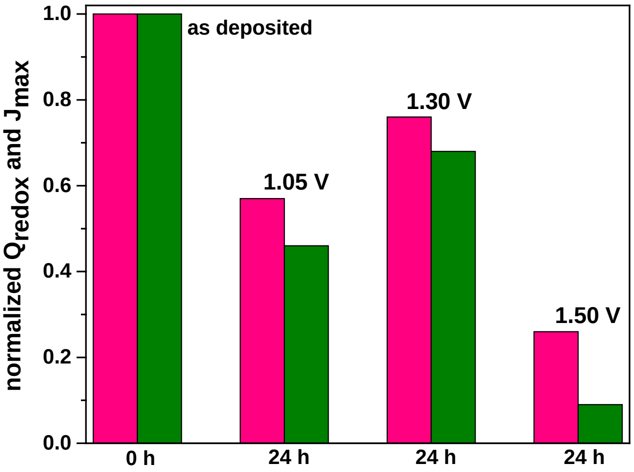

Figure 2.9. To exclude large effects of the intermediate CVs taken every 30 minutes the redox-activity (pink bar) and the catalytic current density (green bar) of CoCat, samples were determined only after electrodeposition and after operation for 24 hours at selected potentials. All samples were operated in Co-free buffer (0.1 mol L^{-1} KP_i). The results are similar to those presented in Figure 2.3. The mean value of the redox-charge and the catalytic current density of the initial CV of all samples were about 3.5 mC/cm^2 and 2 mA/cm^2, respectively.

2.3 Summary

The long-term performance of the CoCat operated in KP_i at pH 7, in Co-free buffer was investigated. The following conclusions can be drawn.

- CoCat is not stable when no current is flowing (OCP); after 24 hours, more than 80 % of the initial amount of cobalt is dissolved.
- At low potentials (< 1.0 V vs. NHE) and elevated potentials (> 1.3 V vs. NHE) the activity drop exceeds 50 % after 24 hours of operation. Under these conditions, CoCat is dissolving quickly at low as well as at elevated potentials. Therefore, a narrow potential range (1.1 < V vs. NHE < 1.35) is suggested as an optimal potential window for having a comparably stable CoCat, where reasonable activity is maintained after 24 hours.
- TXRF results combined with quantification of the negative CV area reveals that the absolute amount of cobalt present is following the trend of the redox activity. This is also confirmed by UV-vis results.

Chapter 3

Self-healing of cobalt catalyst in Co-containing buffer

As we already discussed in chapter 2, when cobalt oxide catalyst (CoCat) is operated in Co-free phosphate buffer the catalyst remains more than half after 24 hours operation, but a significant fraction of the activity of cobalt atoms gets lost during operation at optimal window potential for having a pretty stable CoCat. This raises the question if the repair works only with additional Co-ions in solution and/or entirely due to them. This point is not immediately clear, since the proposed self-repair by re-deposition might also work with dissolved Co-ions initially being part of the catalyst, at least if the mechanism depends on the operating for intermediate potentials (1.15<V<1.35) and the presence of phosphate only.

For further analysis of the repair mechanism, CoCats were operated at catalytic and non-catalytic electrode potentials in different concentrations of Co-containing buffers.

Electrochemical data shows that operation of CoCat in 20 µmol L^{-1} Co-containing buffer is sufficient to achieve an almost stable performance (in terms of current density per geometrical surface area). However, in this case, the film thickness is growing significantly.

Portions of this chapter have been prepared for the publication that was mentioned in chapter 2.

3.1. Experimental Section

3.1.1 Materials and electrodeposition of Co oxides catalyst

Details of Materials and Electrodeposition are described in chapter 2.

3.1.2 Electrochemical characterization

After electrodeposition, the counter and reference electrode were cleaned with 30% nitric acid and MilliQ water (18.2 MΩ). Then CoCat was operated in Co-containing phosphate buffer (0.1 M KPi, pH 7) at various cobalt concentrations (3, 5, 10, 20, 30 and 40 µmol L^{-1}) at several selected catalytic and non-catalytic potentials for 24 hours. Cyclic voltammograms (0.65 – 1.40 V vs. NHE) with scan rates of 20 mVs^{-1} were run every 30 minutes to diagnose losses in redox-active cobalt ions and catalytic activity. The second CV scan was analyzed.

3.1.3 Evaluation of deposited material by TXRF

The details of the quantitative chemical analysis using a total reflection X-ray fluorescence (TXRF) instrument (PicoFox, Bruker) is explained in section 2.1.4.

3.1.4 Tafel-slope

Tafel analysis of CoCat samples operated in Co-free and Co-containing buffer was performed to gain insight into electro-kinetic mechanistic details of the CoCat. Data for CoCat Tafel slopes have been recorded after electrodeposition and also after 24 hours as well as 48 h of operation at 1.3 V in KPi buffer (0.1 M KPi, pH 7). The steady-state currents of all experimental series were acquired at ambient temperature and pressure. The Tafel data were collected by applying the desired potential (from 1 to 1.45 V vs NHE in 10 mV steps) for 60 seconds, and averaging the last 10 s of the steady state current density. Then the current density versus potential was plotted and the inverse slope in a liner region (> 1 V vs. NHE) was extracted.

3.1.5 Scanning electron microscopy (SEM)

SEM was performed with Hitachi SU 8030 instrument operated at 10 kV and 10 mA with an XY detector in a working distance of 8 mm. CoCat samples were prepared as described in chapter 2. SEM was performed by Paul Kubella.

3.2 Results and Discussions

3.2.1 Optimization of cobalt concentration

After electrodeposition and proper cleaning the CoCat was operated in differently concentrated cobalt containing phosphate buffers (3, 5, 7,10, 15, 20, 30, 40, 60, 125, 250, 500, 1000, 2000 µmol L^{-1} in 0.1 M KP_i) for 24 hours at 1.3 V vs. NHE. We observed that under operation in cobalt concentrations ≥ 60 µmol L^{-1} some parts of the CoCat fall off into the solution (Figure 3.1). To avoid degradation of the CoCat during daily operation, we have chosen lower cobalt concentrations in phosphate buffer, namely; 3, 5, 10, 20, 30, 40 µmol L^{-1}

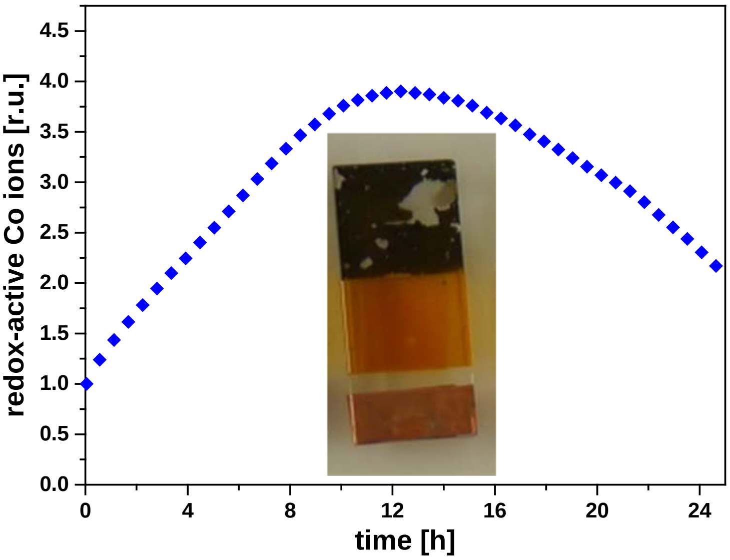

Figure 3.1. Amount of redox-active Co ions vs. time (blue squares) of CoCat operation at 1.3 V vs NHE in 0.1 M KP_i with 100 µmol L^{-1} of Co. The photo shows that CoCat operated at high cobalt concentration > 60 µmol L^{-1} is not stable and some parts of catalyst fall off.

3.2.2 Self-healing of CoCat in Co-containing buffer

When CoCat is operated in Co-free phosphate buffer, the catalyst remains more than half after 24 hours operation, but a significant fraction of the activity of cobalt atoms gets lost during operation at 1.1 < V vs. NHE < 1.35 V (Figures 2.4 and 2.5). This raises the question if the repair works only with additional Co-ions in solution and/or entirely due to them. This point is not immediately clear, since the proposed self-repair by re-deposition might also work with dissolved Co-ions initially being part of the catalyst, at least if the mechanism depends on the operating for intermediate potentials (1.15<V<1.35) and the presence of phosphate only.

For further analysis of the repair mechanism, CoCats were operated at catalytic and non-catalytic electrode potentials in different concentrations of Co-containing buffers (10, 20, 30 and 40 µmol L^{-1}) and cyclic voltammograms were run every 30 minutes in order to diagnose losses in redox-activity or the catalytic activity. The additional Co^{2+} in the solution could potentially compensate for the lost cobalt during operation- if re-deposition takes place and leads to catalytically active sites. Although this protocol is closer to similar previously reported results (Kanan and Nocera 2008), we decided to use a more than one order of magnitude lower concentration of Co ions, because when CoCat is operated at high concentration for 24 hours the thickness of the film is growing too much and some parts of the film fall off into the solution.

Figures 3.2 and 3.3 illustrate the time dependency of redox-active cobalt ions and the catalytic current (taken from CVs) at various electrode potentials (0.90 – 1.50) over the time course of 24 hours.

Figure 3.2-A and B displays that if CoCat is operated at 0.9 V vs. NHE with a Co^{2+} concentration of < 40 µmol L^{-1} the rate of dissolution is higher than self-assembling of the catalyst because the amount of redox-active ions is lower than the initial amount. However, this rate is almost the same when CoCat is operated in 40 µmol L^{-1} Co- concentration although the catalytic current after 24 hours operation is slightly lower than the initial amount.

Operation at 0.95 V shows a similar trend of the catalytic current as operation at 0.90 V. However, the amount of redox-active Co ions is clearly enhanced over the elapsed time at high Co concentrations (30, 40 µmol L^{-1}), constant at intermediate ones (20 µmol L^{-1}), and decreasing at low ones (10 µmol L^{-1}).

If the CoCat is operated at higher potentials (1.0 and 1.05 V vs. NHE) the amount of redox-active cobalt ions increases with increasing the amount of Co^{2+} ions in the buffer solution. The amount of redox-active cobalt ions are two or three times higher than the initial amount when CoCat is operated at 40 µM at 1.0 or 1.05 V, respectively. However, the catalytic current is almost the same as-deposited sample.

Operation at 1.0 V and 1.05 V vs. NHE further reveal that the catalytic current is not exactly following the trend of the amount of cobalt active ions because when samples are operated at cobalt-containing buffer within initial 20 hours, the redox-active cobalt ions increased while the catalytic current decreased. After this time, the trend is following each other.

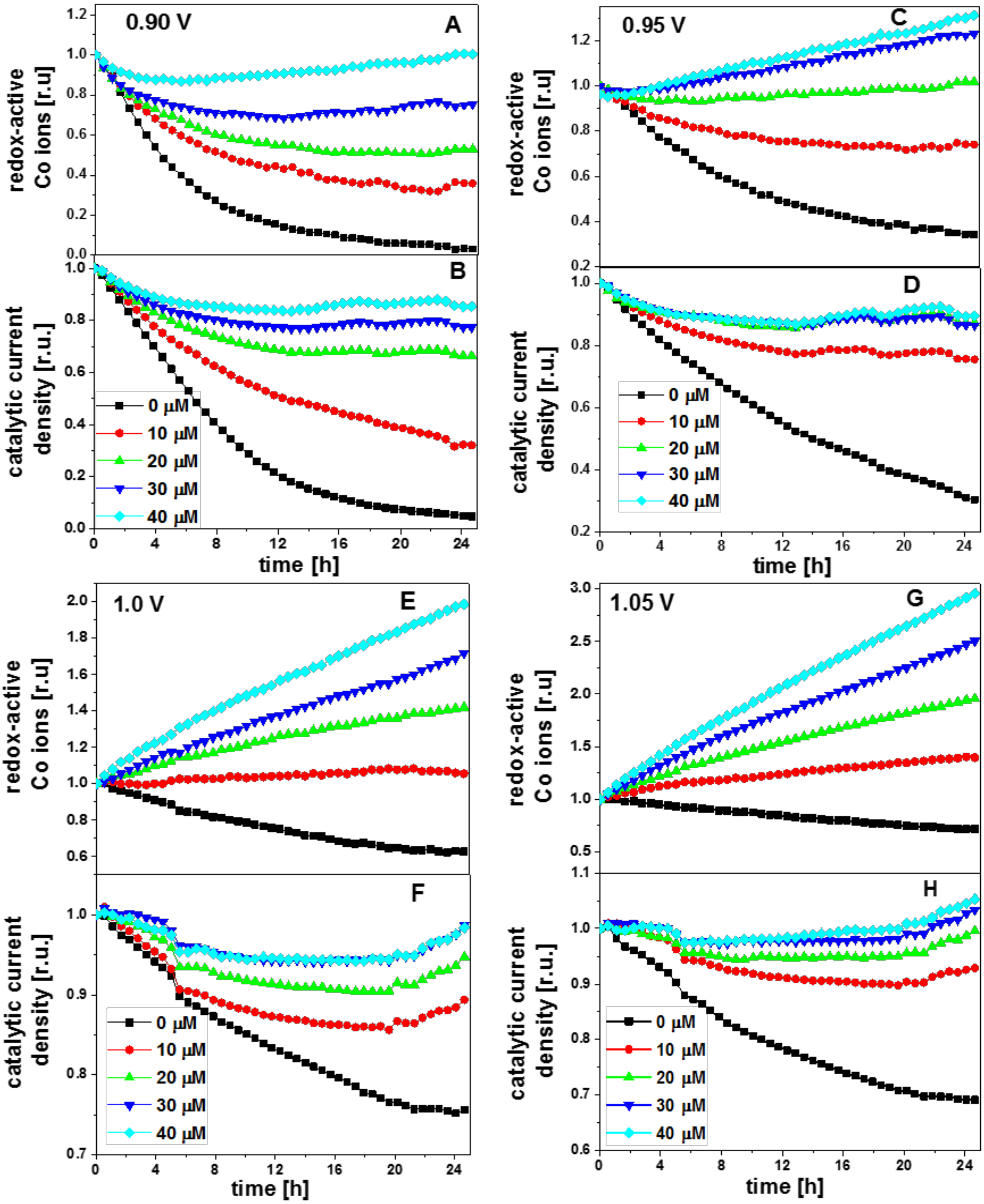

Figure 3.2. Amount of **redox-active cobalt ions** and **catalytic current density** normalized to the initial CV from different CoCat samples, each operated in KP$_i$ buffer at pH 7 containing various Co^{2+} containing buffers for 24 hours at following potentials versus NHE: **0.90 V** (A, B), **0.95 V** (C, D), **1.0 V** (E, F), **1.05 V** (G, H). The mean value of the redox-charge and the catalytic current density of the initial CV of all samples were about 3.5 mC/cm^2 and 2 mA/cm^2, respectively.

Figure 3.3 shows that under operation at catalytic potentials the amount of redox-active cobalt ions of CoCat sample is increased. This finding is a strong indicator that an additional deposition of Co-oxide happens at the electrode. If the CoCat is operated in 10 µmol L^{-1} Co-containing KP_i buffer the amount of redox-active cobalt ions is growing gradually during operation for all potentials while the catalytic current is lower than the as-deposited sample.

If the CoCat is operated in 20 µmol L^{-1} Co-containing KP_i buffer at low catalytic potentials (<1.35 V vs. NHE) the catalytic activity is almost the same as-deposited sample (B, D, F, H, J), although the amount of redox-active Co ions is more than two times higher than as-deposited film. Operation of CoCat in Co-concentrations with more than 20 µmol L^{-1} causes an increase in the catalytic current by maximally 20% over the course of 24 hours. Under these conditions the amount of redox-active cobalt ions increases by a factor of four.

The results shown in Figure 3.3 (**I, J**) uncover a clear discrepancy between the current density and the redox activity. When the CoCat is operated in 3 µmol L^{-1} Co^{2+} containing buffer the redox activity is almost stable, however, the catalytic current is diminished by ~ 20 % and the latter one is increasing by a factor of 400 % (40 µmol L^{-1}) within the 24 hours. On the other hand, the catalytic current density with an increase of less than 10 % is by far not as sensitive as additional Co^{2+} in the buffer.

It is surprising that increasing the potential more than 1.3 V when CoCat is operated in 20 µmol L^{-1} Co-containing (or lower) the catalytic current density cannot reach the initial value after 24 hours although it was higher than initial for low catalytic potentials (1.1 <V<1.3). Operation at 1.35 V in higher Co concentrations more than 20 µmol L^{-1} can only keep constant the catalytic current but the thickness of the film increase more than factor three.

Increasing the operation potential to 1.4 V (Figure 3.3-M and N) makes almost constant catalytic current density if CoCat is operated in 30 µmol L^{-1}. However, increasing the cobalt concentration to 40 µmol L^{-1} cannot help to improve the catalytic current density and after 16 hours of operation, the rate of reassembling is higher than dissolution because the redox-active ions decreased.

If CoCat operated at 1.45 V and 1.50 V in 20 µmol L^{-1} cobalt concentration buffer or lower the redox-activity gradually increase, but the catalytic current continuously decreased. However operation at higher cobalt concentration makes an increase in redox-activity for the first 8 hours of operation, then some parts of catalyst fall off into the solution (O, Q), which is possible to see by eye. We can conclude that operation in higher concentrations than 20 µmol

L^{-1} cannot improve the self-assembling properties of the CoCat over an extended time scale (a day).

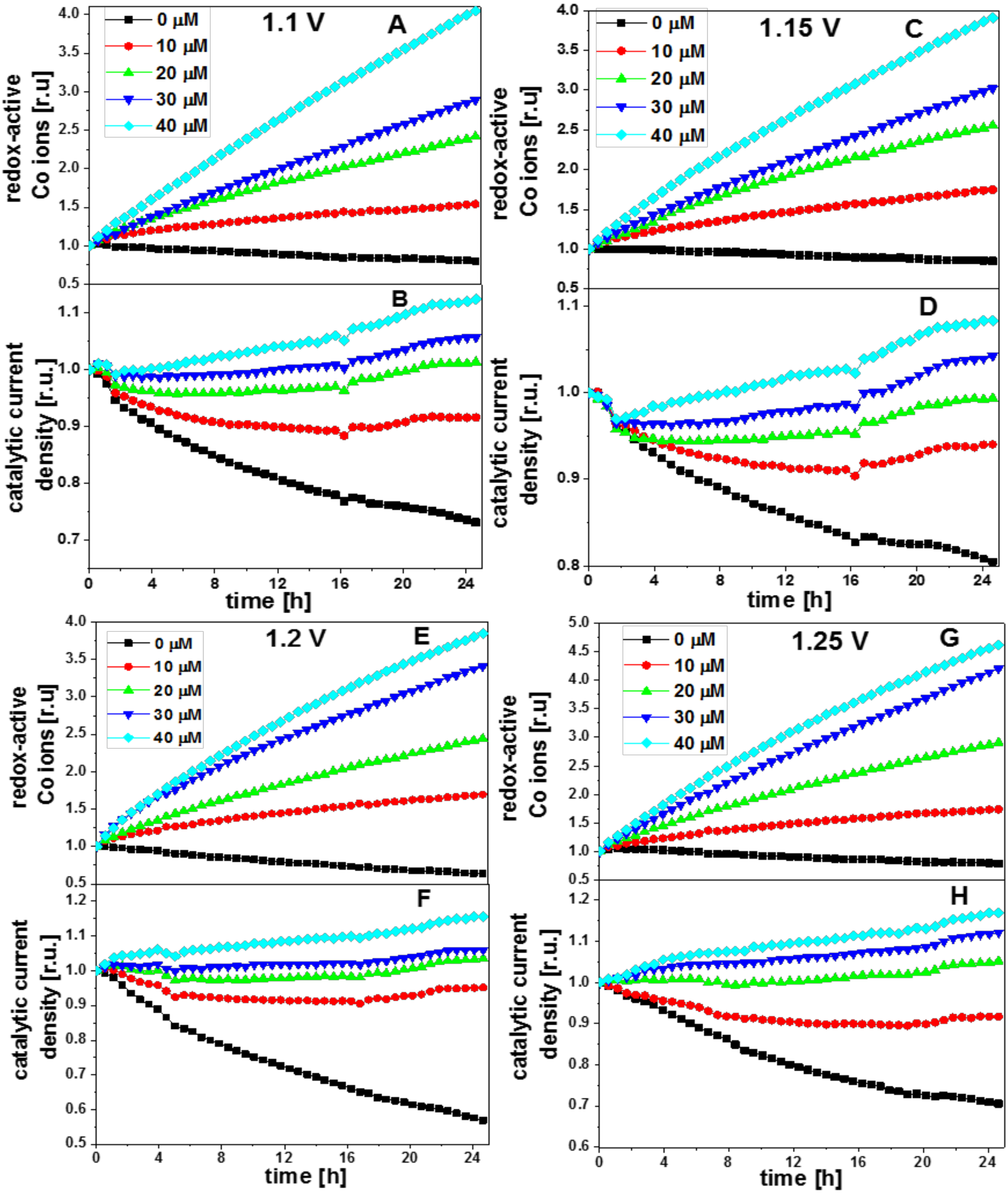

Figure 3.3 (first part). Amount of **redox-active cobalt ions** and **catalytic current density** normalized to the first CV from different CoCat samples, each operated in KP$_i$ buffer at pH 7 containing various Co^{2+} containing buffers for 24 hours at following potentials versus NHE:**1.1 V** (A, B), **1.15 V** (C, D), **1.2 V** (E, F), **1.25 V** (G, H). The amount of redox-active cobalt ions growths with increasing the amount of additional Co^{2+}, which indicates additional deposition of Co-oxide at the electrode. The mean value of the redox-charge and the catalytic current density of the initial CV of all samples were about 3.5 mC/cm^2 and 2 mA/cm^2, respectively.

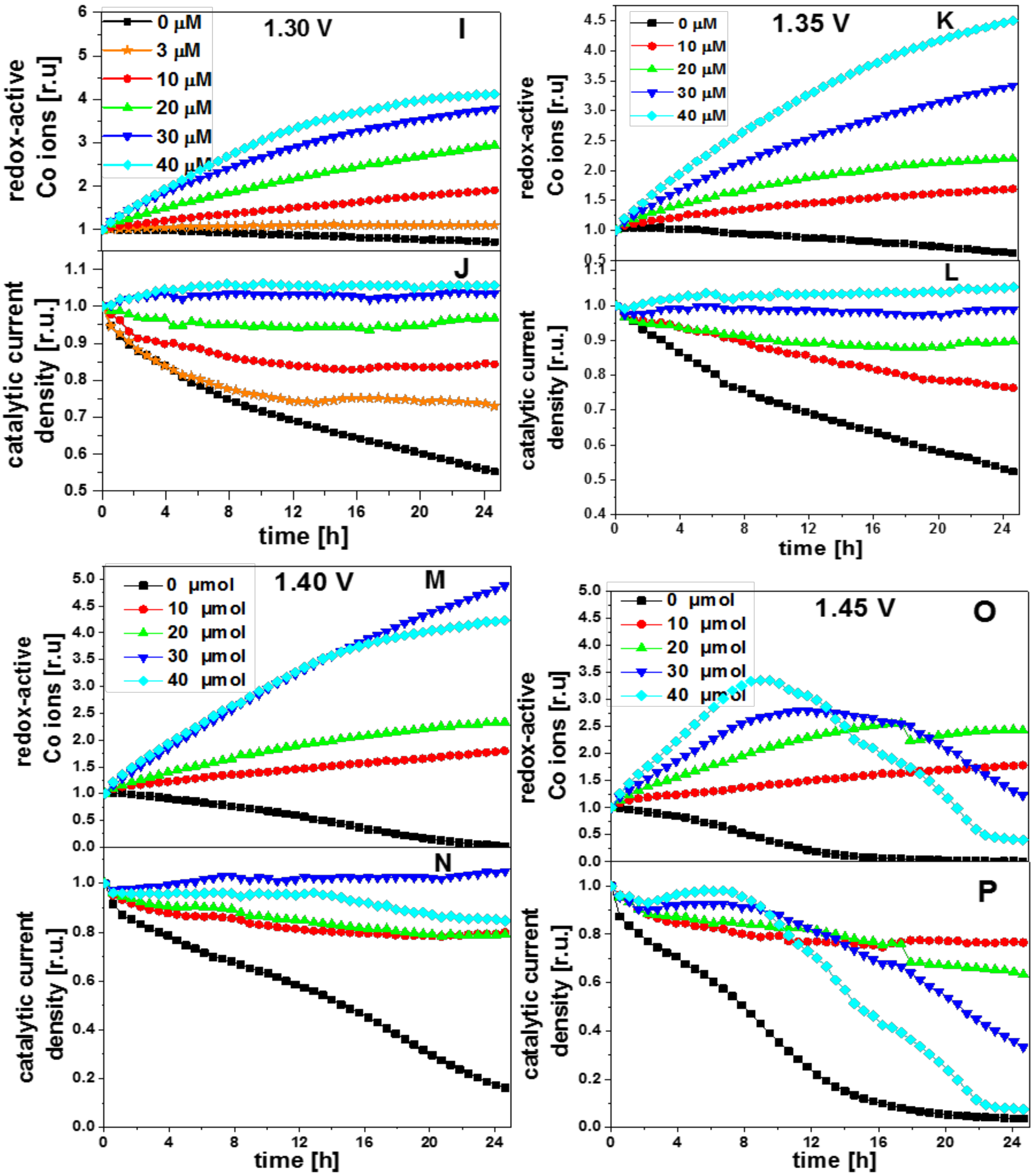

Figure 3.3 (second part). Amount of **redox-active cobalt ions** and **catalytic current density** normalized to the first CV from different CoCat samples, each operated in KP$_i$ buffer at pH 7 containing various Co^{2+} containing buffers for 24 hours at following potentials versus NHE: **1.3 V** (I, J), **1.35 V** (K, L), **1.4 V** (M, N), **1.45 V** (O, P) The amount of redox-active cobalt ions growths with increasing the amount of additional Co^{2+}, which indicates additional deposition of Co-oxide at the electrode. The mean value of the redox-charge and the catalytic current density of the initial CV of all samples were about 3.5 mC/cm^2 and 2 mA/cm^2, respectively.

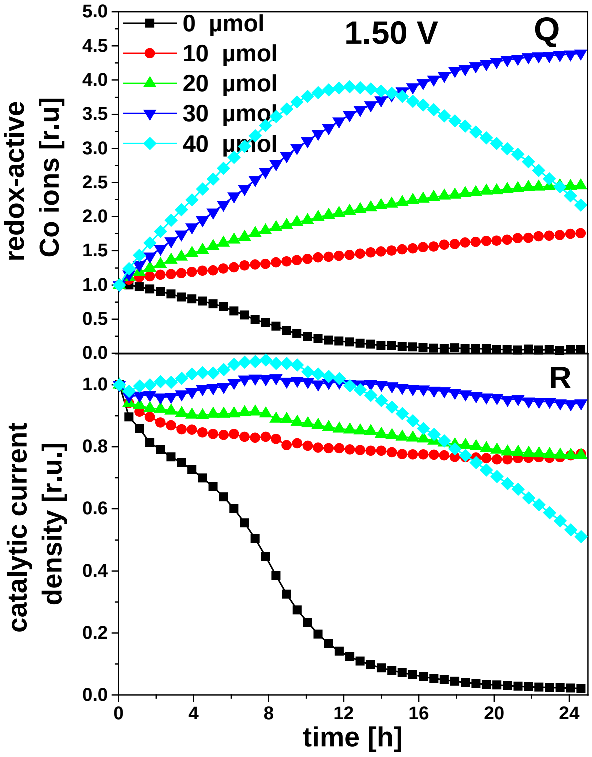

Figure 3.3 (third part). Amount of **redox-active cobalt ions** and **catalytic current density** normalized to the first CV from different CoCat samples, each operated in KP_i buffer at pH 7 containing various Co^{2+} containing buffers for 24 hours at following potentials versus NHE: **1.5 V** (Q, R),

The amount of redox-active cobalt ions growths with increasing the amount of additional Co^{2+}, which indicates additional deposition of Co-oxide at the electrode. The mean value of the redox-charge and the catalytic current density of the initial CV of all samples were about 3.5 mC/cm^2 and 2 mA/cm^2, respectively.

Chemical analysis (TXRF) after 24 hours of operation in various Co-containing phosphate electrolytes at various potentials, confirms the results of the electrochemical characterization (Figure 3.4). Similarly, it shows an increase in the absolute amount of Co ions present at the electrode, but exceeding the increase determined by electrochemical characterization (redox charge from the CVs of Figure 3.3), which means that not all cobalt atoms are catalytically active.

Figure 3.4 shows an analysis of Co-concentration, redox activity and catalytic current density for catalysts operated in different Co-containing KP_i- buffer solutions at different potentials. The absolute Co amount and the redox activity appeared to depend linearly on the Co-concentration, whereas the catalytic current density did not. It rather levels off for higher potentials. This could mean that the pathway for a charge (electrons, ions) inside the CoCat is more and more block by inactive sites when the film is growing. This would be in contradiction to previous findings of Klingan et al. (Klingan, Ringleb et al. 2014), but it should be noted that the reported current densities were only analyzed after one minute of operation. This work shows the importance of considering the operation time. From these data, a growth rate for both, the cobalt amount in the film as well as the redox activity independence of the additional added Co^{2+}, can be derived (Figure 3.5 A). At catalytic potentials (> 1.1 V vs. NHE) they are a linear function of this Co^{2+}-concentration.

Note the difference between these rates: Although the growth rate for the redox activity and the Co-amount are both linearly depending on the added Co^{2+}, they are very different in magnitude, the (normalized) catalytic current is not even increasing consistently with the Co^{2+} added.

For samples operated without additional Co^{2+} from Figure 2.5-B a decay rate due to film dissolution has been derived and is depicted in Figure 3.5-B.

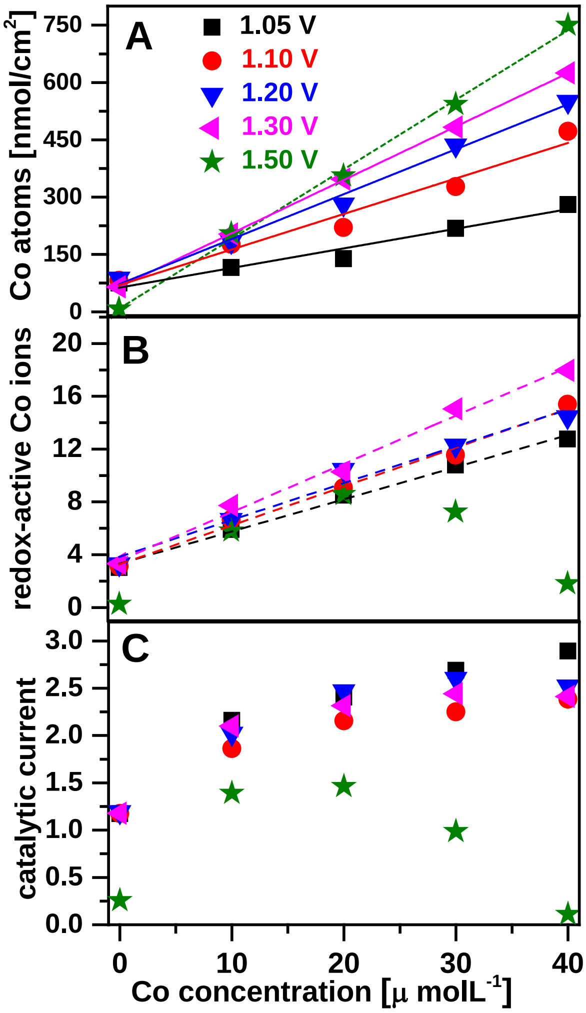

Figure 3.4. Amount of cobalt ions (in µmol L^{-1}) as determined by TXRF (A), redox charge (B) and catalytic current density (C) of different films operated for **24-hours** in Co-containing buffers at various potentials. The redox charge has been extracted from the integrated redox peak area in the cathodic scan of the cyclic voltammogram. The growth rate derived from the data in panel A is depicted in Figure 3.5 A.

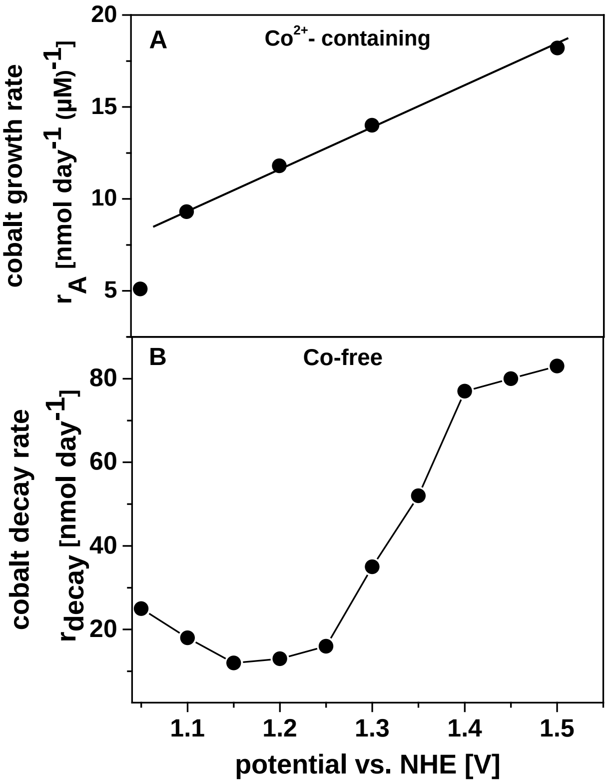

Figure 3.5. (A) The growth rate of CoCat films operated at different potentials in various Co^{2+} containing buffers (the increasing rate of Co-amount per day were taken from Figure 3.4 A). **(B)** Cobalt-concentration decay rate of CoCat samples operated at different potentials in Co-free buffer as derived from Figure 2.6 B. All rates refer to a unit area of 1 cm^2.

The repair of CoCat apparently requires additional Co-ions, which can be associated with a film growth, deviating quantitatively from TXRF. The mechanism of this recovery process is probably not only functioning because of an equilibrium between dissolution and re-deposition ending up in a stable state, but also influenced by other factors such as buffer properties, structural rearrangements, altered redox kinetics etc. Where does the discrepancy between those quantities (redox activity and film thickness) come from?

As the phosphate buffer is described to be the crucial component in the self-repair mechanism(Lutterman, Surendranath et al. 2009), it is worthwhile to investigate the correlation between those buffer properties and the catalytic activity. Responsible for the loss in activity could be a local gradient of protonated phosphate ions or reduction of phosphate at the counter electrode, what is still very unlikely at the potentials investigated here. Thus we carried out the following experiments.

First, we conducted the usual 24-h experiment using operation voltages of 1.05 V (electrodeposition potential of the films) and 1.3 V vs. NHE (catalytic potential) and four Co^{2+}

concentrations (0, 10, 20, 30, 40 µmol L^{-1}). After operation, the buffer solution was stirred for several minutes and the pH determined to be still 7.00 (+/- 0.05). Then the electrodes were reattached, and the 24-h protocol repeated. The results are shown in Figures 3.6 and 3.7, indicating no significant changes in the current density and the redox activity (aside from a small offset for a minor fraction of the samples).

The second experiment has been done accordingly – after 24 hours the buffer was exchanged against a fresh one. In agreement with the experiment mentioned before no dramatic changes were obtained in both, the catalytic current density and the redox activity (Figure 3.8) when the buffer solution had been exchanged after 24 h.

These experiments exclude two possible explanations for the different behavior of catalytic activity and redox capability. First, a significant change in the local pH and second a consumption of phosphate. The loss in activity is not related to the buffer properties.

To validate the trends already shown for the 24-hour experiments, TXRF has been applied for the 48 hours experiments. The results can be found in Figures 3.9 and 3.10.

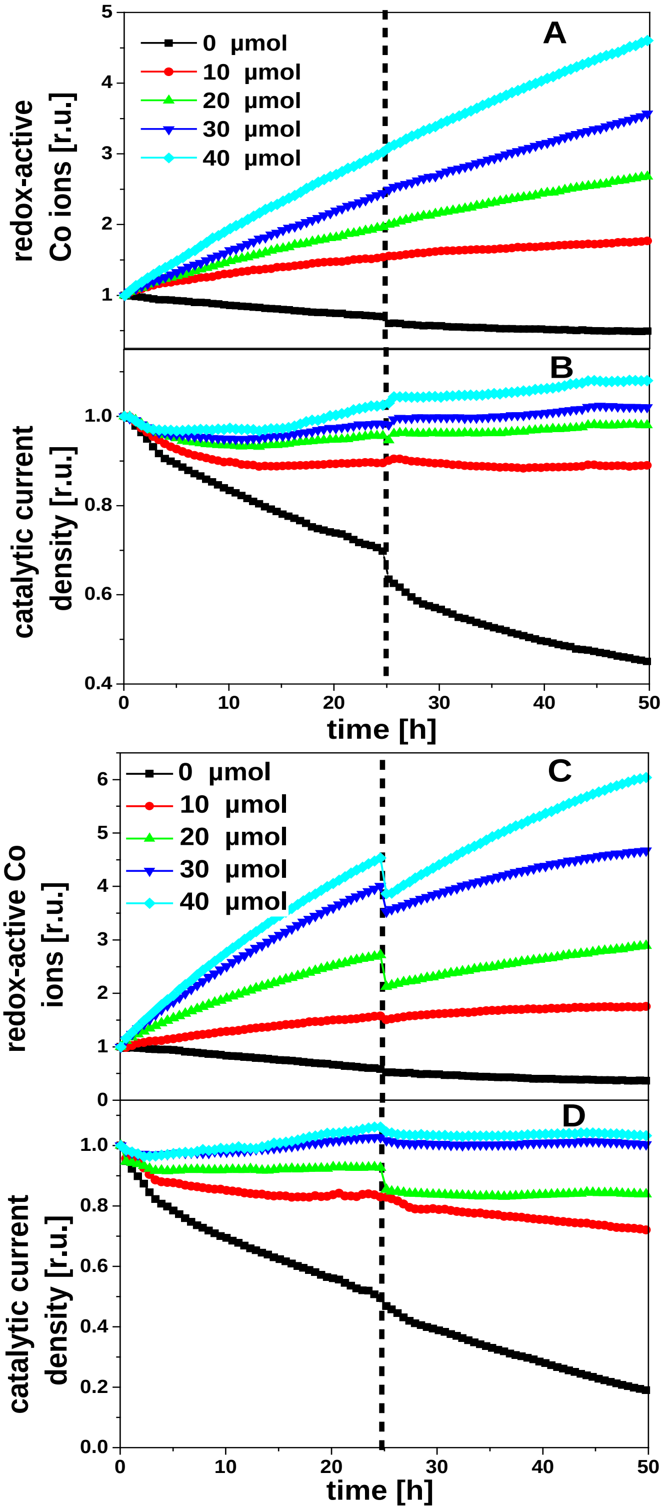

Figure 3.7. Redox-active cobalt ions **(A,C)** and catalytic current density **(B,D)** CoCat samples in 0.1 M KP$_i$ at pH 7 operated at **V=1.05 V** (A,B) and **1.3 V** (C,D) in various Co-containing buffers for 48 hours. After 24 hours **the buffer solution was thoroughly stirred** and it was again operated for 24 hours. The pH has been measured at the beginning and after 24 and 48 hours without significant changes being observed. The mean value of the redox-charge and the catalytic current density of the initial CV were about 3.5 mC/cm^2 and 2 mA/cm^2, respectively.

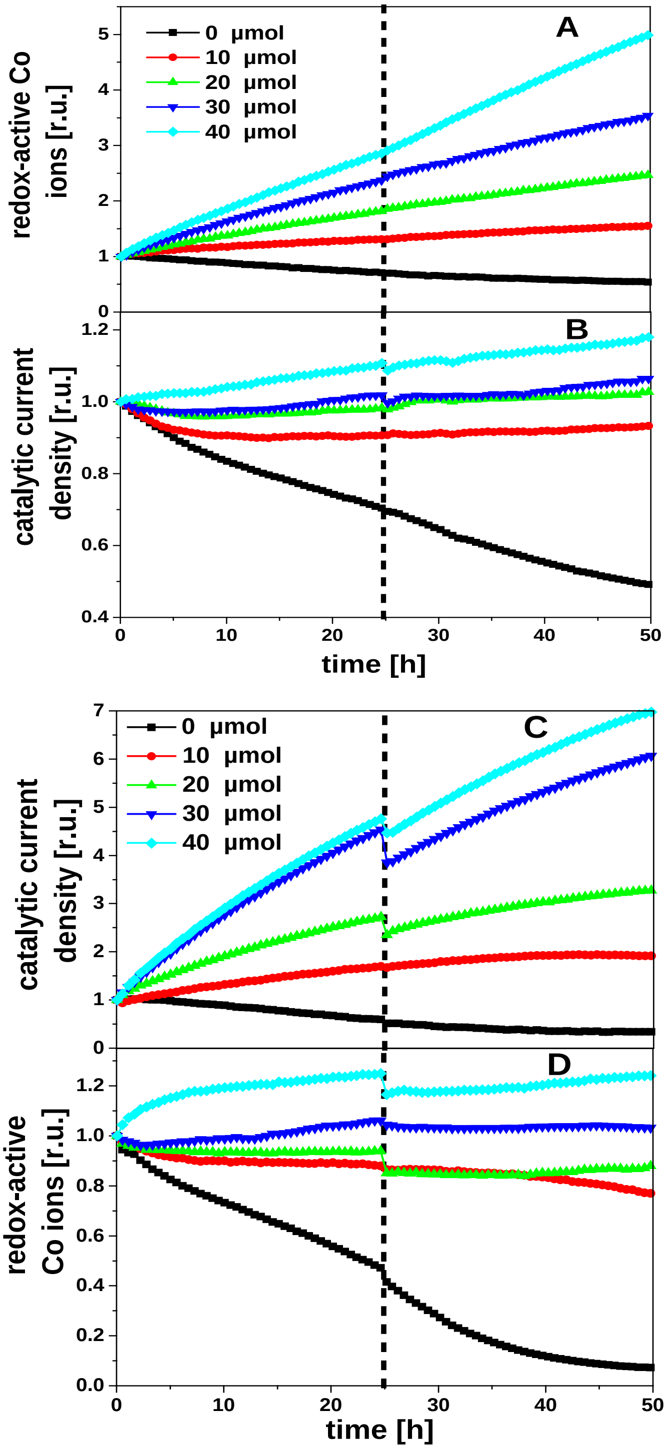

Figure 3.8. Redox-active cobalt ions **(A,C)** and catalytic current density **(B,D)** CoCat the samples in 0.1 M KP_i at pH 7 operated at **V=1.05 V** (A,B) and **1.3 V** (C,D) in various Co-containing buffers for 48 hours. After 24 hours **the buffer solution was exchanged** and it was operated for 24 hours again. No buffer consumption was observed during operation. The mean value of the redox-charge and the catalytic current density of the initial CV were about 3.5 mC/cm^2 and 2 mA/cm^2, respectively.

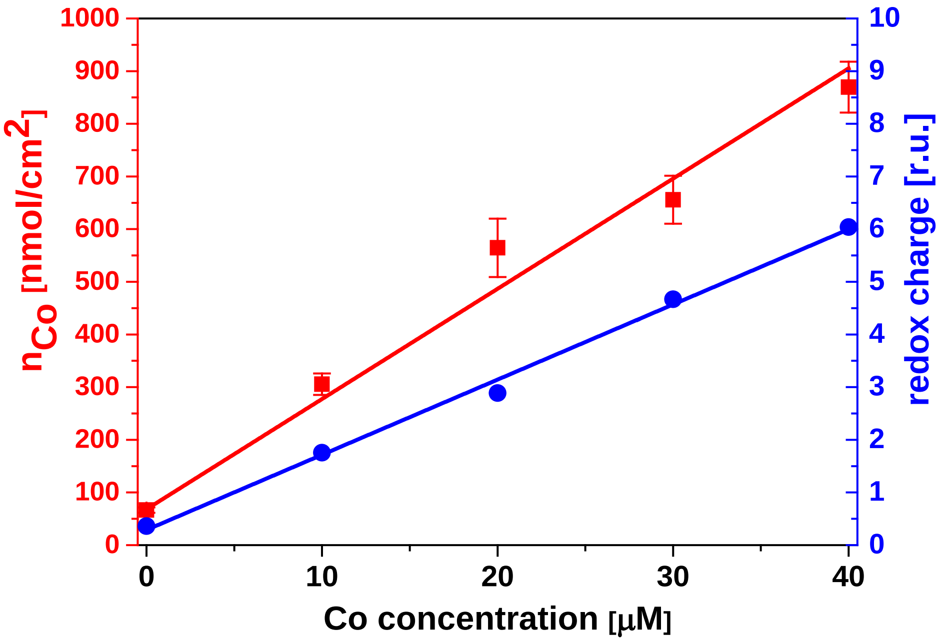

Figure 3.9. The amount of cobalt atoms of samples operated at V = 1.3 V in different cobalt containing buffers for 48 hours**. After 24 hours operation, the buffer solution was stirred** and it was operated for 24 hours again. Left Y-axis shows the absolute amount of cobalt obtained by chemical analysis. The redox-charge has been normalized by the redox charge of the first cycle (t=0) and is shown on the right axis. The Co amount at the beginning was 100 nmol/cm^2. The redox-charge of the initial CV was approximately 3.5 mC/cm^2.

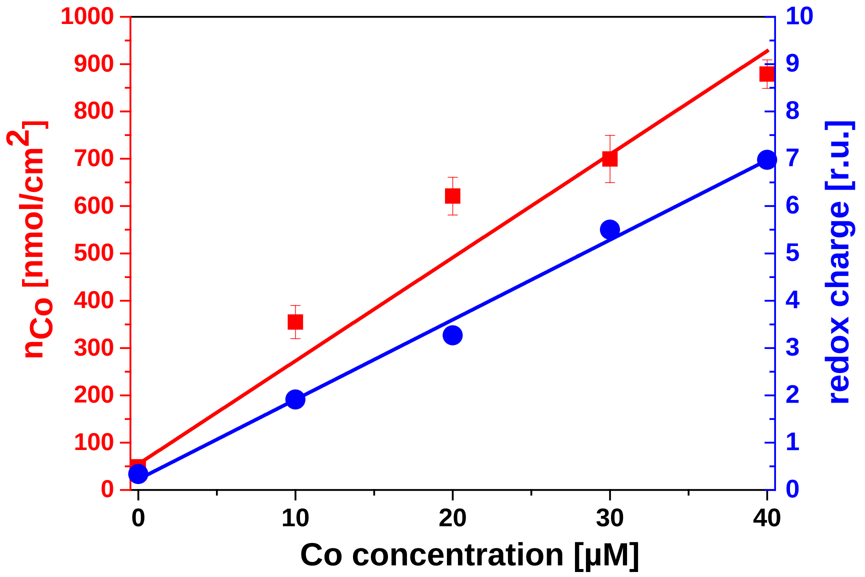

Figure 3.10. The amount of cobalt atoms of samples operated at V = 1.3 V in different cobalt concentration for 48 hours. **After 24 hours operation, the buffer has been exchanged** to a fresh one and again operated for 24 hours. Left Y-axis shows the absolute amount of cobalt obtained by chemical analysis. The redox-charge has been normalized by the redox charge of the first cycle (t=0) and is shown on the right axis. The Co amount at the beginning was 100 nmol/cm. The redox-charge of the initial CV was approximately 3.5 mC/cm^2.

To understand the catalytic mechanism of samples operated in Co-free and Co-containing buffer, the Tafel slope of CoCat has been investigated during two days of operation at 1.3 V vs. NHE (Figure 3.11).

Generally, if the nature of the catalyst stays unchanged and only suffers dissolution, the Tafel slope should stay constant during operation. On the other hand, the exchange current density might be lower due to a smaller number of active sites. A more complicated situation occurs if there are major changes in the activity of the active sites in the catalyst. According to that a changed Tafel slope is expected. Tafel plot data collected for CoCat show an anodic shift in potential with operation time.

According to the previous analyses, in Co free KPi (Figure 2.5) more than 30 % of CoCat is dissolving after 24 hours and the redox activity is dropping (Figure 2.4). Since the Tafel-slope is increasing by about 10 %, the degradation of the electrocatalytic performance of CoCat cannot be explained by dissolution alone. Additionally, structural changes of the active site might contribute to the degradation.

When CoCat is operated in 3 µM Co concentration the amount of redox-active Co ions is constant, while the film thickness is increasing by 5 % (Table 3.1). At the same time the catalytic current density is decreasing by 25 % (Figure 3.3).

On the other hand, if CoCat has been operated in 20 µM Co^{2+} concentration the catalytic current density appeared to be stable after one day. However, the film gets thicker by 300 %, the redox activity by 250 %.

In summary, this means that a stable performance of the CoCat, even though an addition of Co^{2+} to the buffer is alleviating the detrimental changes in catalytic performance, cannot be obtained with this catalyst. Either the film thickness is reasonably constant or the catalytic current density. A continuously growing film at constant current density will sooner or later lead to exfoliation of the catalyst or at least to serious transport limitations.

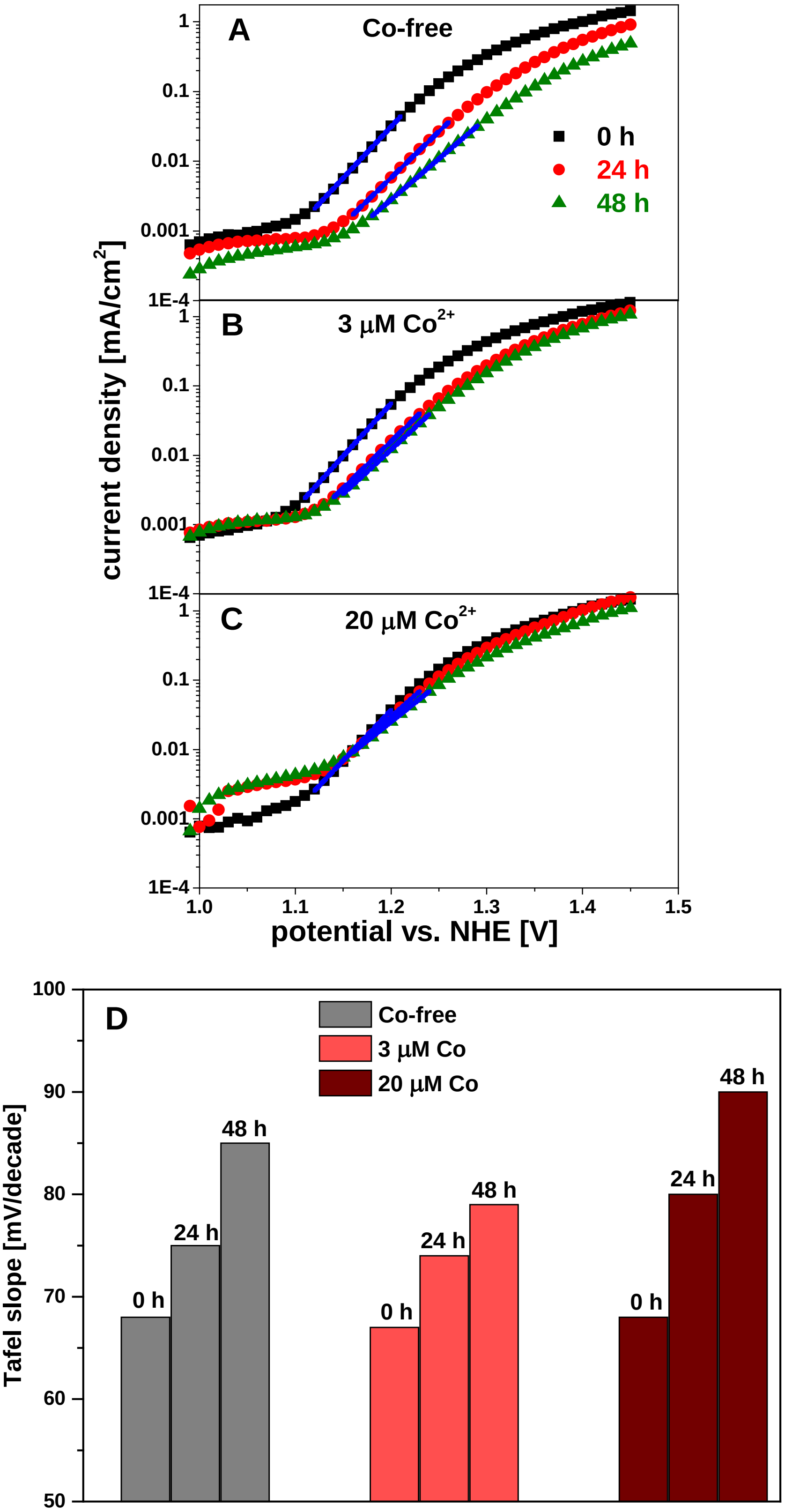

Figure 3.11. Tafel slopes of CoCats operated for 48 hours in **Co-free** (A), **3μM** (B) and **20 μM** (C) Co-containing buffer. The Tafel slopes are shown in **gray** (Co-free), **orange** (3μM Co-containing) and **brown** (20μM Co-containing) color in panel **D**.

Table 3.1. CoCat operated at 1.3 V vs. NHE for 24 hours in Co-free phosphate buffer **(A)**, 3 µM Co-containing buffer **(B)** and 20 µM Co-containing **(C)**. The catalytic current density and the redox-active cobalt ions extracted from Figures 3.3-I and J. The absolute amount of cobalt and the Tafel-slope in this table come from Figures 3.4-A and 3.11, respectively.

Sample	***Buffer***	***Current density (from CV)***	***Redox-active Co ions(from CV)***	***Absolute Co amount (from TXRF)***	***change in Tafel-slope after 24 hours***
A	Co-free; KPi	⬇ -40 %	⬇ -20 %	⬇ -35 %	⬆ +10 %
B	3 µM Co; KPi	⬇ -25 %	➡ 0 %	➡ (+5 %)	⬆ +10 %
C	20 µM Co; KPi	➡ 0 %	⬆ +250 %	⬆ +300 %	⬆ + 17 %

SEM images were recorded to get a visual impression of the morphology of the CoCat. The deposition charge was enhanced up to 30 mC cm^{-2} (instead of only 10 mC cm^{-2} for the electrochemical experiments) to guarantee a reasonable good image data quality.

Figure 3.12 shows that the as-deposited CoCat (A) and CoCat operated in Co-free phosphate buffer (B, C) have a highly similar surface morphology. However, operation in 20 µM Co^{2+}-concentration (D, Co-KP$_i$) causes increased roughness on the surface of catalyst, which can affect its catalytic current density.

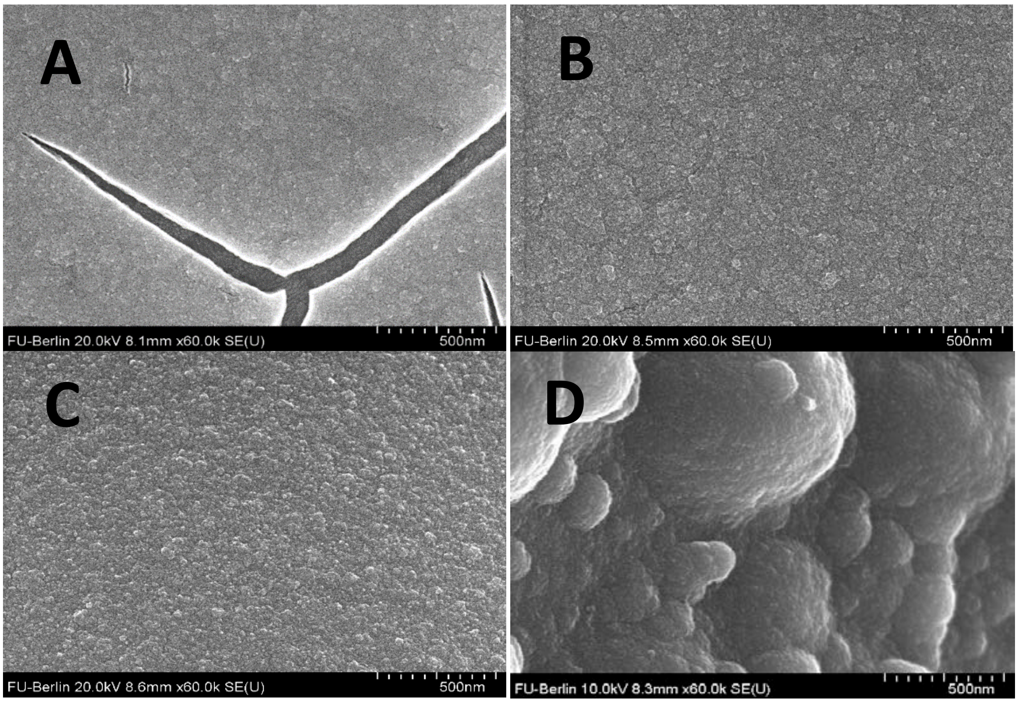

Figure 3.12. SEM images of CoCat as deposited **(A)**, operated in Co-free buffer (KP_i) for 15 minutes **(B)** and for 24 hours **(C)** as well as operated in 20 µM Co^{2+} concentration buffer (Co-KP_i) for 24 hours **(D)**. The operation potential was 1.3 V vs. NHE. After electrodeposition and operation, samples were rinsed with MilliQ water**.**

To extract the amount of cobalt, potassium and phosphorous, TXRF was carried out after 24 hours of operation in Co-free and 20 µM Co^{2+} containing buffer (KP_i, pH 7) at 1.3 V (Fig. 3.13). According to table 3.2, the L-emission lines of indium and tin overlap with the K-emission line of potassium so the CoCat was deposited on platinum instead of ITO. The energy of the X-ray K- and L-emission line of gallium (9880 eV and 1180 eV) are far from the K-emission energy of phosphorous (2013 eV) and potassium (~ 3313 eV), so cesium (L-emission line: ~ 4280 eV) was selected as a TXRF internal standard. However, the internal standard element for quantitative analysis of the cobalt amount was gallium.

According to the results in Figure 3.13-B, during operation the amount of P and K atoms per Co atom increases. This suggests that the number of K and P atoms surrounding Co is increasing while the catalytic current density is almost stable.

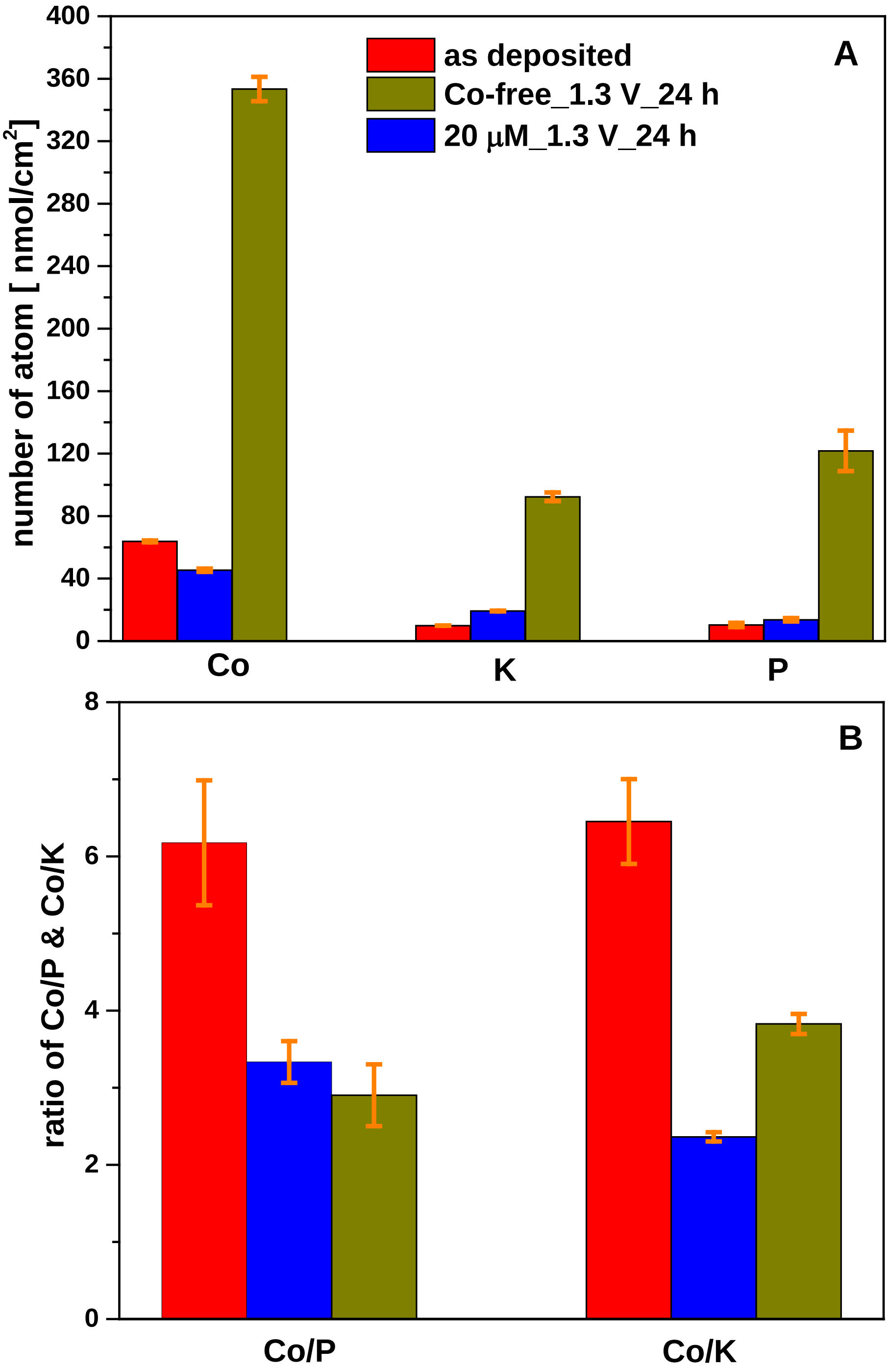

Figure 3.13. The number of cobalt, potassium and phosphor atoms **(A)** and the atomic ratio of these elements **(B)** of samples deposited on platinum substrates and operated for 24 hours in Co-free and 20 µM Co^{2+} containing buffer (KP_i, pH 7) at 1.3 V.

Table 3.2. Energies of X-ray emission lines of different elements (eV).

Element	Kα_1	Kα_2	Lα_1	Lα_2
P	2,013.7	2,012.7		
K	3,313.8	3,311.1		
Co	6,930.3	6,915.3	776.2	776.2
Ga	9,251.7	9,224.8	1,011.7	1,011.7
In	24,209.7	24,002.0	3,286.9	3,279.3
Sn	25,271.3	25,044.0	3,443.9	3,435.4
Cs	30,972.8	30,625.1	4,286.5	4,272.2

To maintain the activity during operation at 1.3 V over an extended time scale the amount of cobalt oxide deposited and thus the redox activity needs to be increased. During operation, there are slight changes visible in the redox waves of the CVs. For a more detailed insight into the redox changes the mean inflection points of oxidation and reduction waves of all CVs are plotted in Figure 3.14-B. This voltage shift can be responsible for the loss of activity as it is likely that an oxidized $Co^{3+/4+}$ species is needed for water oxidation catalysis.

Referring to the definition of a self-repairing or self-healing catalyst the following statement can be made: CoCat is not a self-healing catalyst by itself. However, introducing a slight amount of Co^{2+} to the electrolyte can maintain the catalytic activity in terms of current density for at least 24 hours. The turnover frequency, the film thickness and the overall kinetics as well as the structure change significantly. This is reflected by the fact that the initial current density level can only be reached by accumulating more material to the electrode as summarized in Figure 3.14-A.

That being said it has to be stated that the repair of the CoCat is non-autonomously. It still might be reasonable to speak about self-healing, but only with significant interference from outside. Moreover, as the deposition of CoCat dominates over dissolution, an operation for much longer times than 24 hours (weeks and longer) remains a challenge as structural changes, mass transport problems, exfoliation and unacceptably low turnover frequencies will play a role in either case.

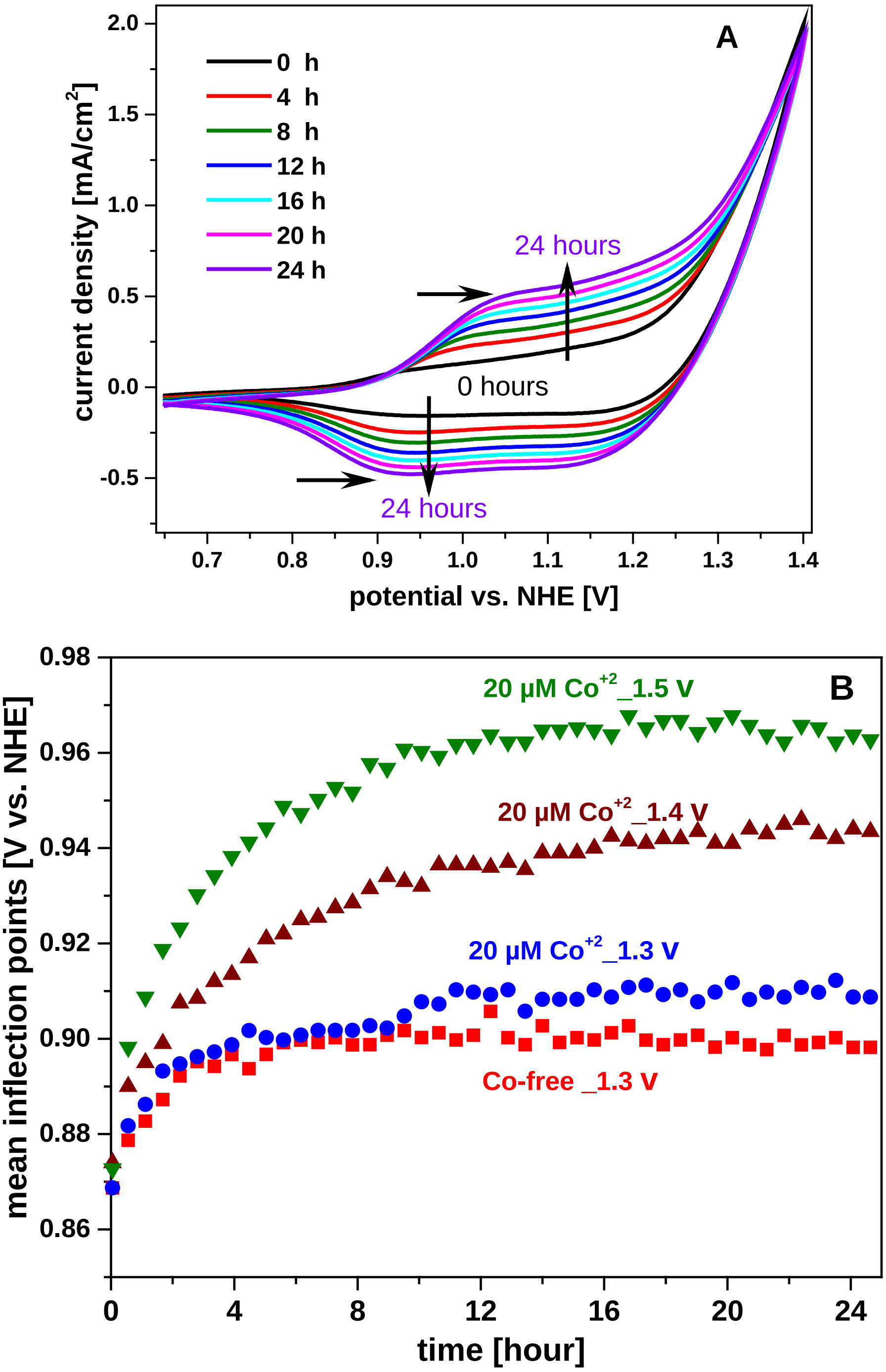

Figure 3.14. Cyclic voltammograms of samples operated for 24 hours in 20 µmol L^{-1} Co^{2+} containing buffer (KP_i, pH 7) at 1.3 V **(A).** The average inflection points of anodic and cathodic redox waves of all CVs of CoCat operated in Co-free and Co-containing KPi buffer at different potentials **(B).**

3.3 Summary

- I investigated the long-term performance of the CoCat operated in KP_i at pH 7, in Co-containing buffer. Striving for a stable performance of the CoCat, samples were operated in low concentration Co-containing buffer ($<$ 50 µmol L^{-1} Co^{2+}, 0.1 M KP_i) at catalytic and non-catalytic potentials. Operation in higher Co^{2+} concentrations causes some parts of the catalyst to fall off into the solution. It was found that a fairly low amount, namely a concentration close to 20 µmol L^{-1} - 25 times less than originally published and usually used for the electrochemical deposition (Kanan and Nocera 2008, Klingan, Ringleb et al. 2014) - is sufficient for maintaining the initial catalytic current. However, achieving an almost stable performance (in terms of current density per geometrical surface area) comes at the cost of a significantly growing film thickness.
- By adding only 3 µM Co^{2+} to the buffer and operating the sample at 1.3 V vs. NHE, the film thickness and the redox activity are basically constant, but now the current density decreases. The loss in activity is not related to a local gradient of protonated phosphate ions or reduction of phosphate at the counter electrode. During operation the Tafel slope is increasing, which might indicate structural changes in the film and therefore decreasing of performance of the CoCat. SEM image of sample is operated in 20 µmol L^{-1} Co^{2+}-concentration buffer (Co-KP_i) shows that after 24 hours operation the surface of the catalyst is drastically changed, and its roughness increased.

Chapter 4

Structural and functional changes in the CoCat

As already was discussed in chapter 3, ‘aging’ of the phosphate buffer has negligible influence on the catalytic performance. At the same time, it was shown that when CoCat is operated in Co-containing buffer, more and more cobalt is accumulated on the electrodes while almost a stable catalytic current was achieved after 24 hours operation. This suggested to consider the turnover frequency (TOF). The results show that The TOF goes down during operation in Co-free and Co-containing buffer, suggesting likely structural changes in the catalyst during operation.

XAS analysis shows that operation of CoCat in Co-concentration buffer enhanced molecular fragments size within the Co-oxide framework.

Redox kinetics of *in-situ* XAS slow down for CoCat after being operated for 24 hours and the oxidation state of cobalt catalyst stays almost constant during operation.

Portions of this chapter have been prepared for the publication that was mentioned in chapter 2.

4.1. Experimental Section

4.1.1 Materials

The details of the Materials were described in chapter 2.1

4.1.2 Electrodeposition of CoCat

Phosphate buffer solution (KP_i) was prepared as a mixture of approximately 40% KH_2PO_4 and 60% K_2HPO_4 at a total KP_i concentration of 0.1 $molL^{-1}$. The pH of the buffer has been verified by adjusting the pH to 7.00. For electrodeposition, concentrated $Co^{II}(NO_3)_2$ 6 H_2O (50 $mmolL^{-1}$) solution was added to the KP_i buffer such that the final concentration of the Co-electrolyte solution was 0.5 $mmolL^{-1}$. For low temperature (20 K) measurements 10 mC cm^{-2} CoCat have been deposited on ITO coated on glass (12 Ω per square, VisionTek Systems Ltd, Cheshire, UK) at a potential of 1.05 V vs. NHE. A geometrical area of 1 cm × 1 cm of the ITO was coated with the CoCat.

However, for *in situ* measurements, ITO/glass was substituted by polyethylene terephthalate (PET) slides coated with indium tin oxide (Sigma Aldrich Chemie GmbH Munich, GER), because glass would absorb a major fraction of the X-rays. Furthermore, for *in situ* XAS measurements, CoCat was deposited with two and a half times higher concentration (charge deposited) to improve the signal to noise ratio (25 mC/cm^2, KP_i, pH 7). A geometrical area of 1.4 cm × 1.4 cm of the CoCat was exposed to the electrolyte.

4.1.3 XAS sample preparation – Cryo measurement (20K)

After electrodeposition, all glassware was cleaned with diluted nitric acid and Millipore MilliQ water. The working electrodes (indium tin oxide on glass, Visiontek Systems Ltd) were cleaned with Ethanol and MilliQ water. A platinum mesh (25×25 mm^2) served as a counter electrode and an Ag/AgCl-electrode (≈200 mV vs. NHE, Metrohm) as a reference electrode. The distance between the working and reference electrode was about 0.5 cm.

After CoCat deposition, the cobalt-containing phosphate buffer was exchanged against a cobalt-free or less Co^{2+}-containing buffers (20 $\mu molL^{-1}$). CoCat samples were operated for 15 minutes (Co^{2+}-free) and 24 hours in Co-free and 20 $\mu molL^{-1}$ Co^{2+}-containing buffer (Co-KP_i). Subsequently, those samples have been rapidly frozen by immersion in liquid nitrogen.

4.1.4 *In-situ* XAS sample preparation – room temperature (293K)

One compartment PTFE cell with a quadratic window size of 2 cm^2 was designed in our group for *in-situ* measurements. The substrate (working electrode) was attached to the cell by Kapton tape (IM301202 polyimide film Goodfellow, 683-465-79). After electrodeposition, the CoCat samples were operated in Co-free or 20 µmolL^{-1} Co^{2+}-containing KP_i buffer (Co-KP_i) at 1.3 V vs. NHE for 24 hours. These "conditioning" steps were done without exposure of the sample to X-rays, but already performed in an electrochemical cell, specially designed for *in-situ* XAS.

4.1.5 X-ray absorption spectroscopy

X-ray absorption spectroscopy was used for the assessment of structural changes at the atomic level. Two types of measurements were conducted: (a) cryo measurements at 20 K and (b) *in situ* experiments at 293 K.

(a) cryo measurements at 20 K

XAS measurements (EXAFS, XANES) at the cobalt K-edge were performed at the KMC-3 beamline at the BESSY II synchrotron facility (Helmholtz-Zentrum Berlin, Germany) at 20 K in a liquid-helium cooled cryostat (Oxford-Danfysik). The excitation energy was selected by a Si-111 double-crystal monochromator (scan range 7600-8750 eV). The angle between the CoCat surface and the incident beam was approximately 45° (fluorescence mode). Fluorescence-detected X-ray absorption spectra at the cobalt K-edge were collected using a 13 Ge element detector (Ultra-LEGe detectors, Canberra GmbH) installed perpendicular to the X-ray beam. Samples were deposited on ITO/glass, therefore simultaneous energy calibration was not possible. Energy calibration was done by measuring the spectrum a cobalt foil (5 µm, 99.99% purity, Goodfellow) after 3 measured sample spectra.

(b) in-situ measurement at 293 K

The setup for *in-situ* measurement was different from cryo measurements so we did some modifications. Figure 4.2 shows the *in-situ* set up in KMC-3. Because the X-ray beam cannot pass through the single-compartment cell, there is not any detector or ion chamber after the sample and only fluorescence mode measurement is possible. Therefore, we measured only the ionization chamber (I_0) before the sample. Before and after every measurement a thick nickel metal foil (10 µm) was measured as an energy standard. To carry out the *in-situ* XAS measurements while electrochemistry is performed, a special kind of electrochemical cell was designed in our group. The cell is made of Teflon to avoid metal contamination. *In situ* measurements were performed in a one compartment PTFE cell with a quadratic window size of 2 cm^2 where a working electrode substrate transparent to X-rays (like Mylar or glassy carbon) so the X-ray beam can pass through the backside of the substrate and reaches to the sample.

For *in-situ* investigations, the electrochemical cell was driven by an SP-200 potentiostat (Bio-Logic, Claix, France). The electrolyte was not stirred during the X-ray measurements to avoid an increase in noise of the fluorescence signal. A scintillation detector was placed instead of the Ge detector close (~ 1 cm) to the electrode surface. Measurements were conducted at 293 K and the cobalt K-edge fluorescence was monitored perpendicular to the incident beam by a scintillation detector coupled to a photomultiplier. The detector was shielded by a thick iron foil (10 µm Fe, ≥ 99.99 %, Goodfellow, Bad Nauheim, GE)) against scattered X-rays and visible light. X-ray photons converted to visible light (~50 % efficiency), which was detected by a fast photomultiplier operated at 0.9 kV. The detector signal from the photomultiplier passed through a 1 MΩ resistor for current-to-voltage conversion and was read by an amplifier (Stanford Research Systems, model SR560) with was channeled through a 10 Hz low-pass filter and recorded with a time resolution of 10 ms by the potentiostat (Biologic SP-300) that also operated the electrochemical cell. For details of the setup see (González-Flores, Klingan et al. 2018).

4.1.6 XAS data extraction

For evaluation of XAS data, we need to record several data. A picture of the XAS setup is shown in Figure 4.1. The following data is simultaneously recorded: four ionization chambers (I_{00} after the monochromator and before the focal point of the beamline, I_0 before the sample, I_1 after the sample, and I_2 after the energy standard chamber), the total incoming count rates (ICR) and the raw fluorescence signal corresponds to a selected window at the Kα emission corresponding to the specific metal recorded by the 13 detector elements.

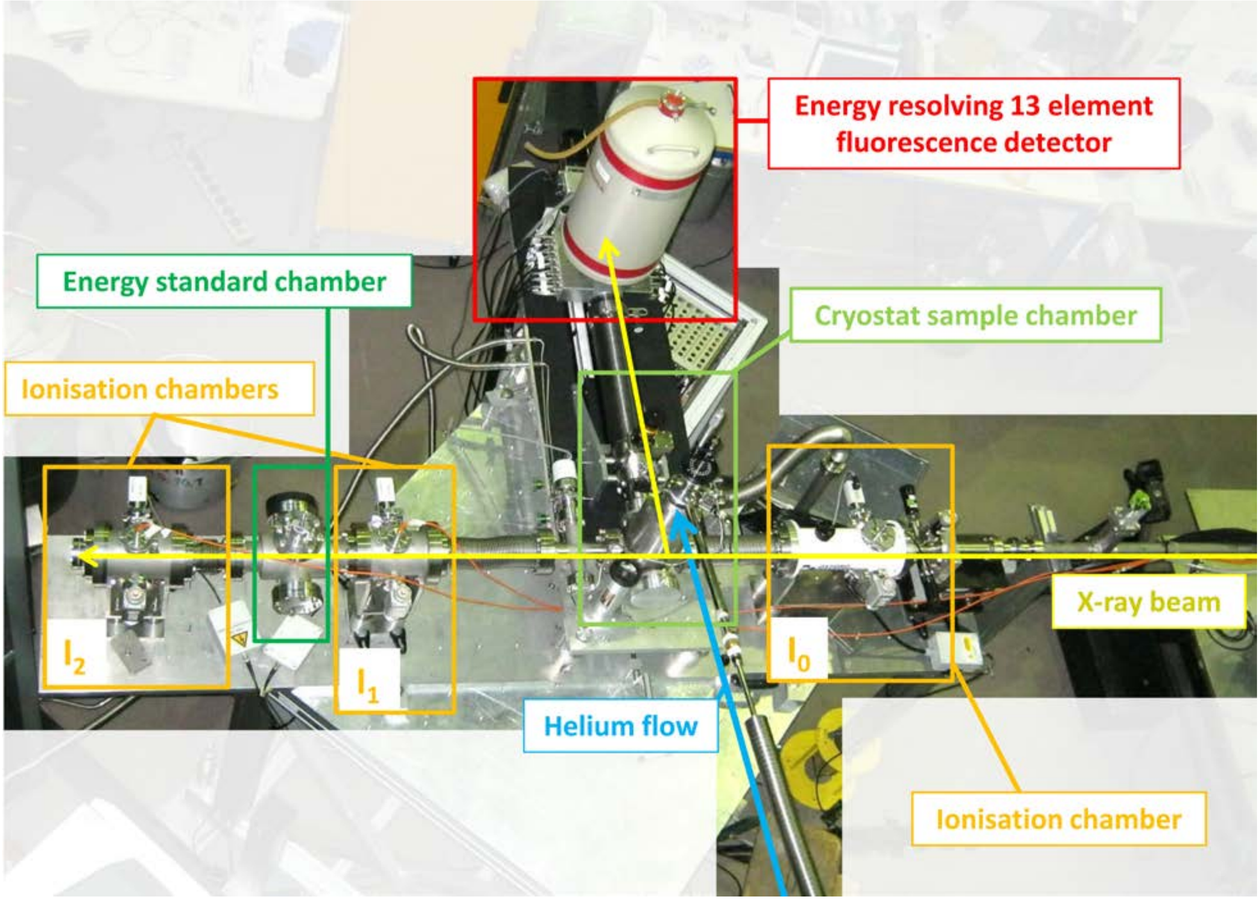

Figure 4.1. Cryo setup. 13 Fluorescence-detected X-ray absorption spectra simultaneously at the cobalt and nickel K-edge were collected using a 13 germanium elements detector (Ultra-LEGe detectors, Canberra GmbH). In addition the currents of three ionization chambers I_0, I_1, and I_2 (absorption mode) were recorded. This Figure was taken from the dissertation of Katharina Klingan.

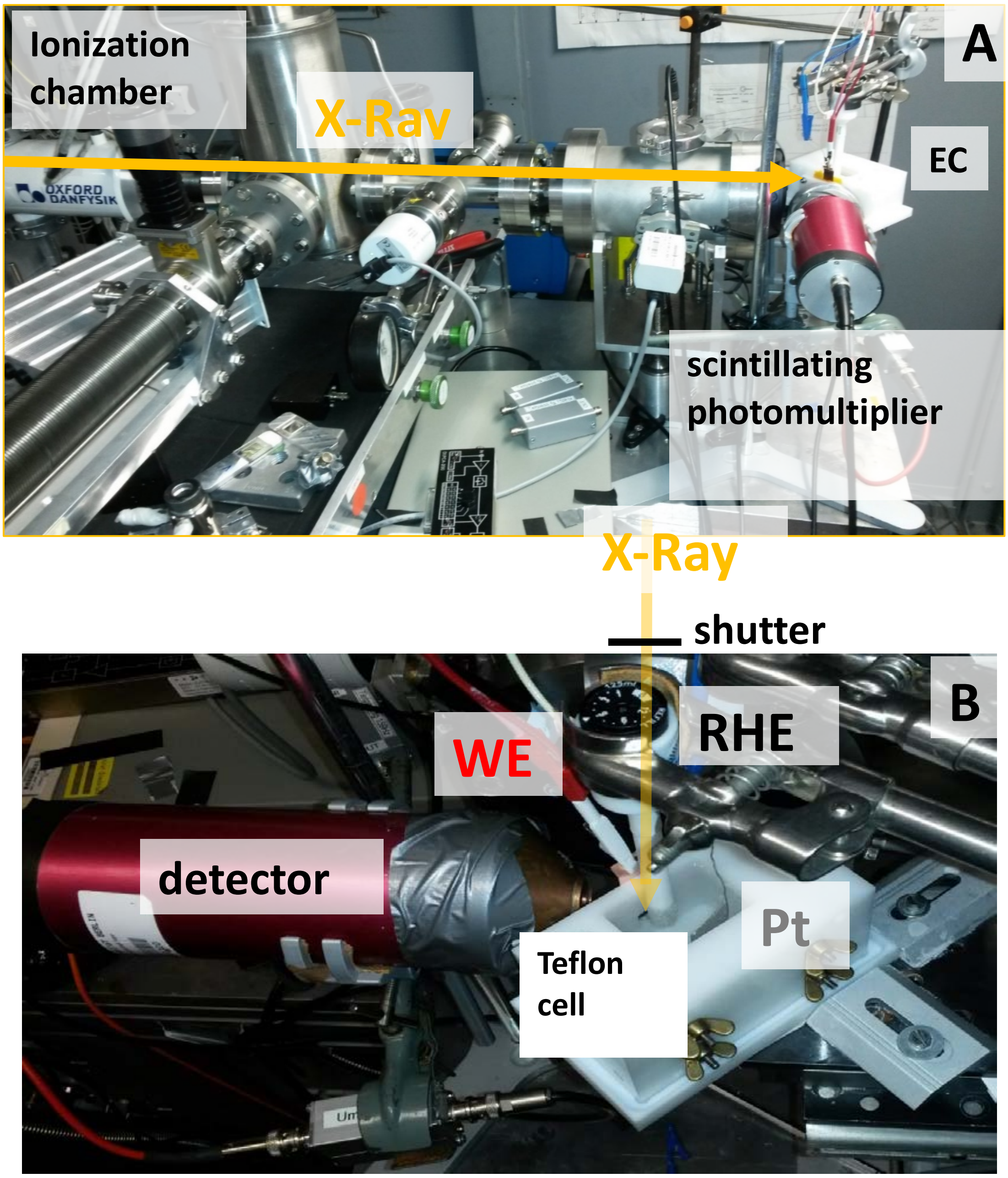

Figure 4.2-A. Picture of the set-up used for the *in-sit*u measurements. The yellow arrow indicates the direction of the incoming X-ray. The X-ray beam passes through the ion chambers and reaches the back-side of the sample. A beam shutter is placed before the sample.

Figure 4.2-B. Shows the focused part of the home-made Teflon electrochemical cell used during the *in-situ* measurements. The scintillation detector (19.6 cm^2 active area, 51BMI/2E1-YAP-Neg, Scionix) shielded by an additional 2 µm Al filter against visible light. The detector is equipped with 0.01 mm Fe for Co edge to suppress scattered light (not visible in the picture). The amplified signal is recorded by a BioLogics potentiostat that operates the electrochemical cell and records the signal from the ionization chamber. This picture was taken by Katharina Klingan.

For measuring a powder sample with absorption of about 90 %, the absorbance data should be analyzed. However, the fluorescence mode is used once the absorption is below 10 %.

An in-house software (Bessy) developed by Dr. Petko Chernev (AG Dau) was used for data treatment.

To obtain energy calibrated, normalized, and averaged fluorescence spectrum of one sample, several steps have to be followed:

(a) All signals should be corrected for the number of not-detected photons due to possible dead time of the detector elements because energy resolving detectors count and analyze the photons at the same time, therefore sometimes can fail to count. The fluorescence out-coming data (*OCR*) is correct by an exponential fit from the *ICR* values (Equation 4.1).

$$OCR = A(1 - e^{-k.ICR}) \qquad (4.1)$$

(b) Remove some glitches if it is needed.

(c) To apply the absorption effect, the intensity of the ionization change after the sample is converted to absorbance by $A_1 = -Ln(I_1/I_0)$.

Behind the sample there an energy standard is placed for energy calibration. The absorption for the standard is calculated as $A_2 = -Ln(I_2/I_1)$. Furthermore, the fluorescence data were normalized by dividing by I_0.

(d) In order to obtain meaningful spectra energies, the energy axis has to be calibrated by standard samples of known energy. Energy calibration of the data was performed by calculating the first derivative of the absorption spectra of A2. The first peak of the derivative is fitted with the combination of a Gaussian and Polynomial function and shifted to the literature value of the corresponding edge. All the experimental data is then shifted by the same factor.

(e) The data of 13 elements were averaged and background subtracted in the regions before the rising edge.Then the spectra were normalized to 1 by dividing through a linear function of a polynomial function of 2nd or 3rd order. After that, the data of several spots (3 - 6 points) are averaged and weighted by its signal to noise ratio. The signal-to-noise ratio was estimated by fitting a straight line to the data points at the end of the EXAFS region, where EXAFS oscillations are insignificantly small; and the root of the squared differences between line and data points was calculated (rms noise).

(f) After normalization, the edge position could be estimated from the spectrum by using a step integral function (Haumann, Porthun et al. 2003).

(g) The normalized EXAFS spectra were converted from energy to wave vector (k-space) and weighted by k^3. The data were then Fourier transformed from k space to R space, resulting in the radial structure functions (RSFs). The RSFs are uncorrected for the photoelectron phase shifts; thus distances are about 0.3 - 0.4 Å shorter than actual distances between the absorber and backscattering atoms.

4.1.7 Converting fluorescence data to oxidation state – jump potential

To provide evidence for changes in the redox kinetics of the CoCat, time-resolved experiments were conducted. As Figure 4.7-A shows, the recorded X-ray fluorescence signal reflects the oxidation state. To trace how fast the oxidation state changes occur, X-ray fluorescence jump potentials from 1.3 V to 0.7 V vs. NHE were recorded at fixed energy, such that this energy is approximately in the middle of the absorption edge of the CoCat (~7722 eV). Beside this, chronoamperometric data was simultaneously recorded with edge scans (XANES) of CoCat operated at 1.3 V vs. NHE was recorded because we need this data to convert the fluorescence jump potentials to oxidation state.

(a) The edge position was extracted as mentioned in section 4.3.6. Furthermore, to determine the accurate oxidation state, the pre-edge was aligned to Co oxides which have known oxidation state(Risch, Ringleb et al. 2015).

(b) The fluorescence of data (after division by I_0, but NO energy calibration, background subtraction or normalization) was analyzed. The curve of energy vs. fluorescence was plotted and the slope (S), as well as the intercept (I), determined.

(c) Then the fluorescence data was converted to edge position energy based on the following equation:

$$E = -(F*S + I - E_m) + E_p \tag{4.2}$$

Where:

F: the fluorescence data; S: slope; I: intercept;

E_m: measured energy (before energy calibration);

E_p: actual edge position (after energy calibration and normalization)

4.1.8 EXAFS simulations

Simulations were performed using the in-house software package ‘SimX’ (Dittmer 1999) and ‘SimXLite’ (developed by Dr. Petko Chernev).

An EXAFS spectrum $\chi(k)$ is given by the sum of the contributions of n_{shell} ‘atomic shells’. A ‘shell’ is a group of elements with identical atomic number and similar distances from the X-ray absorbing atom (e.g., six oxygen atoms surrounding the absorbing cobalt ion in the CoCat). The EXAFS equation is mathematically defined by the following equation:

$$\chi(k) = S_o{}^2 \sum_{i}^{n_{shell}} A(R_i, k)_i N_i \exp\left(-2\sigma_i{}^2 k^2\right) \sin(2kR_i + \phi_i)$$

where $S_o{}^2$ is the amplitude reduction factor, $A(R_i, k)_i$ is a factor that includes the scattering amplitude and mean-free-path of the photo-electron, ϕ_i the phase correction, N_i the number of atoms in the i^{th} atomic shell, σ_i the Debye-Waller parameter of the i^{th} atomic shell, and R_i the (average) distance between the X-ray absorbing atom and the atoms of the i^{th} atomic shell. The functions A and ϕ were obtained herein from ab-initio calculations using Feff 9.05 (Ankudinov, Ravel et al. 1998, Rehr, Kas et al. 2009), using coordinates from a fragment of the $LiCoO_2$ structure (layered CoO_2) with 10 cobalt atoms and 32 oxygen atoms (i.e. 5 incomplete $Co_3(\mu\text{-}O)_6$ cubanes). More details can be found in: (Risch, Ringleb et al. 2015). The coordination numbers N and Debye-Waller parameters σ are also coupled and need to be separated from each other. For conversion of the energy axis to a k-vector axis, an E_0 of 7710 eV was used. Curve-fitting of the data was accomplished within a k-range of 3 $Å^{-1}$ to 13.5 $Å^{-1}$. The amplitude reduction factor,$S_o{}^2$, was set to 0.7. The simulation results are shown in Figure 4.6 and Table 4.1.

4.2 Results and Discussions

4.2.1 XAS results

Figure 3.8 showed that the buffer has a negligible influence on the catalytic performance. At the same time, it was shown that more and more cobalt is accumulated on the electrodes (Co-containing buffers), while a stable catalytic current was achieved for operation in 20 µmolL^{-1} Co^{2+}-containing buffer. This suggested considering the turnover frequency. In this work TOF was calculated per redox active Co atom and O_2 molecule. The catalytic current was measured after equilibration for two minutes at the indicated electrode during the chronoamperometric scan. Figure 4.3 shows the TOF of the CoCat operated at 1.3 V vs. NHE in three different buffer systems (Co-free KP$_i$, KP$_i$ + 20 µM Co^{2+}, KP$_i$ +40 µM Co^{2+}) over the course of 24 hours. The TOF goes down, even faster for 20 µM Co^{2+} and 20 µM Co^{2+}.

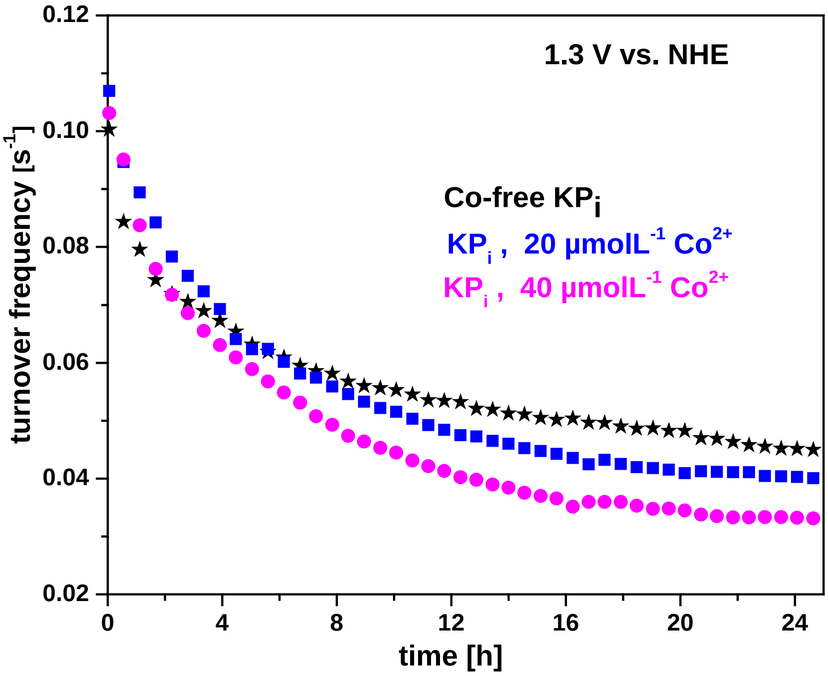

Figure 4.3. Turnover frequency (TOF) of CoCat films per redox-active site and O_2 molecule**.** Samples were operated at 1.3 V vs. NHE for 24 hours in Co-free and 20 µM as well as 40 µM Co-containing buffer. The redox charge was calculated by integration of the reductive current of each CV (0.65 – 1.40 V vs. NHE) which was measured every 30 minutes (48 CVs). The catalytic current was measured after two minutes equilibration during the chronoamperometric scan. This ratio might be named as a turnover frequency (TOF, the rate of catalytic electron flow per redox-active cobalt ion).

We aim to relate the observed changes in the TOF to structural changes in the catalyst. Three samples were selected for XAS studies; Operated samples at 1.3 V vs. NHE in phosphate buffer (KP_i, 0.1 M, pH=7) for 15 minutes (a), 24 hours in Co-free (b) and 24 hours in 20 µM Co-containing (c). Samples have been rapidly frozen by immersion in liquid nitrogen.
The X-ray absorption near-edge spectra (XANES, Fig. 4.5-A) of the three samples were very similar, with the 24 hours operated samples in Co-free and Co-containing samples practically indistinguishable and 15 minutes operated sample only slightly different (0.2 eV lower than others). The Co oxidation states in the samples, determined from the positions of the Co K-edges of Co compounds with known oxidation state (Risch, Ringleb et al. 2015) correspond to $Co^{+3.1}$. Figure 4.4-B shows the difference spectra of samples operated for 15 minutes (Co-free; KPi) and 24 hours (Co-free KPi and 20 µM Co-containing buffer). At energies close to 7724 the negative difference of graph reflects oxidation state changes.

The Fourier transform (Figure 4.5) of both EXAFS-spectra (Co-free and Co-containing buffer) operated for 24 h at 1.3 V show a higher Co-Co peak (at reduced distance 2.5 Å, peak b) that corresponds to di-µ-oxo-bridged Co atoms. This peak can be simulated by two Co-Co shells at 2.81 Å and 2.93 Å. In the short-time operated sample (15 minutes) these two shells have comparable coordination numbers, but after 24 h operation the 2.81 Å distance becomes clearly dominant (Table 4.1). Furthermore, two more peaks in the Fourier transform appear: a Co-Co-Co peak at a reduced distance of 4.5 Å (the tilted double distance of the di-µ-oxo bridge; c) and a peak related to a Co-Co-Co chain in a straight line at reduced distance 5.3 Å (the double distance of the di-µ-oxo bridge; d); both peaks are typical for layers of di-µ-oxo-bridged Co-octahedra. Another peak at a reduced distance of 3.1 Å appears after operation and might be attributed to a second oxygen shell (expected to be found at this distance in an (ordered) structure of layers of di-µ-oxo-bridged Co octahedra), or to mono-µ-oxo-bridging of Co atoms (Risch, Klingan et al. 2012). The amplitudes of all Co-Co peaks is increasing for a long-time operated samples and the increase is slightly above the noise level. It suggests that the ordering in the catalyst is enhanced or growing Co-oxide fragments are forming. Assuming a relatively slow charge transport (e.g. from OH^- to Co-ions) in larger Co-O-fragments, this could explain the lower turnover frequency and thus the dropping in catalytic activity.

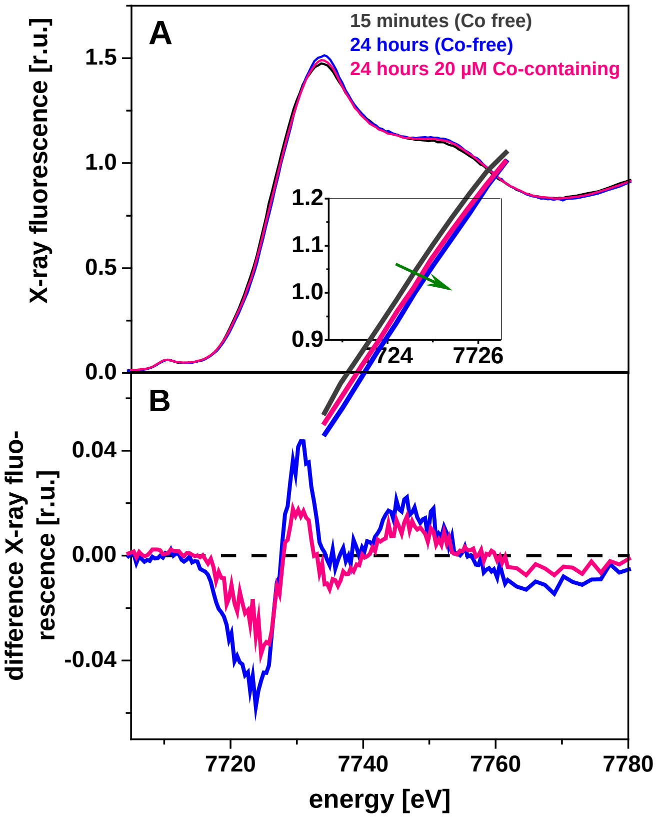

Figure 4.4. XANES spectra **(A)** and difference spectra **(B)** of CoCats operated at V = 1.3 V vs. NHE for 15 minutes (Co-free KPi), 24 hours (Co-free KPi) and 24 hours (20 µM Co-containing buffer). At energies close to 7724 the graph reflects the changes in oxidation state (negative difference).

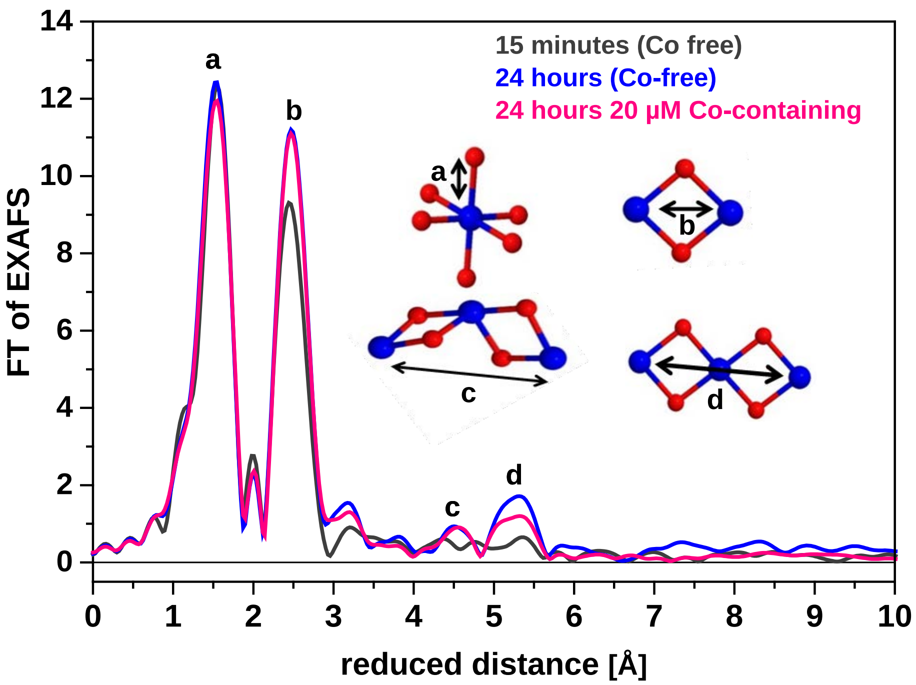

Figure 4.5. Fourier-transform of EXAFS-spectra of CoCat films electrodeposited on ITO (KP_i, pH=7) and operated for **15 min** (gray), **24 h in Co-free** (blue) and **24 h in 20 μM Co-containing** (pink) KPi at 1.3 V vs. NHE. The inset illustrates structural motifs present in the CoCat (blue – cobalt, red - oxygen). Initially, the structure is comprised of small or disordered fragments of di-μ-oxo-bridged CoO_6-octahedra with the main Co-Co distance of 2.81 Å. The operated samples (24 h) exhibit additional motifs similar to those present in either extended or well-ordered structures composed of octahedral coordinated Co-atoms. Additionally, a distance of 3.36 Å can be attributed to a Co-Co distance known from mono-μ-oxo-bridged Co-atoms or to the second oxygen shell being in line with an increased molecular fragments size of Co-oxide fragments and a higher degree of order.

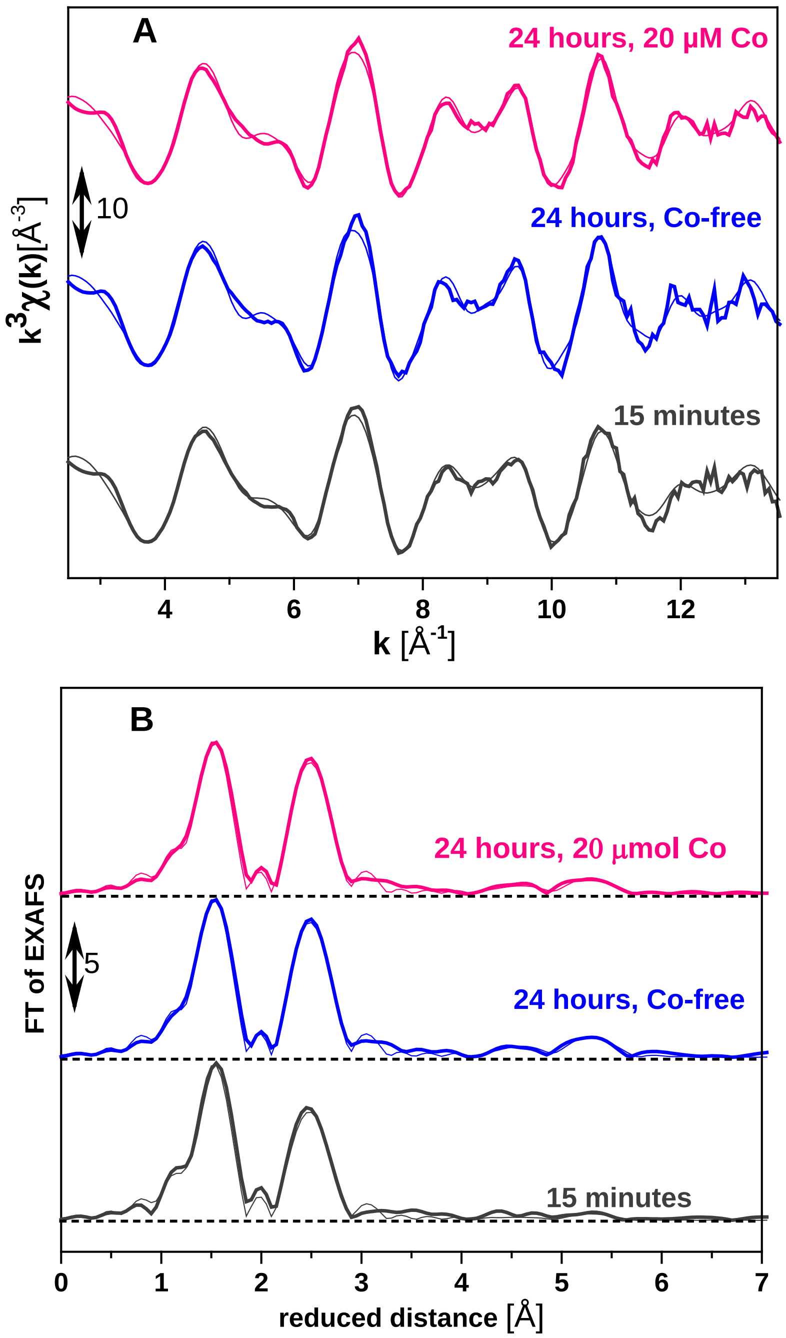

Figure 4.6. k^3-weighted $\chi(k)$ **(A)** and Fourier-transform of EXAFS spectra **(B)** of the CoCat film operated at 1.3 V vs. NHE (phosphate buffer at pH 7) for various times of operation and in the absence or presence of Co^{2+} in solution. Experimental (thick lines) and simulation results (thin lines) are shown. The fit parameters are given in Table 4.1.

Table 4.1.

Parameters obtained by simulation of the k^3-weighted EXAFS spectra. The simulated spectra correspond to the Fourier-transformed EXAFS spectra shown in Figure 4.6. (N: coordination number; R: absorber-backscatter distance; σ: Debye–Waller parameter). The interatomic distances, R, for each shell are shown in blue (in Å) and the coordination numbers at the respective sample are shown in green.

The errors representing 68% confidence intervals of the respective fit parameters are shown in parentheses. To avoid over-parameterization, the Debye-Waller parameter (σ) for oxygen shells and cobalt shells were set to 0.052 and 0.059 Å, respectively. The amplitude reduction factor, S_0^2, was fixed to 0.7. The parameters have star were fixed in the simulation program. Errors are provided in parentheses.

	Co-O	**Co-Co**	**Co-Co**	**Co-O**	**Co-Co**	**Co-Co-Co**	**Co-Co-Co (MS)**	**R-factor filtered**	**oxidation state**
R [Å]	1.90 (0.01)	2.81 (0.01)	2.93 (0.01)	3.38 (0.01)	4.85 (0.01)	5.60 (0.01)	5.60 (0.01)		
N, 15min	6.1 (0.2)	3.8 (0.2)	0.9 (0.2)	2.5 (1.1)	0.5*	0.5 (0.3)	0.5*	16.6	3.14
N, 24 h Co-free	6.3 (0.3)	4.7 (0.3)	1.1 (0.3)	3.9 (1.1)	1.5*	1.5*	1.5*	14.1	3.28
N, 24 h (+20µM Co^{2+})	6.1 (0.3)	4.5 (0.3)	0.9 (0.3)	3.9 (1.1)	1.2*	1.2*	1.2*	14.0	3.21

The XAS data indicate only minor changes in the structure of the CoCat for longer times of operation. The basic atomic arrangement is maintained, and but an increase in the EXAFS coordination number of the Co-Co shells is observed.

To provide evidence for changes in the redox kinetics of the CoCat, time-resolved experiments were conducted. As it was shown that the redox kinetics have a huge impact on the activity of water-oxidizing catalysts (Zaharieva, González-Flores et al. 2016), kinetics might be responsible for the drop in the TOF for the CoCat.

Because ITO on glass would absorb a major fraction of the X-rays, it was substituted by ITO-Mylar (Sigma Aldrich Chemie GmbH Munich, GER) for *in situ* measurements (25 mC/cm^2, KP$_i$, pH 7). The fluorescence signal reflects the oxidation state.

To track changes in the oxidation state the X-ray fluorescence was recorded at fixed energy, such that this energy is in the middle of the absorption edge of the CoCat (~7722 eV). As oxidation state changes are characterized by shifts in the edge position they can be monitored by the intensity of the X-ray fluorescence at this fixed energy (Figure 4.7).

The time scale of redox events was studied by jumping between reducing (0.7 V vs. NHE) and oxidizing potentials (1.3 V vs. NHE) for three minutes. To prevent a possible limitation of those processes by electrolyte resistance the experiments were conducted in 0.1 M KP_i + 1 $molL^{-1}$ KNO_3 as supporting electrolyte, as it was successfully used for electrochemical characterization of manganese oxides and nickel-borate catalysts before (Bediako, Surendranath et al. 2013, Huynh, Shi et al. 2015).

In-situ X-ray fluorescence transients were simulated with a sum of two exponentials (parallel reactions), a fast phase and a slow phase (equation 4.2, Figure 4.7).

$$F = F_0 + A_1 \exp(-t/T_1) + A_2 \exp(-t/T_2) \qquad (4.2)$$

F_0 is the offset of fluorescence. A_1 and A_2 correspond to the number of cobalt atoms that their oxidation state change in T_1 and T_2.

The observed time constants allow a comparison of the oxidation state change kinetics of different samples (Figure 4.7, table 4.2). The amplitudes A1 and A2 are proportional to the Co oxidation state change when recorded in the middle of the Co K-edge (7722 eV). This is valid since the X-ray fluorescence intensity can directly be converted to a Co-oxidation state.

According to the EXAFS-analysis, three types of samples have been investigated: the freshly prepared CoCat **(B)** (25 $mCcm^{-2}$ deposited, operated for 15 minutes), a catalyst operated for 24 hours in 20 $\mu molL^{-1}$ Co^{2+}-containing buffer **(C)** and a film three times as concentrated as film the first mentioned **(D)**.

The obtained redox processes show that after 24 hours both, reduction and oxidation, are by a factor of approximately two slower **(C)**. Note that this sample accumulated almost three times the amount of Co-oxide on the electrode (Figure 4.7). Amplitudes $A_{1,ox}$ and $A_{1,red}$ as well as $A_{2,ox}$ and $A_{2,red}$ are considered to reflect corresponding (reversible) processes as their magnitude is comparable in both films **(B)** + **(C)**.

The slower kinetics in **(C)** can be interpreted the following: (i) charge transport limitations due to growing film thickness, or (ii) deaccelerated kinetics due to the enhanced degree of order in the film of the catalyst operated for one day as suggested from the XAS data. The increase in time constants by a factor of two is not convincingly explaining the activity loss. Slower oxidation state change in this case might come from the film thickness that is higher for the operated film (+ 20 $\mu molL^{-1}$ Co^{2+}) by a factor of three approximately.

Accordingly, a film with three times the charge deposited **(D)**, yielded approximately the same amount of cobalt on the electrode that is present after 24 of operation in 20 µmolL^{-1} Co-containing buffer.

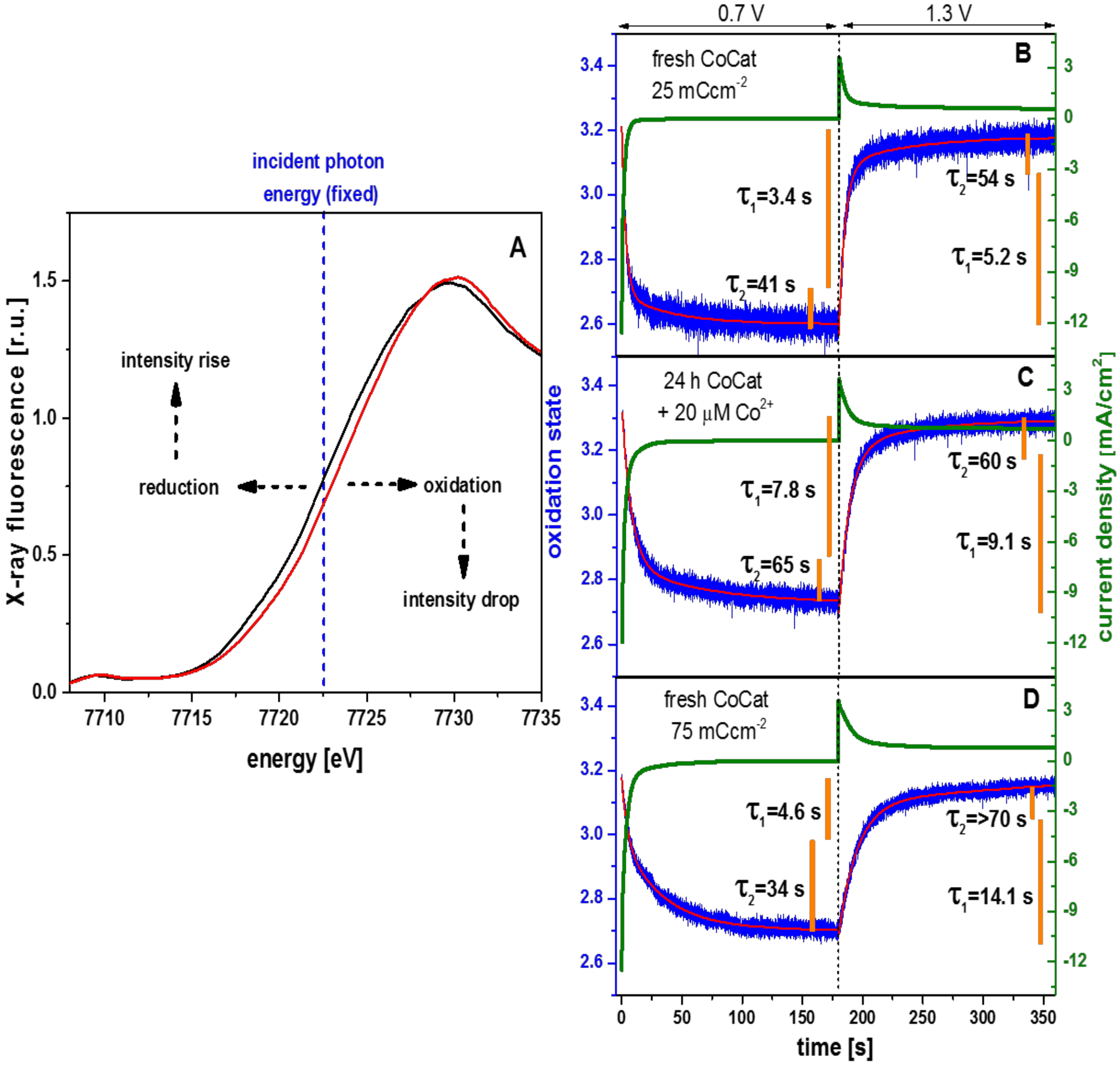

Figure 4.7. Oxidation state change kinetics. (A) Showcase XANES spectra for a CoCat sample. Redox processes typically are accompanied by a shift in edge position. Recording the emitted X-ray fluorescence intensity at fixed energy in the middle of the K-edge jump can provide insight in redox kinetics.

In-situ X-ray fluorescence transients with step potential procedure for CoCat samples deposited on Mylar 25 mC/cm^2 fresh **(B)**, 24-h operated in 20 µmolL^{-1} Co^{2+}-containing buffer **(C)**, 75 mC/cm^2 fresh **(D)**. Amplitudes A_1 and A_2 (correspond to the number of cobalt atoms that their oxidation state change in T_1 and T_2) are indicated with bars next to the time constants. The ohmic resistance was about 65 Ω.

This film exhibits slightly smaller time constants for the reduction and larger time constants for the oxidation – still being within the same order of magnitude. However, due to much smaller amplitudes and mixing of A_1 and A_2 for the film **(D),** a comparison is more sophisticated. Although the two-exponential fit is representing the data similarly well, there is no clear biphasic exponential behavior as it was observed for **(B)** and **(C)**. Nevertheless, the time constants for the film **(D)** are clearly larger than for film **(B)**, although a slightly lower $T_{1,ox}$ and slightly larger $T_{1,red}$ could result in time constants close to those of sample **(C)** with similar fit quality.

Table 4.2: Fitting parameters for redox kinetics investigated by *in situ* X-ray fluorescence at the fixed energy of 7722 eV;
Data were fitted by applying the equation: $F = F_0 + A_1 \exp(-t / T_1) + A_2 \exp(-t / T_2)$

Sample	Parameter	Co reduction	Co oxidation
25 mC/cm^2 fresh film	F_0	3.1247 ± 4 E-4	3.7042 ± 6 E-4
	A1	0.518 ± 0.002	-0.521 ± 0.002
	T_1	3.39 ± 0.03	5.19 ± 0.04
	A2	0.093 ± 0.001	-0.090 ± 0.001
	T_2	41 ± 1	54 ± 1.6
	R^2	0.91	0.95
24-h operated in 20 µmolL^{-1} Co^{2+}- containing	F_0	3.1692 ± 7 E-4	3.7367 ± 6 E-4
	A1	0.466 ± 0.002	-0.504 ± 0.002
	T_1	7.78 ± 0.05	9.08 ± 0.06
	A2	0.121 ± 0.001	-0.092 ± 0.002
	T_2	65 ± 1.6	60 ± 2
	R^2	0.97	0.98
75 mC/cm^2 fresh film	F_0	3.1443 ± 2 E-4	3.599 ± 0.001
	A1	0.185 ± 0.001	-0.382 ± 0.003
	T_1	4.59 ± 0.07	14.1 ± 0.1
	A2	0.287 ± 0.001	-0.093 ± 0.002
	T_2	34.1 ± 0.2	75 ± 3.7
	R^2	0.98	0.98

Additional in-situ XAS experiments in Co-free buffer (KP_i, pH 7) were performed. We collected XANES spectra for potential of 1.3 V vs. NHE. Before collecting XANES data, the electrochemical potential had been applied for 3 minutes to ensure steady state conditions and then XANES have been taken (4 edges for Co-free; KP_i, pH 7) for about 25 minutes.

Furthermore, for studying film dissolution *in-situ* potential jumps were performed, in which the potential was changed from 1.3 V to 0.7 V vs. NHE (each applied for 3 min). The energy was fixed in the middle of the absorption energy (7724 eV) during the potential jumps. From this data, the redox-charge of the CoCat was calculated when 0.7 V was applied. In addition, the catalytic current density was extracted from the average of last minute operation at 1.3 V vs. NHE. Schema 4.1 shows the flow chart of the *in-situ* experiment.

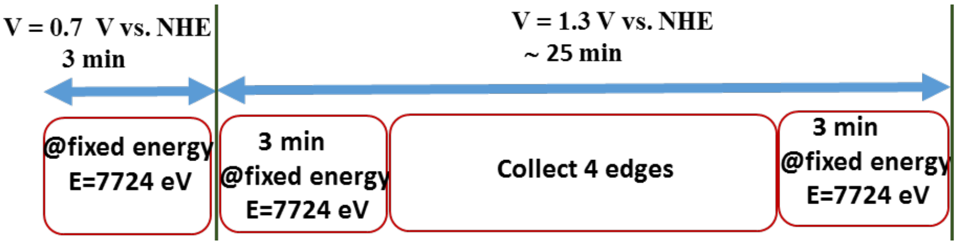

Schema 4.1. A flow chart of the *in-situ* experiment of CoCat operated in Co-free phosphate buffer to provide evidence for oxidation state changes and also to study film dissolution by recording simultaneously the fluorescence during operation.

Figure 4.8 shows the current density, redox-active cobalt ions, fluorescence amplitude after the edge and cobalt oxidation state of a sample operated in Co-free buffer for 6.5 hours. It shows that after 6.5 hours operation the amount of Co ions were dissolved rather 5 % and the fluorescence data is well compatible with redox activity. Although CoCat is almost stable in this period the current density decreased by 35 %. Figure 4.8 clearly displays the average oxidation state of cobalt is constant during operation.

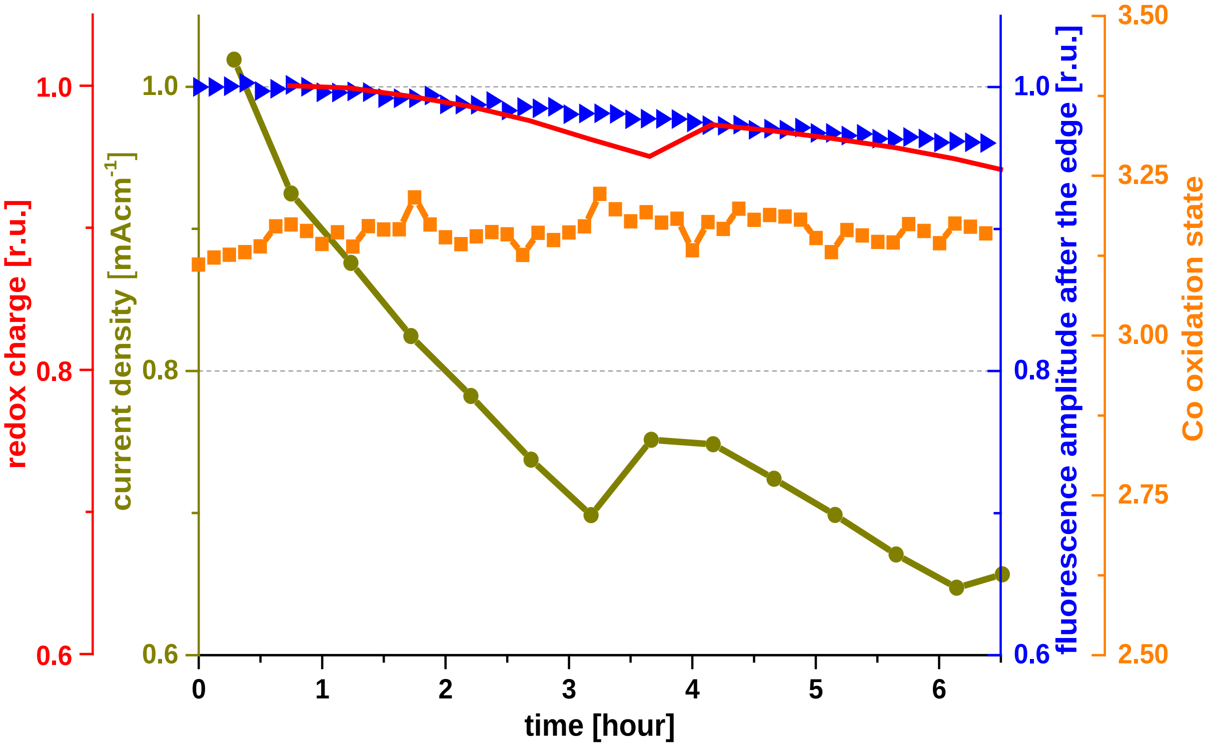

Figure 4.8. Chronoamperometric scans with simultaneously recorded edge scans (XANES) to monitor CoCat oxidation state changes and film dissolution when it is operated in **Co-free buffer** (ITO on Mylar, KP_i, pH 7). XANES (4 edges) were taken at 1.3 V vs. NHE. After that, potential jumps from 1.3 V to 0.7 V vs. NHE were performed to monitor the catalytic current and the redox-charge. The protocol was repeated for 6.5 hours. Left Y-axes, red and green, show the normalized redox-charge during the potential jumps and the averaged current during four XANES spectra, respectively. The right Y-axes, orange, shows the oxidation state of CoCat, and the fluorescence amplitude, blue, show the amplitude fluorescence after edge.

To study changes in oxidation state when CoCat is operated in 20 µM Co^{2+}-containing buffer, additional in-situ XAS experiments were performed. We collected XANES spectra at 1.3 V vs. NHE. Before collecting XANES data, the electrochemical potential had been applied for 3 minutes to ensure steady state conditions and then XANES have been taken (7 edges) for about 30 minutes.

Furthermore, for studying film dissolution, *in-situ* CV was performed. The energy was fixed in the middle of the absorption energy (7724 eV) when the CV was recorded. The redox-active cobalt ions were calculated from the negative area of CV and the catalytic current density was extracted from the maximum point of it. Schema 4.1 shows the flow chart of the *in-situ* experiment.

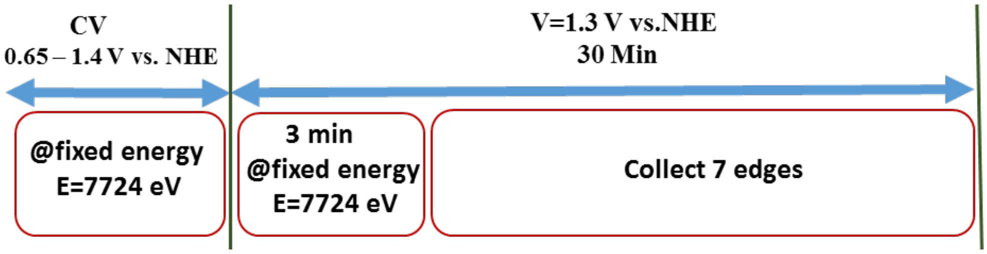

Schema 4.2. A flow chart of the *in-situ* experiment of CoCat operated in 20 µmolL^{-1} Co^{2+}-containing phosphate buffer for oxidation state changes and studying film dissolution by recording simultaneously the fluorescence during operation.

Figure 4.9 shows the current density, redox-active cobalt ions, fluorescence amplitude after the edge and cobalt oxidation state of sample operated in Co-free buffer for 8.5 hours. It shows that during operation in 20 µmolL^{-1} Co^{2+}-containing buffer the oxidation state of the CoCat remains constant over 8 hours. Furthermore, under these conditions, the fluorescence data suggests that the thickness of the film is growing by 35% but surprisingly the catalytic current density is decreasing about 10%. The fluorescence data also confirms the rising of the film thickness.

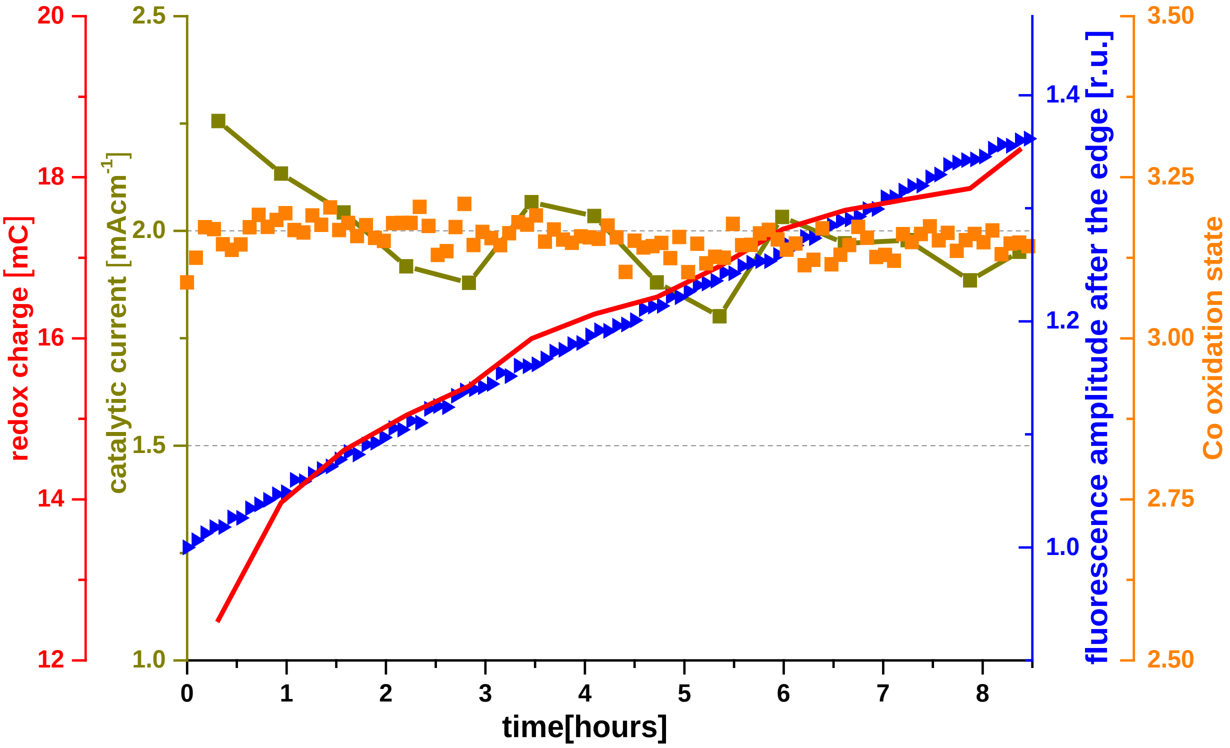

Figure 4.9. Chronoamperometric scans with simultaneously recorded edge scans (XANES) to monitor CoCat oxidation state changes and film dissolution when it is operated in **Co-containing buffer** (ITO on Mylar, KP_i, 20 µmolL^{-1} Co^{2+}, pH 7). XANES (7 edges) were taken at 1.3 V vs. NHE. After that potential jumps from 1.3 V to 0.7 V vs. NHE was performed to monitor the catalytic current and also the redox-charge. These protocol repeated for 8.5 hours. Left Y-axes, red and green, show the normalized redox-charge during the potential jumps and the averaged current during four XANES spectra, respectively. The right Y-axes, orange, shows the oxidation state of CoCat is almost constant and blue, shows the amplitude fluorescence after edge.

4.2.2 XAS study of CoCat oxidation state changes during cyclic voltammetry

To study the dynamics of the oxidation state changes during operation in Co-containing buffer (ITO on Mylar, KP_i + 20 µmolL^{-1} Co^{2+}, pH 7), *in-situ* cyclic voltammetry experiments (0.45 -1.4 V vs. NHE) with simultaneously recorded fluorescence data of CoCat were performed. The X-ray energy beam was fixed at the middle of the cobalt edge (7724 eV). Figure 4.7-A showed that the changes in the fluorescence are related to changes in the oxidation state. This relation can be used for in-situ CV experiments as well. The changes in fluorescence during the CV scan are shown in Figure 4.10. An increase in the electrochemical potential relates to a decrease in fluorescence on the forward scan of the CV, meaning that the CoCat is being more oxidized. During the backward scan, the CoCat is reduced and the fluorescence signal is gradually increased to its initial level. During the CV the oxidation sate of CoCat is changing from 2.6 to 3.2. These results are in line with the changes observed during potential jumps (Figure 4.7).

After taking a CV with simultaneously recorded fluorescence data, the X-ray beam was stopped and the CoCat was operated for 8 hours at 1.3 V in 20 µmolL^{-1} Co^{2+}-containing buffer. As was discussed in chapter 2, the thickness of the sample is growing during operation but the catalytic current remains stable. During this operation, the dynamic redox-behavior of the CoCat could change. To investigate this possibility, we repeated cyclic voltammetry with simultaneously recorded fluorescence data after operation of the CoCat at catalytic potential for 8 hours. Figure 4.10 shows that after 8 h operation the CoCat film exhibits a slower redox-behavior than its as-deposited counterpart, but the minimal (reduced form) and maximal (oxidized form) oxidation state are the same for the not-operated and the operated film. However, the slower redox-changes are small and could be rather related to the film thickness than the nature of the catalyst.

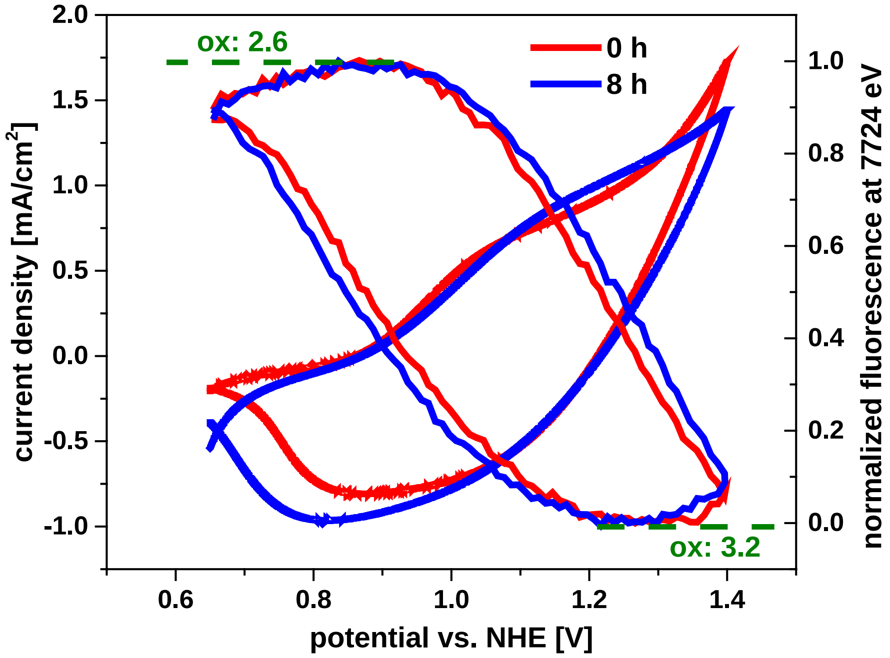

Figure 4.10. *In-situ* X-ray absorption measurements of CoCat deposited on ITO on Mylar (25 mC/cm^2). Cyclic voltammogram experiments with simultaneously recorded fluorescence data of fresh film **(red)** and after 8 hours operation at 1.3 V vs. NHE in 20 µmolL^{-1} Co^{2+}-containing phosphate buffer **(blue).** The X-ray energy was fixed at the middle of the cobalt edge (7724 eV) and the scan rate of CV was 20 mV/s. During operation (8 hours) the X-ray beam was stopped.

4.2.3 Study of oxidation state changes during cyclic voltammetry of CoCat by in-situ UV-vis

As was discussed in section 4.2.3, after 8 hours operation at 1.3 V in 20 µmolL^{-1} Co^{2+}-containing buffer the process of oxidation and reduction is a bit slower than for the as-deposited CoCat. It could be possible to resolve these changes more clearly with *in-situ* UV-vis spectroscopy. The CoCat film was operated at the same condition (ITO-glass, KPi, pH 7). *In-situ* CV-UV-vis (green light; 520-560 nm) absorption data were recorded every 4 hours to diagnose the dynamics of the oxidation state changes. To increase the ratio of signal to noise of UV-visible absorption data, CVs were collected ten times and their UV data were averaged. Figure 4.11 shows that during operation the oxidation process is getting slower. However, we did not observe any time-dependent linear changes of the CoCat redox-properties. Most changes are completed within 12 hours, the following operation of 8 hours does not affect the redo-properties of the film significantly.

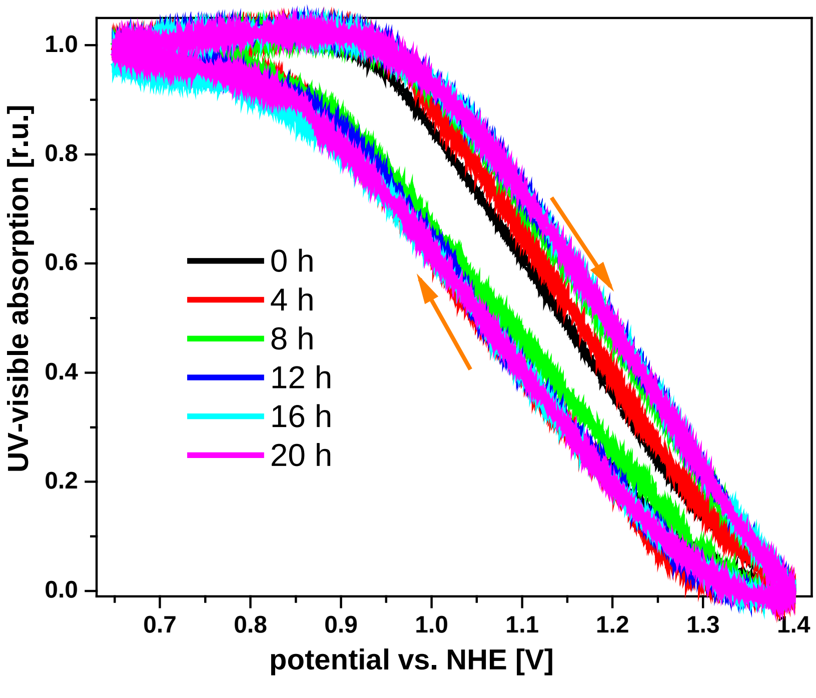

Figure 4.11. *In-situ* UV-visible (green light; 520-560 nm) absorption measurements of cobalt catalyst sample deposited on ITO on glass (10 mC/cm^2). CoCat was operated at 1.3 V vs. NHE in 20 µM Co^{2+}-containing phosphate buffer (KPi, pH7) for 20 hours, and CVs with simultaneously recorded UV-visible absorption data were recorded every 4 hours.

4.3 Summary

- Structural analysis by EXAFS spectroscopy of operated (24 hours) samples at catalytic potentials indicates small, but significant changes. They can very probably be related to an increasing order or a potentially enhanced molecular fragments size within the Co-oxide framework. An additional indication for structual changes is provided by an increasing concentration of either mono-µ-oxo-bridged Co-species or a visible splitting of the oxygen shell. Both structural motifs seem to cause a drop in the activity of the CoCat.
- Redox kinetics have been found to slow down for the reduction and oxidation of the CoCat after being operated for 24 hours. This finding can be attributed to charge transport limitations in the thicker film and a different kinetic response of the Co-oxide fragments. The changes are relatively weak and could very likely be a consequence of the growing film thickness only.
- *In-situ* XAS experiments of CoCat operated at 1.3 V in 20 µmolL^{-1} Co^{2+}-containing phosphate buffer (KPi, pH7) for 8 hours shows that the oxidation state of cobalt catalyst stays almost constant over this extended time period.

Chapter 5

Stability and self-repair of a nickel oxide catalyst (NiCat)

Recently the effects of short-term electrolysis at 1.1 V *vs*. NHE (1 M B_i) on the NiCat has been studied (Lee, Carlton et al. 2012, Farrow, Bediako et al. 2013). It was shown that activation resulted in current density values, which were two orders of magnitude enhanced compared to an ‘as-deposited’ film. Herein, we have investigated self-healing of NiCat operated at non-catalytic and catalytic electrode potentials. During the electrochemistry experiment after every 30 minutes of chronoamperometry, CVs are recorded in order to diagnose losses in redox-active nickel ions and catalytic activity.

Electrochemical results show that for operation of NiCat in Ni-free buffer at non-catalytic and catalytic potentials the redox charge drastically decreases within the first day of operation and then reaches a stable condition. However, the catalytic current reaches a minimum after only the 12 hours of operation. This means that the minimum of redox charge and the catalytic current are not consistent.

The Tafel slope of NiCat after one-week operation is lower than for the as-deposited sample.

Portions of chapters 5 and 6 have been prepared for publication:

Katharina Klingan, Mohammad Reza Mohammadi, Diego González-Flores, Petko Chernev, Ivelina Zaharieva, Paul Kubella, Stefan Loos, Chiara Pasquini, Rodney Smith, and Holger Dau

K. Klingan tested the experiments related to the ‘non-operated’ NiCat.

M. R. Mohammadi performed all experiments and the results are shown in chapters 5 and 6.

D. González-Flores, P. Chernev, I. Zaharieva, P. Kubella, S. Loos, C. Pasquini, and R. Smith assisted in synchrotron measurements and by valuable discussions.

H. Dau supervised.

5.1. Experimental Section

5.1.1 Materials

Reagents: $Ni^{II}(OH_2)_6(NO_3)_2$ (ChemPur, ≥99.9%), $Fe^{III}(OH_2)_9(NO_3)_3$ (Sigma Aldrich, ≥98%), H_3BO_3 (Merck, p.A.), NaOH(Roth, ≥99%).

All reagents were used without further purification. Solutions were prepared with 18.2 MΩ·cm Milli-Q water.

5.1.2 Electrodeposition of NiCat

Electrochemical experiments including the deposition of the nickel oxide film (NiCat) were performed in a single-compartment cell (Titration vessel, Borosilicate glass 3.3 according to ISO 3585, Metrohm), three-electrode setup driven by ten parallel Gamry potentiostats (Gamry Interface 1000^{TM}, Warminster, USA). A platinum mesh (25×25 mm^2) served as a counter electrode and an Ag/AgCl-electrode (+200 mV vs. NHE, Metrohm) as a reference electrode. The working electrode was ITO coated on glass (12 Ω per square, VisionTek Systems Ltd, Cheshire, UK). Copper tape (Farnell GmbH) was attached to the ITO on glass substrate to upgrade the electrical contact between the ITO and the clamp.

Before anodic deposition, the substrate and the platinum grid were cleaned with ethanol, concentrated nitric acid and sufficient amounts of MiliQ water. After electrodeposition, the single-compartment cell and the platinum grid (100 mesh, 99.9 %, Sigma Aldrich GmbH) were rinsed with nitric acid and MiliQ water, while the reference electrode was rinsed with MiliQ water. The NiCat was anodically electrodeposited using 0.1 M $B(OH)_3$ (Bi) and 0.5 mM $Ni(NO_3)_2$ at pH 9.2 and a deposition potential of 1.15 V vs. NHE. The buffer solution of 0.1 M $B(OH)_3$ was adjusted to pH 9.2 with small amounts of a saturated NaOH solution. The deposition was stopped at a charge of 10 mC cm^{-2}. Active IR-drop compensation was not possible to conduct with this potentiostat and resistances were about 90 Ω for deposition and operation.

5.1.3 Electrochemical Characterization

5.1.3.1 Ni-free borate buffer

The NiCats were operated in Ni-free buffer (Bi: 0.1 M H_3BO_3, pH 9.2) at 10 different catalytic and non-catalytic potentials (0.80, 0.90, 1.00, 1.10, 1.15, 1.20, 1.25, 1.30, 1.35, 1.40 V vs. NHE) for one week. Cyclic voltammograms (0.45 – 1.45 V vs. NHE, the scan rate of 20 mV s^{-1}) were run every 30 minutes in order to diagnose losses in redox-active nickel ions and catalytic activity (Figure 5.1). The second of two scans is analyzed and the current density corresponding to 1.45 V vs. NHE was selected as a catalytic current. The uncompensated resistance (R_u) was about 100 Ω.

5.1.3.2 Ni-containing borate buffer

The NiCats were operated in Ni-containing buffer (Ni-Bi: 3, 5, 10, 20 µM) at 1.15, 1.3, 1.4 V vs. NHE for one week. As was mentioned in section 5.1.3.1, cyclic voltammograms were recorded every half hour in order to diagnose losses in redox-active nickel ions and catalytic activity (Figures 5.1 & 5.3).

5.1.3.3 Evaluation of deposited material by TXRF

Chemical analysis was conducted using a total reflection X-ray fluorescence (TXRF) instrument to determine the numerical value of the amount of deposited Ni in NiCats. The details of this technique were explained in section 2.1.4.

5.2 Results and Discussion

5.2.1 Stability of NiCat in Ni-free buffer

Recently the effects of short-term electrolysis at 1.1 V *vs.* NHE (or 3.5 mA cm^{-2} for 2.5 hours in 1 M B_i) on the NiCat were studied (Dincă, Surendranath et al. 2010, Bediako, Costentin et al. 2013). It was shown that activation resulted in current density values, which were two orders of magnitude enhanced compared to an 'as-deposited' film. In this work, we have investigated the long-term electrolysis (one week) of the NiCat operated at different electrochemical potentials (0.80 - 1.40 V vs. NHE). During the electrochemistry experiment after every 30 minutes of chronoamperometry, CVs are recorded in order to diagnose losses in redox-active nickel ions and catalytic activity. The second of two scans with a scan rate of 20 mV s^{-1} is analyzed. The data were normalized to the initial CVs.

Figure 5.1-A shows the amount of redox-active nickel ions dramatically decreased within the initial half-day operation. The dissolving of nickel atoms continue within two days operation but with a slower rate. After two days of operation the rate of dissolution and reassembling is the same for potentials lower than 1.25 V vs. NHE. However, for higher potentials the rate of assembling is higher than dissolution, meaning that the number of redox-active nickel ions is increasing gradually for some time and after 5 days operation stays almost constant. After one week operation at non-catalytic potentials (≤ 1 V) only 20 % of the as-deposited nickel atoms remain. On the other hand, more than 50 % of redox activity remains for those one operated at higher than 1.2 V but lower than 1.4 V.

Figure 5.1-B shows that after 11 hours of operation at redox potentials (0.80 and 0.90 V vs. NHE) and 17 hours of operation at catalytic potentials (1.40 V vs. NHE) the catalytic currents reach a minimum. In addition, although the amount of redox-active Ni ions is significantly decreased (Figure 5.1-A) the catalytic activity increases significantly for prolonged electrolysis (Figure 5.1-B).

What is really surprising is the behavior at 0.80 and 0.90 V; a lot of redox activity is lost (80 %), but the catalytic current density is increased by about 50%, meaning that they have more active nickel center than initially.

Every 24 hours of operation, chronoamperometric data sets (potential jumps to obtain corresponding Tafel slopes) were recorded. The small drop in catalytic current after every 24 hours could be related to the interruption of the application of constant potentials by the potential jumps. It is evident from Figure 5.1 that the catalytic current and the redox activity follow each other only within the first half-day operation. However, after that the redox activity is not increase gradually while the catalytic current continuously increased.

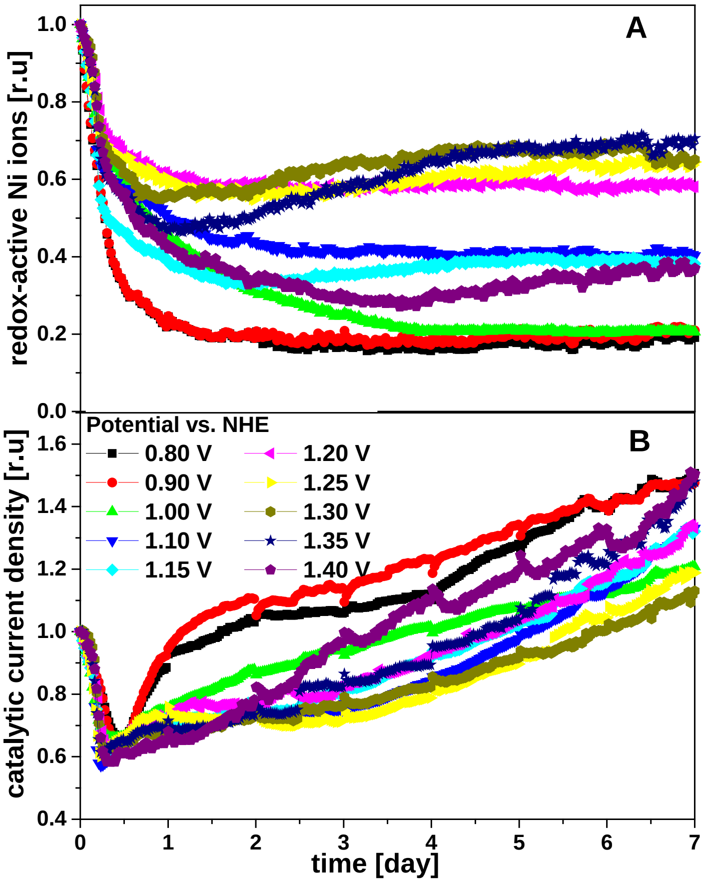

Figure 5.1. Water oxidizing nickel-oxide film operated in 0.1 M $KB(OH)_3$ at pH 9.2. The amount of redox-active Ni ions **(A)** and the catalytic current density **(B)** determined by integration of negative cathodic CV scan during operation of nickel-oxide films at indicated potentials (0.80 - 1.40 V vs NHE) over the course of one week. Every 30 minutes of chronoamperometry CVs (0.45 – 1.45 V vs. NHE) are recorded and the second of two scans with a scan rate of 20 mV s^{-1} was analyzed. The current density corresponds to 1.45 V vs. NHE was selected as a catalytic current and the data were normalized to the initial CVs. Every 24 hours, Tafel data was recorded. The mean value of the redox-charge and the catalytic current density of the initial CV of all samples were about 7 mC/cm^2 and 1.5 mA/cm^2, respectively.

To determine the accurate amount of nickel atoms and compare it with the redox-charge of CV, TXRF was performed. Figure 5.2 reveals that the absolute amount of nickel present is not exactly following the trend of the redox activity for all applied potentials. However, similar values for the amount of nickel atoms (n_{Ni}) and redox charge are obtained for non-catalytic potentials (≤ 1.10 V vs. NHE). Between 1.15 and 1.30 V the amount of nickel present in the films is not following the trend of the redox activity, which means that from 1.15 V to 1.30 V the redox-charge increased while n_{Ni} decreased. At high catalytic potentials (1.4 V) the loss in nickel atoms is about 60%, and n_{Ni} and the redox charge behave similarly.

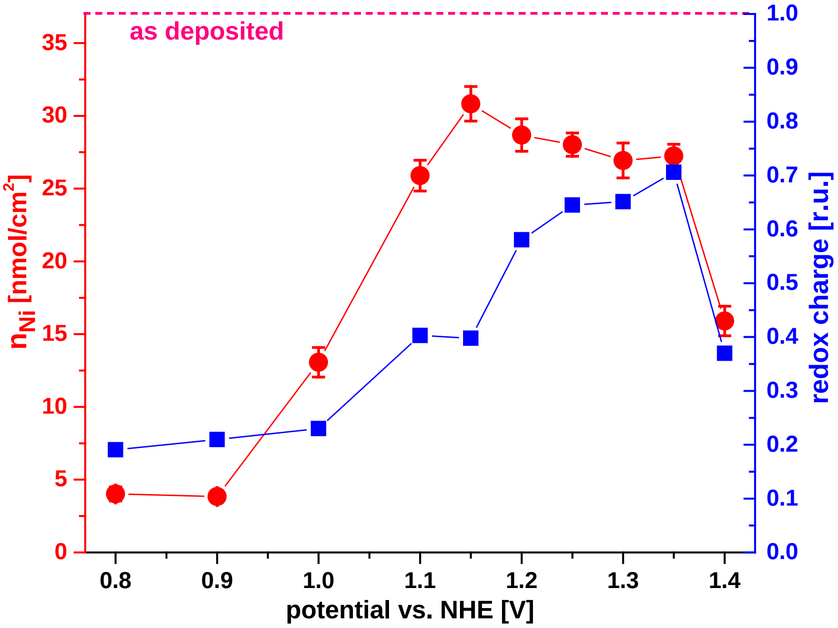

Figure 5.2. Amount of nickel extracted by chemical analyses of catalysts operated for one week in Ni-free buffer (0.1 M $KB(OH)_3$ at pH 9.2, red) and the redox-charge normalized to the initial CV (blue). The initial amount of Ni atoms was 37 nmol/cm^2. The transferred redox-charge during the cathodic scan of the first CV was approximately 7 mC/cm^2. Lines added to the Figures serve to guide the eye.

5.2.2 Self-healing of NiCat in Ni-containing buffer

When nickel catalysts are operated in Ni-free buffer (< 1.15 V vs. NHE) less than half of their initial redox-activity after one week of operation, but the catalytic current density is higher than in the beginning. However, the behavior of cobalt catalyst (CoCat) is quite different to NiCat. As was already discussed in chapter 2, the consequence of dissolving CoCat ions into the buffer during long time operation is reducing the catalytic activity. The behavior of CoCat in cobalt-containing buffer was already studied (chapter 3) and it was shown that during operation the catalytic current increased with loading cobalt ions. Now it is interesting to monitor the catalytic current of NiCat when it is operated in Ni-containing buffer.

For further analysis of the self-healing, NiCats were operated at catalytic and non-catalytic electrode potentials in different concentrations of Ni-containing buffers (3, 5, 10 and 20 µmolL^{-1}) and cyclic voltammograms were run every half an hour in order to diagnose losses in redox-activity or in the active sites. The same protocol was applied to CoCat, the additional Ni^{2+} could potentially compensate loss of nickel atoms - if re-deposition takes place and leads to catalytically active sites (self-healing process). Figure 5.3 illustrates the number of redox-active nickel ions and the catalytic current at non-catalytic and catalytic electrode potentials.

Figure 5.3 shows that during initial operation hours the redox-charge and also the catalytic current decrease and then both are rising. The redox charge is increased to reach a maximum of and after this “saturation the catalyst dissolves either into the buffer or the rate of dissolution and reassembling are the same.

When NiCat operated at non-catalytic potential (1.15 V vs. NHE) after decreasing within initial operation hours, the redox-charge and also the catalytic current gradually increase (except a drop after about one to two days of operation in the catalytic current density) to reach the saturation amount after 6 days and then the catalytic current decreased. The decrease of the catalytic current after about 6 days operation may be related to charge transfer limitation.

When Ni-Cat is operated at catalytic potentials (≥ 1.30 V vs. NHE) after a drastic loss in the catalytic current, it is increased sharply for several hours. The redox-charge is also risen after initial drops. Then the amount of redox-active Ni ions increased gradually for about four days. However, the catalytic current decrease until about two days and the increase to reach the maximum amount and then start to drop with decreasing the amount of redox-charge.

Operation of the NiCat in Ni-containing buffer causes the amount of nickel to increase by a factor of about three (Figure 5.3-A), but the catalytic current is almost the same as the initial value or lower (Figure 5.3-B). However, when the NiCat is operated in Ni-free buffer the redox charge decreases about 40% while the catalytic current increases more than 20%. Therefore, the self-assembling process of the NiCat is not totally self-repair mechanism because the number of active nickel sites is decreased. Furthermore, when the thickness of the sample increases maximally during 4 days of operation (Figure 5.3-A), we observe a charge transfer limitation which causes the catalytic current to decrease.

After one week of operation in Ni-free borate buffer, the catalytic current (Figure 5.1-B) is higher than the initial amount while at least 30% of Ni atoms are dissolved (Figure 5.1-A). This could be related to changes of the number of Ni active sites. However, when NiCat is operated in Ni-containing borate buffer the amount of redox-active Ni ions is increased two times but the catalytic current is lower than operated samples in Ni-free buffer, meaning that the number of active sites is decreased or could be related to mass transport limitations.

It could be beneficial to compensate the losses activity of Ni-ions by switching to a reductive potential (e.g. 0.8 V vs, NHE) for 1.5 days (Figure 5.1) during long-term operation at catalytic potentials in order to increase the catalytic current.

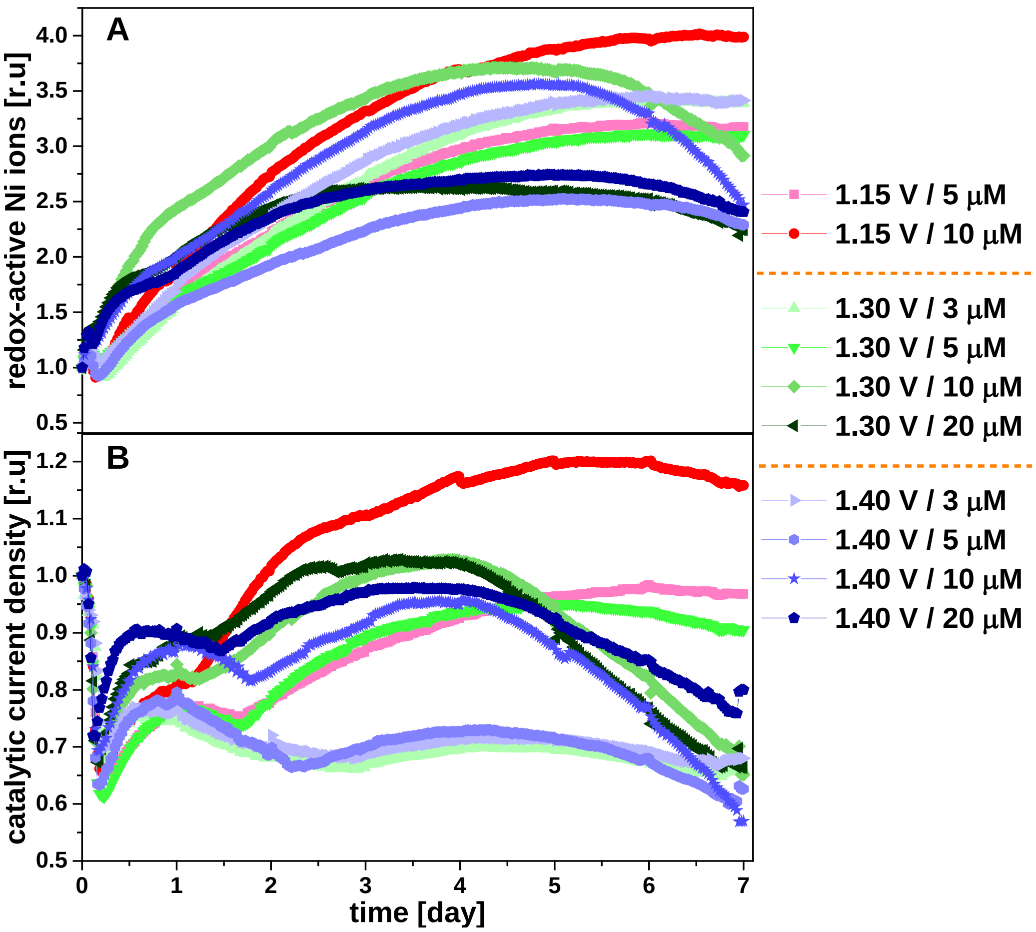

Figure 5.3. Water oxidizing nickel-oxide films operated in Ni-containing 0.1 M $KB(OH)_3$ at pH 9.2 (Ni-concentration of 3, 5, 10, 20 μM) at selected electrochemical potentials (1.15, 1.30, 1.40 V vs. NHE). The amount of redox-active Ni ions **(A)** and the catalytic current density **(B)** determined by integration of region in the negative cathodic CV scan during operation of nickel-oxide films at indicated potentials (0.80-1.40 vs NHE) over the course of one week. Every 30 minutes of chronoamperometry CVs are recorded and the second of two scans with a scan rate of 20 mV s^{-1} was analyzed. The data were normalized by the initial CV. Every 24 hours the chronoamperometry data correspond to Tafel slope was recorded. The mean value of the redox-charge and the catalytic current density of the initial CV of all samples were about 7 mC/cm^2 and 1.5 mA/cm^2, respectively.

The TXRF results (Figure 5.4) reveal that the absolute amount of nickel present in the NiCat follows the trend of the redox activity only for 1.15 V vs. NHE, and for low concentration (3 μM) of catalytic potentials (1.3 V and 1.4 V). When NiCat is operated at catalytic potential in higher concentration (>3 μM) the amount of NiCat increased while the redox charge is decreased, because the film is too thick (mass transport limitations).

For all potentials, an apparent increase of Ni ions is observed over increasingly high Ni concentrations in the buffer. Although the NiCat can gain more material from increasingly available Ni ions in solution, the redox-active sites are negatively affected by the same increase in Ni ions in the buffer solution.

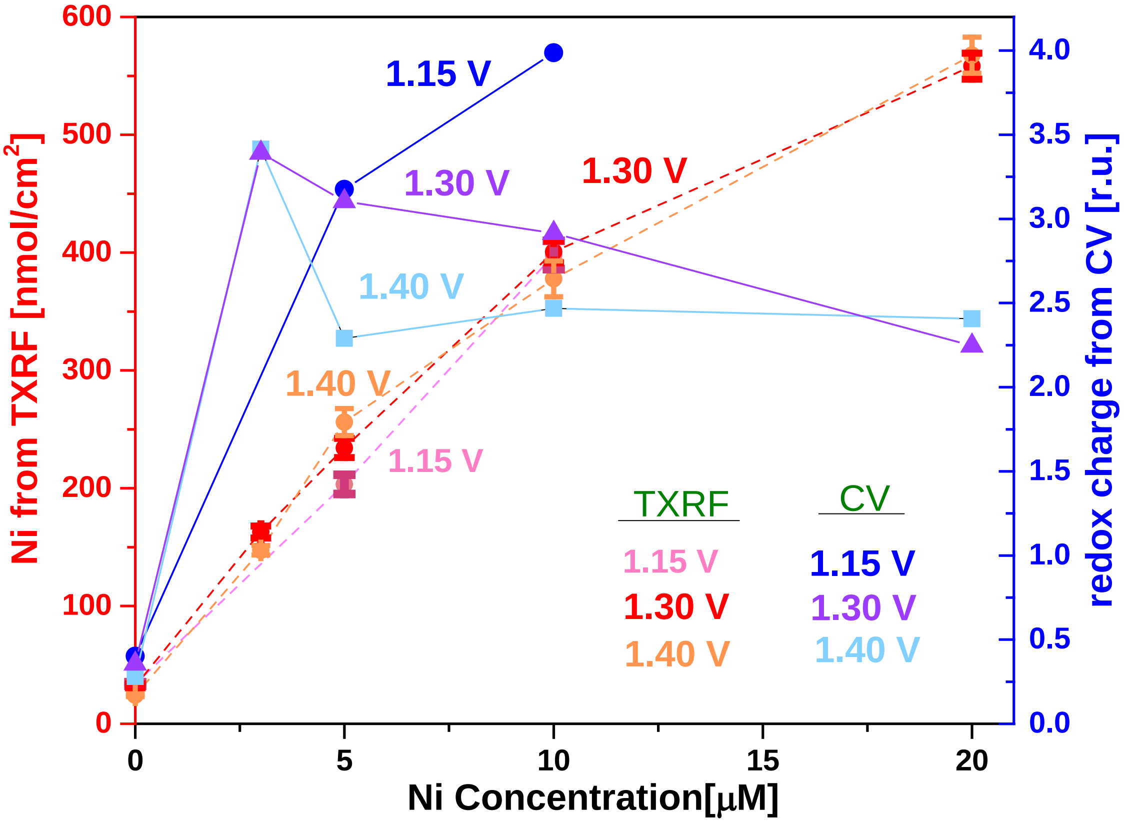

Figure 5.4. The left Y-axis (red) shows the amount of nickel extracted by chemical analyses of catalysts operated for one week in Ni-containing buffer (0.1 M $KB(OH)_3$ at pH 9.2).The right Y-axis (blue) shows the redox-charge normalized to the first CV. The initial amount of Ni atoms was 37 nmol/cm^2. The transferred redox-charge during the cathodic scan of the first CV was approximately 7 mC/cm^2. Lines are guides for the eye.

5.2.3 Tafel slope of NiCat

To understand the kinetic mechanism of samples operated in Ni-free and Ni-containing buffer, the Tafel slope of NiCat has been investigated for as-deposited samples and operated for one week at catalytic and non-catalytic electrode potentials in Ni-free and Ni-containing borate buffer (0.1 M $KB(OH)_3$ at pH 9.2). Tafel slopes were collected the following: Chronoamperometry measurements (potential jumps) of NiCat for one minute were carried out and the steady state currents were extracted. Potential jumps were applied from 0.9 V to 1.45 V vs. NHE with a step size of 10 mV. The steady state current after 1 min was plotted versus the applied potential and the linear part of the curve was fitted and the inverse of the slope was extracted as Tafel slope. From 1.05 V to 1.15 V vs. NHE the current density versus potential is linear (the corresponding graph are shown in the appendix). The results are shown in Figure 5.5. The Tafel slopes of the as-deposited NiCat samples are expected to be the same; variation from the average Tafel slope of 111 mV/dec reflects the precision of the experiment.

Figure 5.5-A shows that after one-week operation in Ni-free buffer the Tafel slopes are decreased to 50 and 30 mV/dec for 0.8 and 0.9 V, respectively. However, it is higher for higher potentials, where it is 70-80 mV/dec depending on the operation potentials. Low operation potentials of 0.80 and 0.90 V vs. NHE help to decrease the Tafel slope drastically. A low Tafel slope after operation means that the kinetic process is faster than in the as-deposited sample. When NiCat is operated in Ni-containing buffer at non-catalytic and catalytic electrode potentials, the Tafel slope decreases only slightly (Figure 5.5-B), except when it operated in high concentration Ni-containing buffer (20 µM) at catalytic potentials (1.3 and 1.4 V vs. NHE). Figure 5.5-B shows that the Tafel slopes increase with potential and Ni^{2+} concentration.

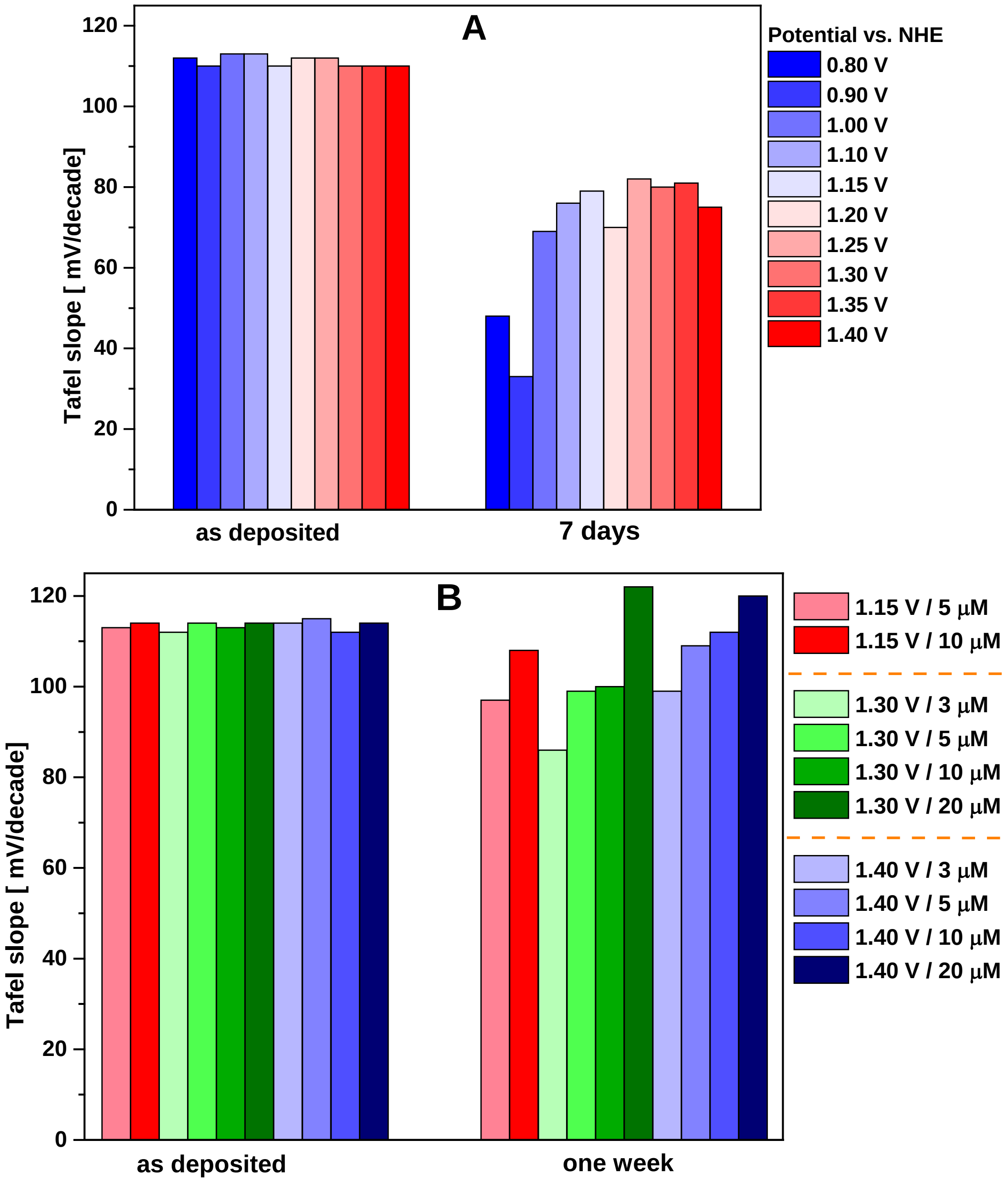

Figure 5.5. Tafel slopes of NiCats as deposited and operated for one week in Ni-free **(A)** and Ni-containing **(B)** borate buffer (0.1 M $KB(OH)_3$ at pH 9.2) at catalytic and non-catalytic electrode potentials. Chronoamperometry measurements (potential jumps) of NiCat for one minute were carried out and the steady state currents were extracted. Potential jumps were applied from 0.9 V to 1.45 V vs. NHE with a step size of 10 mV. The steady state current after 1 min was plotted versus the potential and the linear part of the curve was fitted. The inverse of the slope was extracted as Tafel slope. The potential interval in which the current has a linear relationship with potential was from 1.05 V to 1.15 V vs. NHE.

5.2.4 Shift in oxidation/reduction peak of CV

During operation of NiCat in Ni-free and Ni-containing borate buffer (0.1 M $B(OH)_3$ at pH 9.2) at non-catalytic and catalytic electrode potentials, there are drastic changes in the oxidize/redox waves of the CVs (Figure 5.6). For a more detailed insight, the mean value of the maximum oxidation wave and the minimum reduction wave (half wave potential; $E_{1/2}$) of all CVs are plotted in Figures 5.7 and 5.8. This voltage shift can be responsible for the loss of activity as it is likely that an oxidized $Ni^{3+/4+}$ species is needed for water oxidation catalysis(González-Flores, Klingan et al. 2018, Smith, Pasquini et al. 2018).

Figure 5.7-A shows the half-wave potential of NiCat, which was operated at catalytic and non-catalytic potentials in Ni-free buffer. When NiCat is operated at 0.8 V and 0.9 V vs. NHE, within the initial 6 hours operation, $E_{1/2}$ sharply increased then the slope of increase is lower for about 24 hours. After that, it is increasing gradually. Operation at other potentials (1 - 1.4 V) show a drastic increase of $E_{1/2}$ for the initial 6 hours operation and then it was decreased and after that increase gradually. The decrease of $E_{1/2}$ for 1.1 V is higher than other potentials.

Figures 5.7-B presents the half-wave potential of NiCat were operated at catalytic and non-catalytic potentials in Ni-containing buffer. $E_{1/2}$ is increasing dramatically within the initial 6 hours operation like operation in Ni-free buffer. However the slope of the increase is higher in this case. Then it is decreased for 6 hours and reached the minimum amount and then it is rising continuously the whole time.

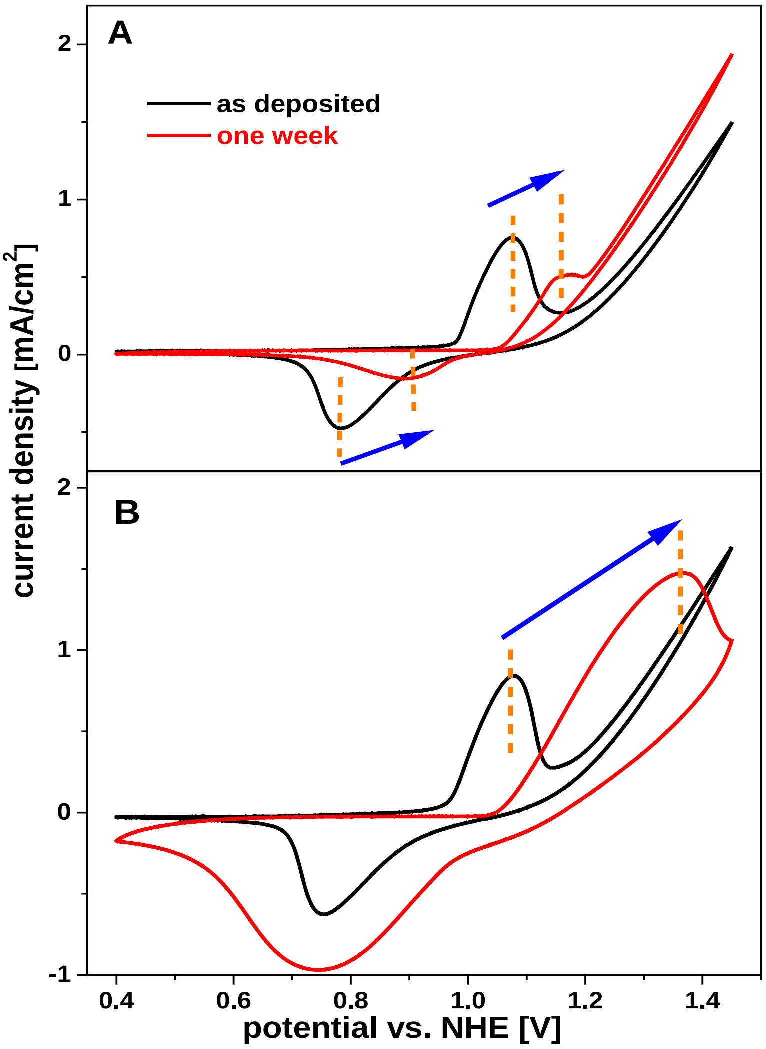

Figure 5.6. Cyclic voltammogram of the 2nd cycle for as-deposited 10 mC NiCat film (black) and operated for one week (red) at 1.3 V vs. NHE in **Ni-free buffer** (A) and in **10 µM Ni borate buffer** (B) at pH 9.2 (0.1 M $B(OH)_3$) with a scan rate of 20 mV s^{-1}.

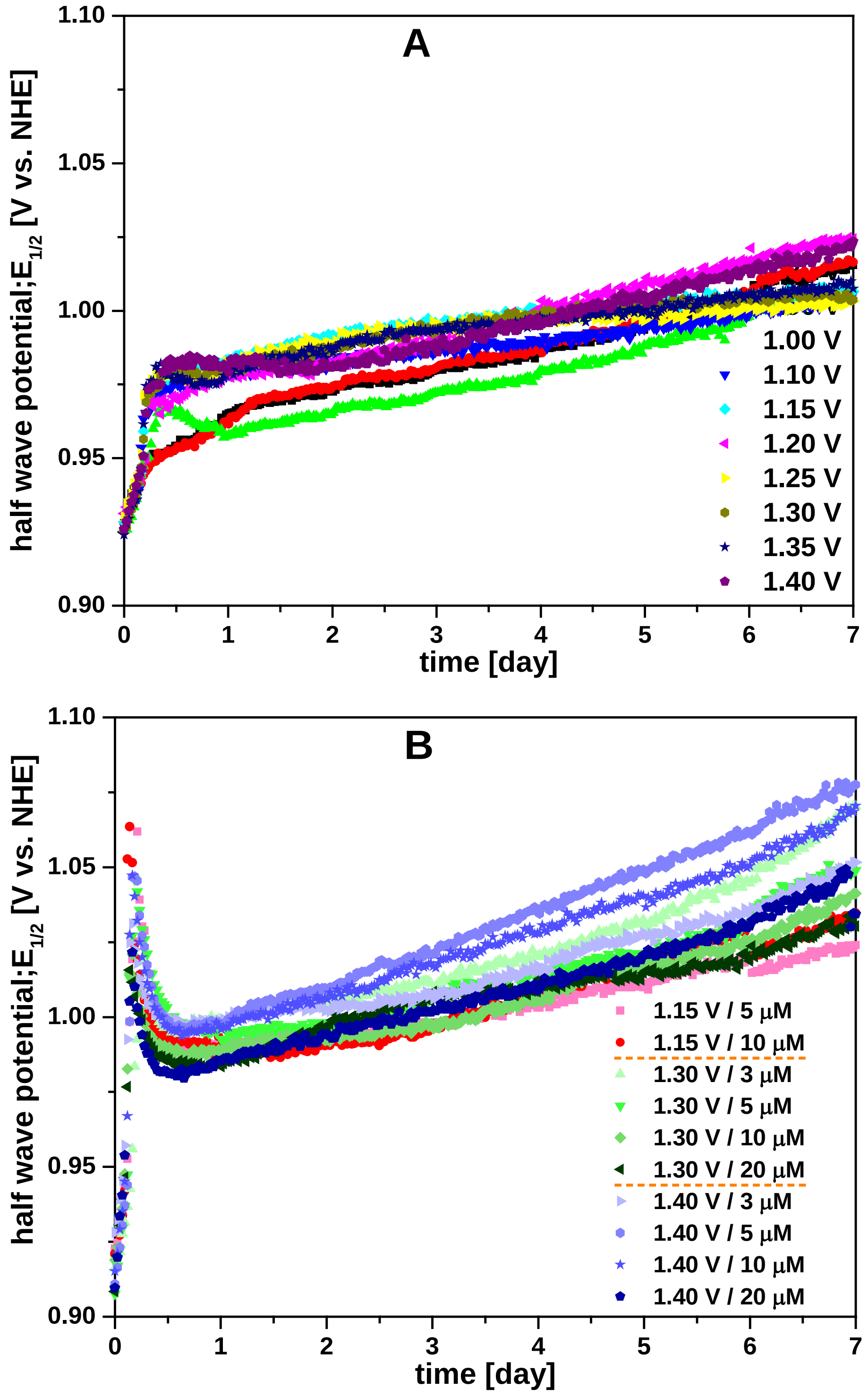

Figure 5.7. The averaged value of the maximum oxidation wave and the minimum reduction wave (half wave potential; $E_{1/2}$) of all CVs were recorded every 30 minutes during NiCat operation for one week in **Ni-free** (A) and **Ni-containing** (B) borate buffer (0.1 M $KB(OH)_3$ at pH 9.2) at non-catalytic and catalytic potentials. All potentials are given in Volt versus NHE.

5.2.5 Possibility of Fe contaminations

As Figure 5.1-B shows that the catalytic current of NiCat is decreasing during half-day operation and then it is growing gradually. These changes could be related to structural changes, which are discussed in the next chapter, or maybe it is associated with iron contamination. The TXRF results show that the ratio of Fe to Ni for as-deposited sample is 1:500, however this ratio is 1:8 and 1:5 for samples were operated at 0.9 V and 1.4 V vs. NHE, respectively. The basic question is that from where Fe atoms come?

They most likely come from glassware so the glass cell was changed to plastic one and NiCats were operated at 0.90 and 1.40 V vs. NHE in 0.1 M $KB(OH)_3$ at pH 9.2 for one week. Figure 5.8-A, C show that changing the electrochemical cell has a significant effect on the catalytic current. When NiCat is operated in a glass cell the catalytic current after one-week operation is about 50% higher than the initial amount while if it is operated in a a plastic cell the catalytic current is lower than the initial amount. Therefore, it shows that the slow activation phase is strongly diminished when the Fe-free plastic container is used.

We also performed a further experiment to show that the catalytic current is somehow restored if Fe is added when NiCat is operated in a plastic electrochemical cell. NiCats were operated at a non-catalytic potential (0.9 V) and catalytic potential (1.4 V) in 0.4, 0.8, 1.6, 3.2 and 6.4 µM and the results are shown in Figure 5.8-B, D. The results show that operation in Fe-containing borate buffer increased the catalytic current. When NiCat is operated at 0.9 V in Fe-containing buffer, increasing Fe concentration to 3.2 µM enhanced the catalytic current while 0.8 µM has the highest effect on catalytic current if it is operated at 1.4 V.

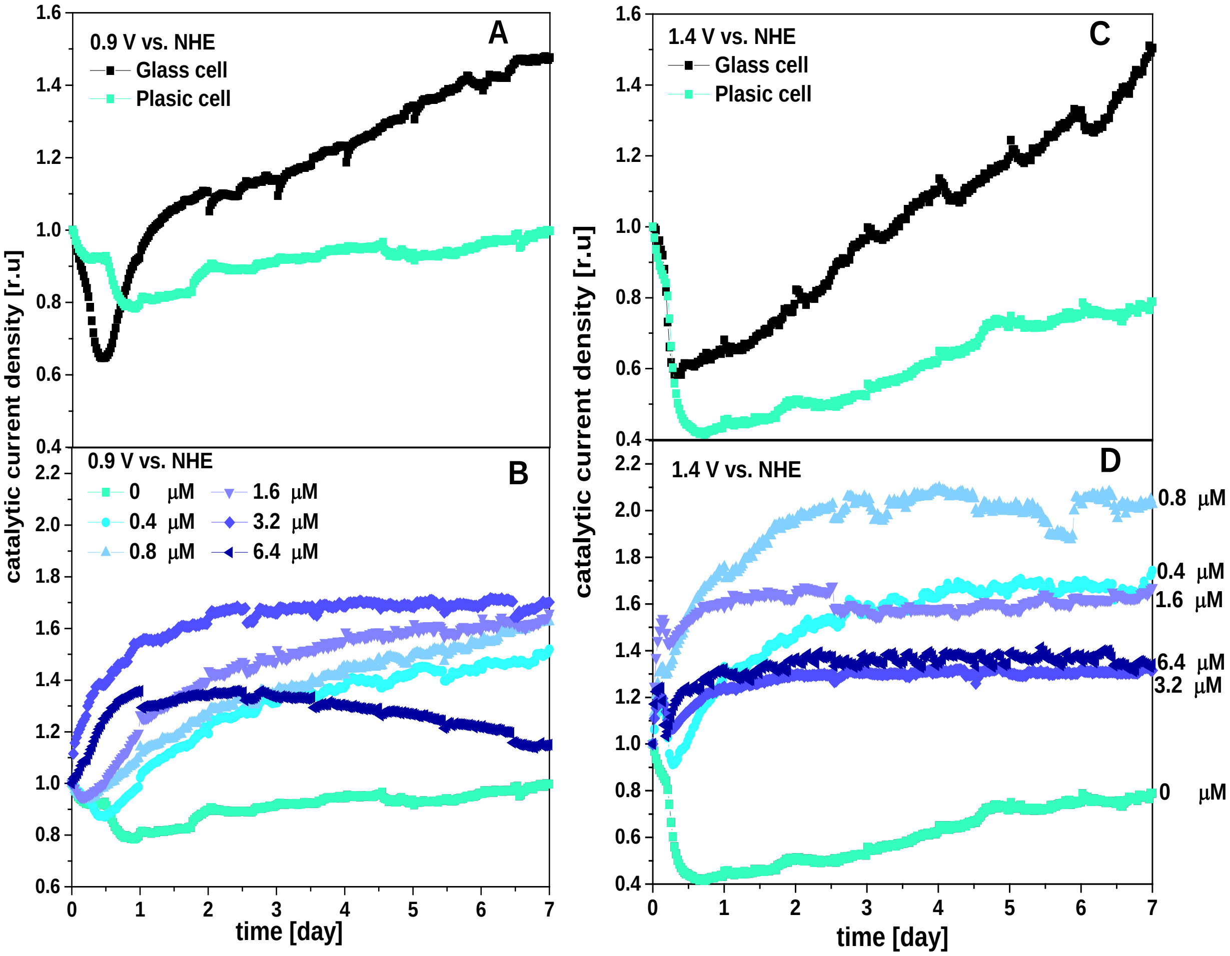

Figure 5.8. The amount of catalytic current density **(B)** determined by integration of negative cathodic CV scan during operation of nickel-oxide films in 0.1 M KB(OH)$_3$ at pH 9.2 at 0.90 V (**A, B**) and 1.40 V (**C, D**) over the course of one week. Every 30 minutes of chronoamperometry CVs (0.45 – 1.45 V vs. NHE) are recorded and the second of two scans with a scan rate of 20 mV s^{-1} was analyzed. The current density corresponds to 1.45 V vs. NHE was selected as a catalytic current and the data were normalized to the initial CVs. The effect of glass and plastic cells on catalytic current during operation are shown in **A** and **C**. The effect of adding a different concentration of iron ions in a plastic cell for samples operated at 0.9 V and 1.4 V are shown in **B** and **D**, respectively. The mean value of the catalytic current density of the initial CV of all samples was about 1.5 mA/cm^2.

5.3 Summary

- Long-term operation of NiCat in Ni-free buffer at non-catalytic and catalytic potentials reveals that the redox charge drastically decreases within the first day of operation and then reaches a stable condition. During the first day of operation, the rate of dissolution exceeds the self-assembling process. However, the catalytic current reaches a minimum after only 12 hours of operation. This means that the minimum of redox charge and the catalytic current are not consistent. This strongly points towards a change of the atomic structure during operation. Therefore, we studied the NiCat atomic structure by X-ray absorption spectroscopy analysis and the result are shown in the following chapter. Surprisingly the Tafel slope of NiCat after one-week operation is lower than for the as-deposited sample.

- Long-term operation of NiCat in Ni-containing buffer at non-catalytic and catalytic potentials shows that the redox charge decreases slightly within the early hours of operation, then increases to reach a maximum, and then it goes down again. The maximum point of activity depends on the potential as well as the nickel concentration. However, there is a drastic loss in catalytic current after about 12 hours of operation.

- Operation of the NiCat in Ni-free and Ni-containing buffer at non-catalytic and catalytic potentials causes a potential dependent change of the oxidation and reduction waves. The average of oxidation and reduction points shifted to a higher potential.

- Operation of NiCat in Fe-containing buffer (< 2 μM) enhance the catalytic current. If we use a glass cell, Fe contamination of glassware improves the catalytic activity.

Chapter 6

XAS study of NiCat

Structural and functional changes in the NiCat

Using X-ray absorption spectroscopy (XAS), we investigated the structure of a nickel oxide catalyst film (NiCat) operated at catalytic and non-catalytic potentials as well as time-resolved oxidation-state change kinetics by *in-situ* measurements.

XAS results show that operation at catalytic potential induces a structure similar to γ-NiOOH, which is largely stable over electrolysis time.

The minimum catalytic activity of samples operated for 11 hours at non-catalytic potentials (0.8 and 0.9 V vs. NHE, see chapter 5) is related to a rather ordered amorphous nickel oxide. However, after 48 hours operation the catalyst is more disordered, and the initial Ni-O and Ni-Ni distances are split, explainable by distortion of the NiO_6 octahedral.

Furthermore, the *in-situ* measurement shows that the reduction process does not finish within 10 seconds, but slowly continues which means that not all nickel atoms are fully reduced even after half an hour operation.

Portions of this chapter have been prepared for the publication that was indicated in chapter 5.

6.1 Experimental Section

6.1.1 Materials

The details of the materials were described in section 5.1.1.

6.1.2 Electrodeposition of NiCat

The NiCat was anodically electrodeposited from 0.1 M $B(OH)_3$ (Bi) and 0.5 mM $Ni(NO_3)_2$ solution at pH 9.2 and a deposition potential of 1.15 V vs. NHE. The buffer solution of 0.1 M $B(OH)_3$ was adjusted to pH 9.2 with small amounts of a saturated NaOH solution. The deposition was stopped at a charge of 10 mC cm^{-2} (ITO on glass) and 50 mC cm^{-2} (ITO on Mylar) for low-temperature and *in-situ* measurements, respectively. More details are given in section 5.1.2.

6.1.3 XAS sample preparation without potential applied at low temperature (20 K)

The electrode substrate for the NiCat was ITO coated on glass (Visiontek Systems Ltd). After electrochemical operation, the NiCats were washed with buffer solution (0.1 M H_3BO_3, pH 9.2), mounted to the sample holders, and frozen in liquid nitrogen prior to the synchrotron measurements.

6.1.4 XAS sample preparation with applied potential (freeze-quench or quasi-*in situ*) at low temperature (20 K)

NiCat was electrodeposited on ITO substrate coated on polyethylene terephthalate sheets (ITO on PET, Sigma Aldrich Chemie GmbH Munich, GER).The size of the cutted substrate was 25 mm x 14 mm. Half the area was covered with Kapton tape and copper tape for the electrode clamp connection. The substrate was cleaned with ethanol and attached to the cell made of transparent PVC (33 mm x 19 mm x 2 mm) with a window of 14 mm x 14 mm. The backside was covered by Kapton tape that does not allow the buffer to come out from the cell when the sample is frozen. This cell has two holes drilled for insertion of a platinum wire, which serve as a counter electrode within freezing sample at specific potential (More details can be found in ref (Zaharieva, González-Flores et al. 2016). After electrodeposition, samples were operated for 24 hours at 0.9 V and 1.4 V.

For freezing the sample at a certain potential of the working electrode, a two-step procedure for the electrochemical conditioning was applied. In the first step, the sample was kept at the desired working electrode potential for a certain time and the potential difference between working electrode and counter electrode was recorded simultaneously. After that, the reference electrode was removed and its cable was connected to the counter electrode. In a second step, the equilibrium value of the beforehand determined potential difference (between working electrode and counter electrode), was applied as a new working electrode potential.

After 24 hours operation, the cell was cleaned with 0.1 M H_3BO_3. Then 0.90 V and 1.40 V were applied for three minutes in 0.1 M H_3BO_3 at pH 9.2 and the potential between the counter electrode and the working electrode was recorded simultaneously. After that, the reference electrode was removed and the determined potential was applied between the working and counter electrode for 3 minutes. After three minutes, the whole sample was quickly and carefully frozen in liquid nitrogen under continuous application of a voltage between working and counter electrode. Then samples were stored in liquid nitrogen for XAS measurements at BESSY.

6.1.5 X-ray absorption spectroscopy (XAS)

X-ray absorption spectroscopy was used for the assessment of structural changes at the atomic level. XAS measurements (EXAFS, XANES) at the nickel K-edges were performed. The excitation energies were selected by a double-crystal monochromatic (Si-111), such that the scan range was 8215-9378 eV (Ni K-edge XAS). The angle between the NiCat surface and the incident beam was approximately 45° (fluorescence mode). Each spot on the examined NiCat films was exposed for less than 35 min to synchrotron radiation at 20 K. After each scan the spot location was changed vertically by 0.5 mm. More details were given in section 4.3.5.

6.1.6 XAS data extraction

The details of XAS data extraction were given in section 4.3.6.

6.1.7 *In-situ* XAS sample preparation – room temperature (293K)

The details were given in section 4.3.4.

6.1.8 ***In-situ*** **X-ray absorption spectroscopy**

For *in-situ* XAS measurements, NiCat was deposited with five times (50 mC/cm^2) higher concentration (charge deposited) to improve the signal to noise ratio. This has been done in a separate electrochemical setup. The buffer solution of 0.1 M $B(OH)_3$ was adjusted to pH 9.2 with small amounts of a saturated NaOH solution. The concentration of nickel was 50 mmolL^{-1} and the substrate was ITO coated polyethylene terephthalate sheets (ITO on PET, Sigma Aldrich Chemie GmbH Munich, GER), which were cut to fit the sample holders (18 mm x 20 mm). After electrodeposition NiCat was attached to the in-situ cell. The uncompensated resistance (R_u) was about 100 **Ω**. Measurements were conducted at ambient condition (25 °C, 1 atm) and the Ni K-edge fluorescence was monitored perpendicular to the incident beam by a scintillation detector coupled to a photomultiplier. The detector was shielded by a thick cobalt foil (10 μm Co, ≥ 99.99 %, Goodfellow, Bad Nauheim, GE) against scattered X-rays and visible light.

More details were given in section 4.3.5 and 5.1.2.

6.2 Results and Discussions

Ex-situ and in-situ XAS experiments were performed to understand the structural changes and the reaction kinetics of NiCat.

6.2.1 Ex-situ results - low temperature (20K)

In the previous chapter, the stability and self-healing properties of the NiCat were investigated by electrochemical methods over the course of one week (Figure 5.3). We have seen that after 11 h of operation at non-catalytic potentials (0.80 and 0.90 V vs. NHE) and 17 h hours of operation at catalytic potentials (1.40 V vs. NHE) the catalytic currents reach a minimum. Furthermore, although the amount of redox-active Ni ions is significantly decreased the catalytic activity undergoes a stabilization effect for prolonged electrolysis. To get insight into the atomic structure during these conditions, we have investigated the structure-function relation by XAS for two days operation at catalytic and non-catalytic electrode potentials.

As Figure 5.1-B shows, after 11 hours of operation at redox potentials (0.80 and 0.90 V vs. NHE) and 17 hours of operation at catalytic potentials (1.40 V vs. NHE) the catalytic currents reach a minimum. In addition, although the amount of redox-active Ni ions is significantly decreased (Figure 5.1-A) the catalytic activity increases for prolonged electrolysis (Figure 5.1-B). X-ray absorption spectroscopy of these samples, the as-deposited sample and the sample operated for 48 hours, were performed to distinguish the changes in catalytic current is related to structural changes. The results are shown in Figure 6.1. The Fourier transform of the EXAFS-spectra shows a high main Ni-O peak (at a reduced distance of 1.5 Å) that corresponds to di-µ-oxo-bridged Ni ions. This peak can be simulated by two Ni-O shells (Table 6.1). The second peak of the Fourier transformed (at a reduced distance about 2.5 Å) correspond to Ni-Ni distances. Furthermore, a peak reflecting the bent version of double distance and also a double distances peak are detectable in the Fourier transform (dashed lines 3 and 4 in Figure 6.1). The motifs were shown in Figure 6.1, in which the green and red circles correspond to nickel and oxygen, respectively.

The minimum catalytic activity at operation for 11 hours at non-catalytic potentials (0.8 and 0.9 V vs. NHE) is related to a rather ordered amorphous nickel-oxide. As the catalytic activity is almost stabilized (after 48 hours), the catalyst gets more disordered, and the initial Ni-O and Ni-Ni distances are split caused by distortion of the NiO_6 octahedral. Operation at catalytic potential (1.4 V vs. NHE) induces a structure similar to γ-NiOOH, which is majorly stable over electrolysis time. These results highlight that long term operation at different electrochemical potentials can induce different nickel-oxide phases, where the most ordered γ-NiOOH phase does not present the most active phase. The data with the corresponding simulations are shown in Figure 6.1 and the simulation results are shown in Table 6.1. The simulations were carried out as a joint fit in which the Debye-Waller factors were determined by the program for the first shells (Ni-O and Ni-Ni) and fixed for the other shells to avoid over-parameterization. The coordination numbers and the atomic distances were calculated by the program. The summed number of oxygen and nickel atoms each were fixed to be equal to six.

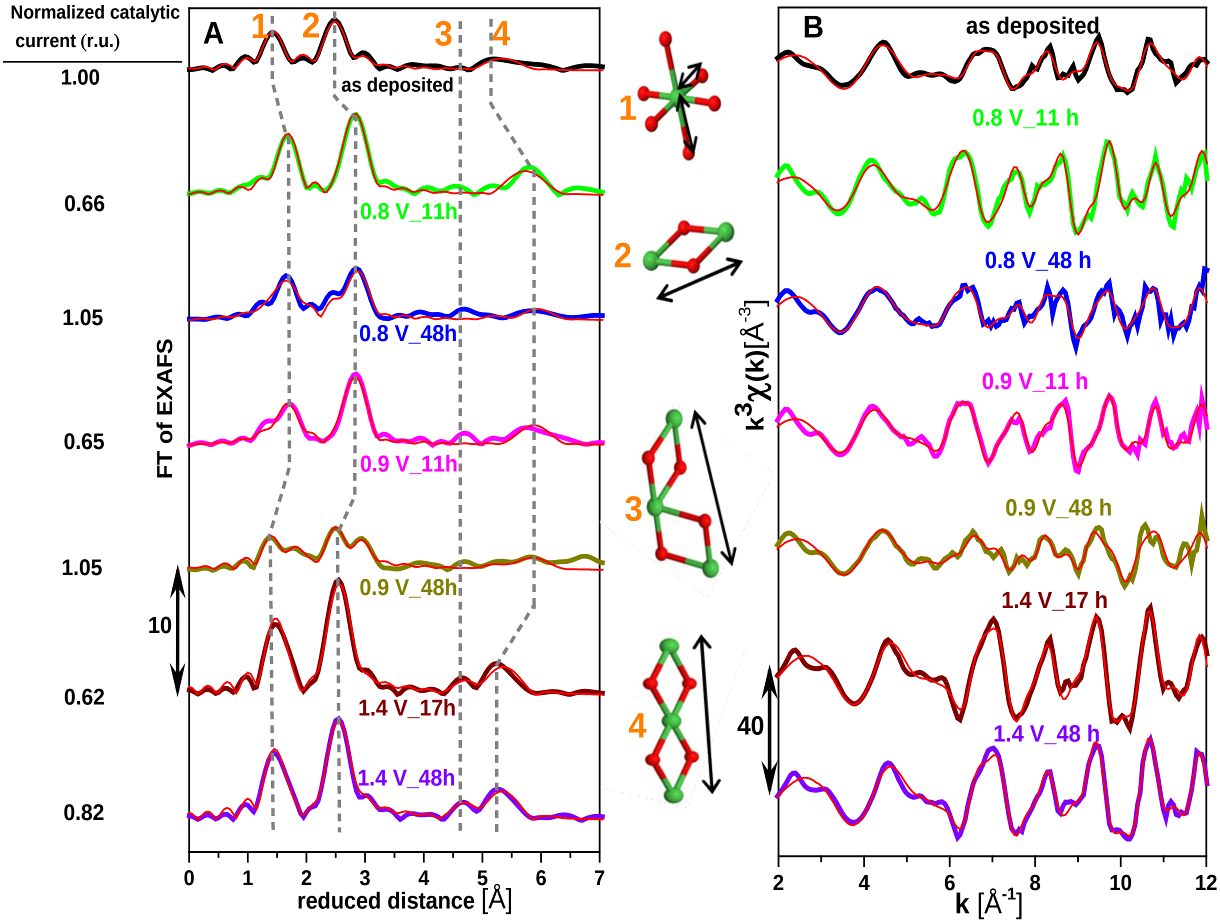

Figure 6.1. (A) Fourier-transformed EXAFS spectra of NiCats as deposited (black), operated at 0.80 V vs NHE for 11 h (green) and 48 h (blue), operated at 0.90 V vs NHE for 11 h (pink) and 48 h (dark yellow), and operated at 1.40 V vs NHE for 17 h (wine) and 48 h (violet). The thick lines are the experimental data and the thin red lines are the simulation results. The corresponding simulation parameters are provided in Table 6.1. Note that the distance on the x-axis is reduced by 0.3-0.4 Å relative to the real distance. The Ni-O or Ni-Ni distances are marked at the corresponding FT peaks and the identified structural motifs are displayed schematically. Color codes are the following: nickel, green; and oxygen, red. (B) Experimental EXAFS simulations in k-space (thick lines) and their simulation (thin red lines) between 3 and 13.5 $Å^{-1}$ of long-term electrolysis NiCats at indicated potentials.

Table 6.1. Parameters obtained by simulation of the k^3-weighted EXAFS spectra. The simulated spectra correspond to the Fourier-transformed EXAFS spectra shown in Fig. 6.1. (N: coordination number; R: absorber-backscatter distance, RFF: R-factor filtered). The number in parentheses corresponds to the errors representing 68% confidence intervals of the respective fit parameters. The Debye-Waller parameter (σ) of all samples for oxygen and nickel shells were determined by the simulation program. The amplitude reduction factor, S_0^2, was fixed to 0.85 as suggested by simulations.

Type of bond	**As deposited**			
	R [Å]	**N**	**σ [Å]**	**RFF**
Ni-O$_{short}$	1.88 (0.01)	3.4 (0.2)	0.044	14
Ni-O$_{long}$	2.08 (0.01)	2.6	0.044	
Ni-Ni$_{short}$	2.82 (0.01)	4.1 (0.1)	0.066	
Ni-Ni-Ni	5.65	4.1	0.066	
Ni-Ni-Ni (MS)	5.65	2.7(0.4)	0.066	
Ni-Ni$_{long}$	3.04 (0.01)	1.9	0.066	
Ni-Ni-Ni	6.07	1.9	0.066	
Ni-Ni-Ni (MS)	6.07	0.9 (0.4)	0.066	
Ni-Ni	-----------	----------	-------	

Type of bond	**1.40 V vs. NHE** **17 h**				**1.40 V vs. NHE** **48 h**			
	R [Å]	**N**	**σ [Å]**	**RFF**	**R [Å]**	**N**	**σ [Å]**	**RFF**
Ni-O$_{short}$	1.87 (0.01)	4.6 (0.3)	0.020	13	1.86 (0.01)	4.4 (0.3)	0.027	12
Ni-O$_{long}$	2.03 (0.02)	1.4	0.020		2.02 (0.02)	1.6	0.027	
Ni-Ni$_{short}$	2.83 (0.01)	5.3 (0.1)	0.041		2.83(0.03)	4.8 (0.1)	0.042	
Ni-Ni-Ni	5.66	5.3	0.041		5.66	4.8	0.042	
Ni-Ni-Ni (MS)	5.66	3.7 (0.3)	0.041		5.66	3.7 (0.3)	0.042	
Ni-Ni$_{long}$	3.05 (0.01)	0.7	0.041		3.06 (0.01)	1.2	0.042	
Ni-Ni-Ni	6.1	0.7	0.041		6.11	1.2	0.042	
Ni-Ni-Ni (MS)	6.1	0.6 (0.2)	0.041		6.11	0.9 (0.3)	0.042	
Ni-Ni	4.91	2.1 (0.5)	0.041		4.91	2.7 (0.5)	0.042	

Type of bond	**0.90 V vs. NHE** **11 h**				**0.90 V vs. NHE** **48 h**			
	R [Å]	**N**	**σ [Å]**	**RFF**	**R [Å]**	**N**	**σ [Å]**	**RFF**
Ni-O$_{\text{short}}$	1.93 (0.03)	0.1 (0.1)	0.089	16	1.89 (0.01)	2.8 (0.1)	0.034	19
Ni-O$_{\text{long}}$	2.04 (0.1)	5.9	0.089		2.07 (0.01)	3.2	0.034	
Ni-Ni$_{\text{short}}$	2.84 (0.06)	0.3	0.065		2.85 (0.01)	3.2 (0.1)	0.053	
Ni-Ni-Ni	5.68	0.3	0.065		5.69	3.2	0.053	
Ni-Ni-Ni (MS)	5.68	0.01 (0.3)	0.065		5.69	1.7 (0.3)	0.053	
Ni-Ni$_{\text{long}}$	3.08 (0.01)	5.7 (0.2)	0.065		3.06 (0.01)	2.8	0.053	
Ni-Ni-Ni	6.2	5.7	0.065		6.12	2.8	0.053	
Ni-Ni-Ni (MS)	6.2	4.7 (0.5)	0.065		6.12	2.5 (0.3)	0.053	
Ni-Ni	---------	--------	--------		----------	--------	--------	

Type of bond	**0.80 V vs. NHE** **11 h**				**0.80 V vs. NHE** **48 h**			
	R [Å]	**N**	**σ [Å]**	**RFF**	**R [Å]**	**N**	**σ [Å]**	**RFF**
Ni-O$_{\text{short}}$	2.03 (0.02)	5.7 (1.4)	0.058	18	1.96 (0.01)	2.9	0.037	18
Ni-O$_{\text{long}}$	2.19 (0.25)	0.3	0.058		2.11 (0.02)	3.1 (0.3)	0.037	
Ni-Ni$_{\text{short}}$	2.91 (0.01)	0.3	0.053		2.85 (0.01)	1.6	0.062	
Ni-Ni-Ni	5.82	0.3	0.053		5.70	1.6	0.062	
Ni-Ni-Ni (MS)	5.82	1.4 (0.4)	0.053		5.70	1.1 (0.3)	0.062	
Ni-Ni$_{\text{long}}$	3.08 (0.01)	5.7 (0.3)	0.053		3.08 (0.01)	4.4 (0.1)	0.062	
Ni-Ni-Ni	6.2	5.7	0.053		6.16	4.4	0.062	
Ni-Ni-Ni (MS)	6.2	3.6 (0.5)	0.053		6.16	3.0 (0.4)	0.062	
Ni-Ni	-----------	----------	--------		------------	---------	--------	

To understand if these structural changes are related to long-time operation or short time operation as well, after electrodeposition NiCat, they were operated for 3 minutes at reduction potential (0.9 V vs. NHE) and oxidized potential (1.45 V vs. NHE). Then they were frozen in liquid nitrogen while the potential was applied (quasi *in-situ*). Furthermore, two samples were operated for 24 hours at 0.9 V and 1.4 V vs. NHE and frozen. The results are given in Figure 6.2. Exposure of NiCat to 0.90 V for 24 h results in a severe shift of the edge position (by 0.9 eV) towards higher energies (Figure 6.2-A). This energy difference of 0.9 eV corresponds to a nickel oxidation state of +2.3 for the steady state film and +2.8 for the 24 h operated film. The difference between the NiCat at 1.45 V and the one operated for 24 h at 1.40 V corresponds to a change in integral edge position of 1.1 eV, in other words, nickel oxidation states of +3.0 at 1.45 V and +3.7 for the film operated for 24 h at 1.40 V (Figure 6.2-B). Long-term electrolysis clearly influences the oxidation state of the NiCat. The X-ray edge position of the catalyst film after long-term application at 1.40 V for 24 hours reaches the highest oxidation state observed in this experimental series.

Furthermore, we measured the XANES of some NiCat samples that were directly frozen after operation without applied potential. The data of as-deposited Ni catalyst film and operated samples at non-catalytic potentials (0.80 V and 0.90 V vs. NHE) for 11 h and 48 h as well as catalytic potential (1.4 V vs. NHE) for 17 h and 48 h are shown in Figure 6.3. Exposure of a NiCat to non-catalytic potentials (0.80 V and 0.90 V) for 48 h compare to 11 h results in a severe shift of the edge position towards higher energies (Figure 6.3). This energy difference of 0.4 eV for samples operated at 0.8 V corresponds to a nickel oxidation state of +2.3 for 11 hours operated sample and +2.5 for the 48 h operated film. On the other hand, there is a slight difference in the edge position of samples operated 17 h and 48 h. Long-term electrolysis clearly influences the oxidation state of the NiCat.

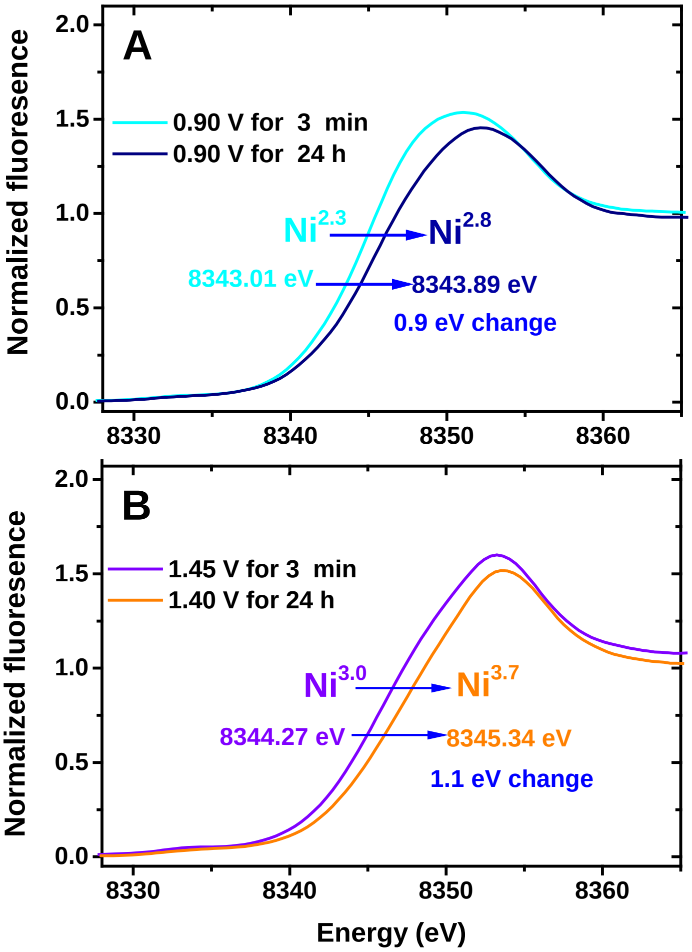

Figure 6.2. Nickel *K*-edge XANES spectra for Ni catalyst film samples: **(A)** Frozen at 0.90 V (Borate buffer, 0.1 M, pH 9.2) (cyan), and operated at 0.90 V for 24 h (royal). **(B)** Frozen at 1.45 V (violet), and operated for 24 h at 1.40 V (orange). All potentials are vs. NHE. The arrow indicates the shift of the X-ray edge for more oxidized NiCats to more positive energy values. Oxidation states were calculated by linear relation in Figure 6.4. The data of this Figure was taken from the thesis of Katharina Klingan.

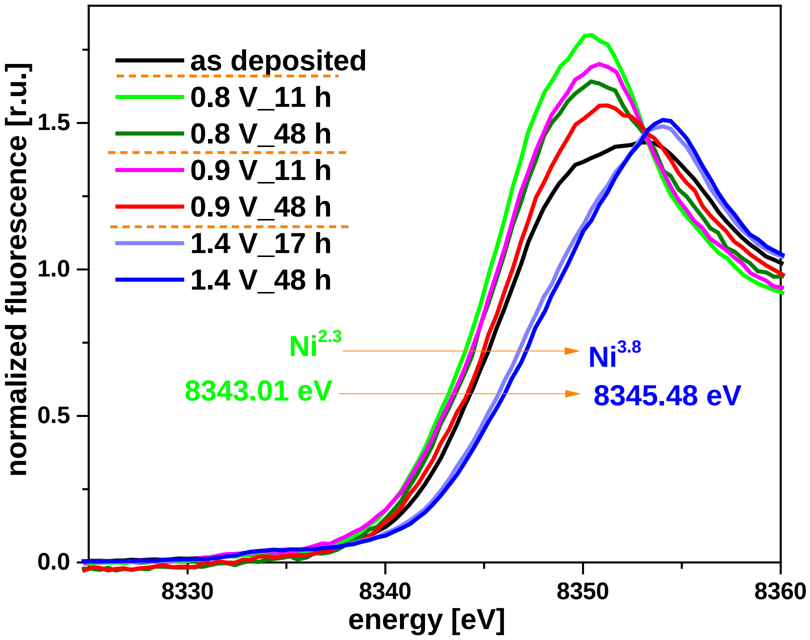

Figure 6.3. Nickel *K*-edge XANES spectra of as-deposited Ni catalyst film and operated samples at non-catalytic potentials (0.80 V and 0.90 V vs. NHE) for 11 and 48 hours as well as catalytic potential (1.4 V vs. NHE) for 17 and 48 hours. After electrodeposition (1.15 V vs. NHE, Borate buffer, 0.1 M, pH 9.2), as the deposited sample was rinsed with borate buffer and directly frozen in liquid nitrogen. The other samples were frozen the same way after operation at specific time and potentials were mentioned in the Figure. The operation time of these samples was discussed in chapter 5 and their corresponding Fourier-transformed EXAFS spectra are shown in Figure 6.1. All samples were electrodeposited on ITO on glass substrate and they were frozen directly after operation without applied potential.

6.2.2 In-situ results - ambient conditions (293 K)

To provide evidence for changes in the oxidation state of nickel catalyst while potential was applied at ambient conditions, XANES measurements were performed. First, dry sample of NiCat which was electrodeposited at 1.15 V vs. NHE was measured. The edge position of the dry sample was 8343.89 eV, which corresponds to an oxidation state of +2.8 ($Ni^{2.8+}$) based on the Ni oxide references (NiO, $Ni(H_2O)_6$, $LiNiO_2$ and $K_2Ni(H_2IO_6)_2$ as shown in Figure 6.4). Then in-situ XANES of the NiCat operated in catalytic and non-catalytic potentials was measured. When the potential changed from 0.40 to 1.80 V vs. NHE, the edge position shifted from 8342.75 eV to 8345.53 eV which corresponds to oxidation state changes from 2.1 to 3.8 (Figure 6.5). The edge position of XANES spectra points to a sharp oxidation-state change at around 1.1 V vs NHE which almost all Ni atoms convert from Ni^{2+} to Ni^{4+}. *In-situ* measurement of NiCat shows the average oxidation state of 2.1 when 0.8 V is applied (Figure 6.5). However, Cryo measurements display the average oxidation state of 2.3 and 2.5 for NiCat were operated for 11 h and 48 h, respectively (Figure 6.3). Furthermore, the edge position of *in-situ* measurement of sample was operated at 1.5 V is 8345.18 eV which corresponds to oxidation state of 3.6 (Figure 6.5), but Cryo measurement shows oxidation state of 3.8 for NiCat was operated at 1.4 V for 48 h (Figure 6.3). Suggesting that the oxidizing process of NiCat cannot completely happen within short time operation.

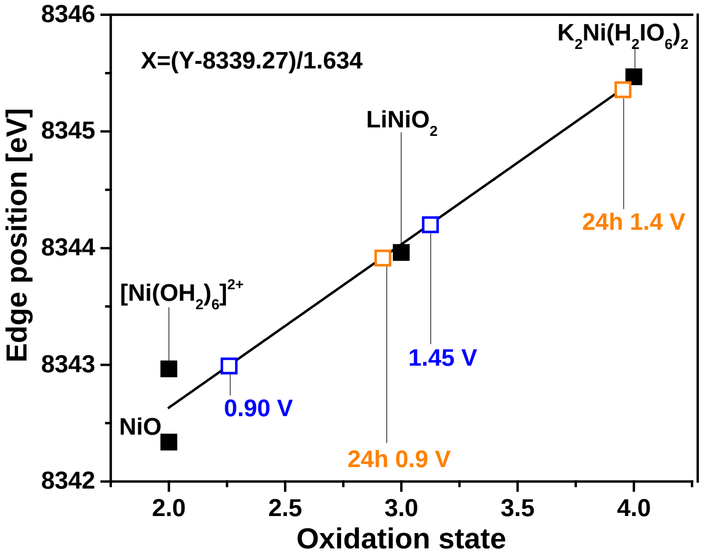

Figure 6.4. Calibration curve defined by a linear fit to determine oxidation states of nickel from XAS edge positions of different Ni compounds. Edge positions were determined from Ni *K*-edge XANES spectra by the integral method ($0.15 < \mu < 1$) (H. Dau, M. Haumann, *Anal. Bioanal. Chem.* **2003**). Reference samples from low oxidation state to high oxidation state: $Ni^{II}O$, $Ni^{II}(OH)_2$, $LiNi^{III}O_2$ and $K_2Ni^{IV}(H_2IO_6)_2$. The data of this Figure was taken from the thesis of Katharina Klingan.

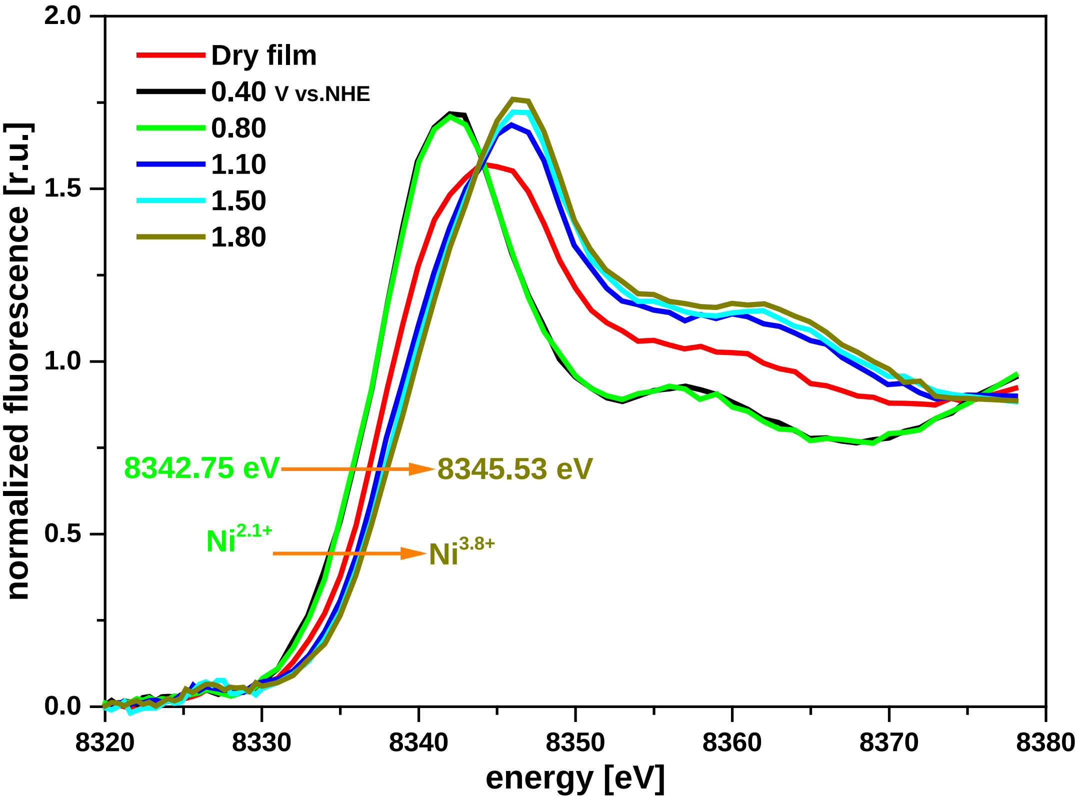

Figure 6.5. In-situ X-ray absorption measurement of Ni catalyst sample electrodeposited on ITO coated on polyethylene terephthalate sheets at 1.15 V vs. NHE in Bi buffer (pH 9.2). The Figure shows that average oxidation sate changes from 2.1 to 3.8 when the applied potential changes from 0.40 to 1.80 V vs.NHE.

To provide evidence for changes in the structure under applied potential EXAFS measurements at the K-edge of Ni with 0.40, 1.10 and 1.80 V vs. NHE applied potential were performed. The experimental and simulated EXAFS spectra of the NiCat at mentioned potentials are shown in Figure 6.6 and the simulation results are provided in Table 6.2. Jointly fitted simulations were carried out in which the Debye-Waller factors were fixed to avoid over-parameterization. The coordination numbers and the atomic distances were calculated by the program. Exposure to catalytic potentials of 1.80 V causes a contraction of the Ni-O and Ni-Ni distances in respect to non-catalytic potential of 0.40 V. The simulation results show that two main peaks of NiCat operated at 0.40 V vs. NHE contain sub-peaks, indicating a mixed nickel oxide phase. For 0.40 V, Ni-O$_{short}$ and Ni-Ni$_{short}$ distances are observed at 1.95 and 3.07 Å, respectively, corresponding probably to a γ-NiOOH phase; and Ni-O$_{long}$ and Ni-Ni$_{long}$ distances at 2.09 and 3.50 Å, corresponding probably to α-Ni(OH)$_2$ phase. However, when NiCat is exposed to 1.10 and 1.80 V vs. NHE the α-Ni(OH)$_2$ phase clearly disappears which is reflected in the contraction of Ni-O and Ni-Ni distances to lower values. Formation of shorter distances is usually associated with an increase in the oxidation state and/or deprotonation as it is obvious in Figure 6.6 for potential changing from 0.4 V ($Ni^{2.1+}$) to 1.8 V ($Ni^{3.8+}$).

We compared the experimental EXAFS spectra of in-situ NiCats operated at 1.1 V and 1.8 V vs. NHE with an ex-situ operated sample at 1.4 V for 48 hours and the results were represented in Figure 6.7. Both 1.4 V and 1.8 V vs. NHE are pretty high catalytic potentials and as Figure 6.7 shows after 48 hours operation at 1.4 V the amplitude peak corresponding to Ni-Ni distances is growing, suggesting that the Ni-Ni distances become more uniform in length after long time water oxidation reaction. Furthermore, the amplitude of Ni-Ni double distances is increased and it also becomes more uniform in length.

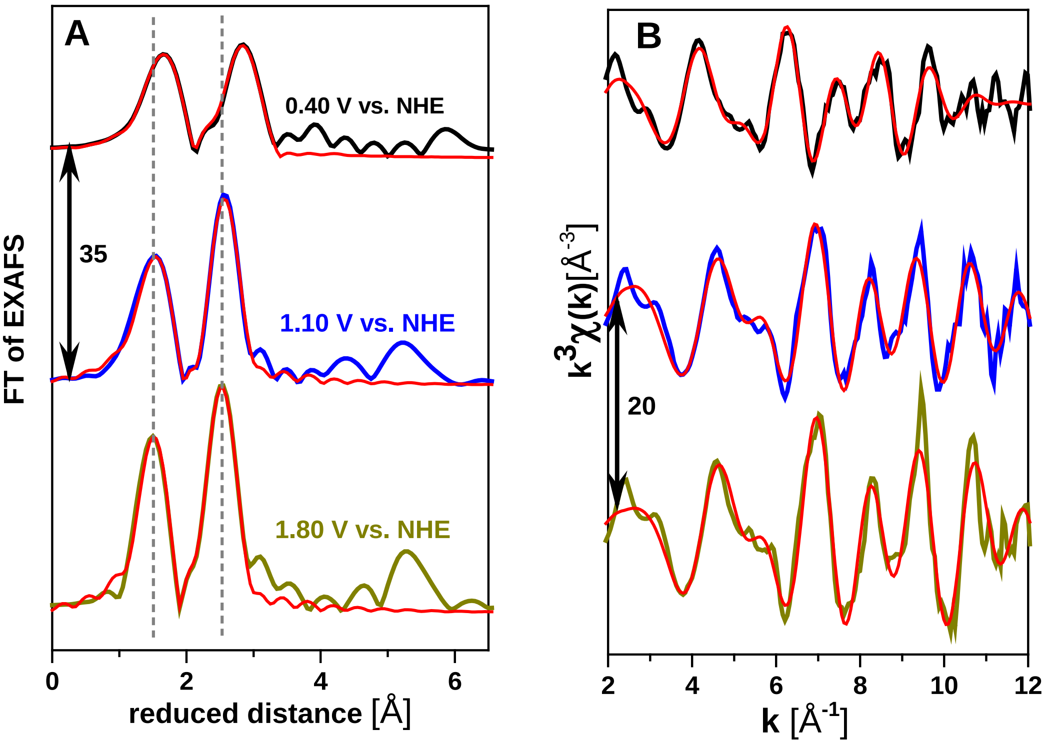

Figure 6.6. k^3-weighted $\chi(k)$ (A) and Fourier-transform of EXAFS spectra (B) of Ni K-edge for NiCat sample electrodeposited on ITO coated on polyethylene terephthalate sheets at 1.15 V vs.NHE in Bi buffer (pH 9.2). X-ray fluorescence data were collected while 0.40, 1.10, and 1.80 V vs. NHE were applied to the NiCat sample. The thick lines are the experimental data and the thin red lines are the simulation results. The simulation parameters are provided in Table 6.2.

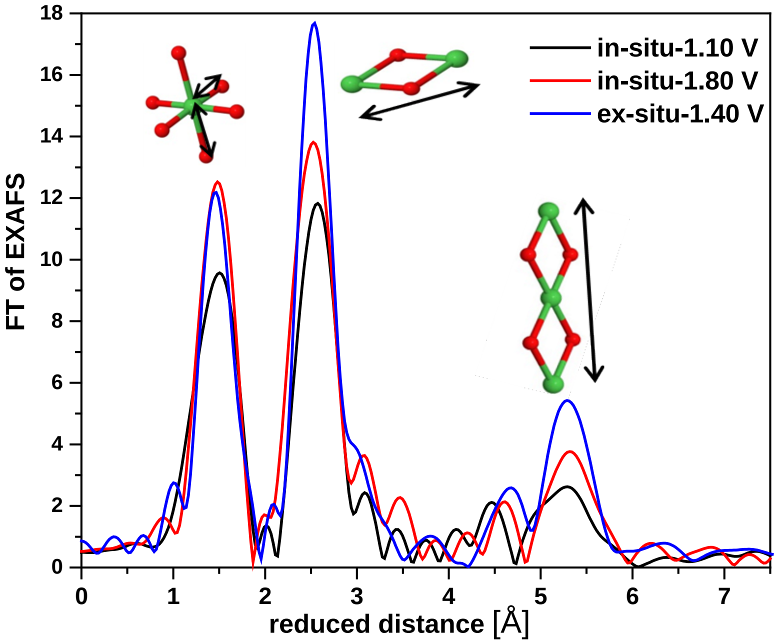

Figure 6.7. Fourier-transform of EXAFS spectra of Ni K-edge for in-situ NiCat samples operated at 1.10 V and 1.80 V vs. NHE and ex-situ operated sample for 48 hours at 1.40 in borate buffer (0.1 M, pH 9.2). Color codes are the following: nickel, green; and oxygen, red.

Table 6.2. Parameters obtained by simulation of the k^3-weighted EXAFS spectra. The simulated spectra correspond to the Fourier-transformed EXAFS spectra shown in Fig. 6.6 (N: coordination number; R: absorber-backscatter distance). The number in parentheses corresponds to the errors representing 68% confidence intervals of the respective fit parameters. To avoid over-parameterization, the Debye-Waller parameter for oxygen shells and Ni shells were fixed to 0.032 and 0.087 Å, respectively. The amplitude reduction factor, S_0^2, was fixed to 0.90 as suggested by simulations. Errors are represented in parentheses.

Type of bond	**0.40 V vs. NHE**		**1.10 V vs. NHE**		**1.80 V vs. NHE**	
	R [Å]	**N**	**R [Å]**	**N**	**R [Å]**	**N**
Ni-O$_{short}$	1.95 (0.01)	2.7 (0.3)	1.81 (0.01)	2.4 (0.4)	1.85 (0.01)	3.9 (0.6)
Ni-O$_{long}$	2.09 (0.01)	4.0 (0.3)	1.93 (0.01)	3.1 (0.4)	1.95 (0.02)	1.8 (0.5)
Ni-Ni$_{short}$	3.07 (0.01)	6.3 (0.4)	2.61 (0.01)	1.4 (0.5)	2.82 (0.01)	11.4 (0.5)
Ni-Ni$_{long}$	3.50 (0.02)	1.7 (0.5)	2.82 (0.01)	9.6 (0.6)	3.07 (0.01)	3.9 (0.6)

To study the dynamics of the oxidation state changes, cyclic voltammetry (44 CVs) experiments (0.25 – 1.45 V vs. NHE) with simultaneously recorded fluorescence data of NiCat (ITO on Mylar, Bi 0.1 M, pH 9.2) were performed. The X-ray energy beam was fixed to the middle of the nickel edge (8345 eV). The changes in the fluorescence are related to changes in the oxidation state. Figure 6.8-A shows XANES spectra of the NiCat at reductive (0.45 V) and oxidative (1.45 V) potential. These XANES spectra are neither background subtracted nor normalized in order to relate the fluorescence changes in the CV to Ni edge changes. The red dotted line represents the energy at which the X-ray was set (8345 eV). An oxidation of Ni during the CV results in a shift of the edge position to higher energy as illustrated by the blue arrow in the inset. This fact, in turn, causes a decrease in the fluorescence intensity as illustrated by the red arrow in the inset. An increase in the oxidation state is then reflected as a decrease in the fluorescence and vice versa.

The averaged changes in the fluorescence during 44 CVs are shown in Figure 6.8-B. When the potential increases, the amount of fluorescence decreases, meaning that the NiCat is first getting more oxidized and then it is increased to the same level as the film is reduced in the backward scan (signaled by the arrows). During the potential interval selected for the CV, the overall fluorescence changes correspond to about 1.8 eV in the middle of the edge in the non-normalized data.

The actual edge shift (estimated with the integral method) and change in oxidation state after normalization correspond to 2.7 eV (Figure 6.5). In this case, we observed a change in oxidation state from almost $\mathrm{Ni^{II}}$ to $\mathrm{Ni^{IV}}$. The oxidation state changes obtained by CV experiment is smaller compared to the one in Figure 6.5. By following the time course of the reduction behavior of the NiCat (Figure 6.9), we observed that during operation, nickel ions could be trapped in high oxidation states because the low oxidations state can only be recovered after operation at reductive potentials (>25 min reduction). However, the oxidation state changes observed during a CV on a NiCat account for 1 unit in terms of oxidation state changes. The majority of the oxidation state changes when scanning the CV in the anodic (positive) direction happen between 1.0 V and 1.20 V in a quite narrow potential range. Higher than 1.20 V vs. NHE oxygen evolution is happening without further oxidation of the Ni ions. As the X-ray fluorescence signal reflects the oxidation state, consequently the first derivative of the fluorescence represents a current that can be assigned to the reduction of the metal centers given by equation (6.1).

$$\int I dt = Q_{ox} + Q_{O_2} \qquad (6.1)$$

Where Q_{ox} and Q_{O_2} are charges corresponding to changes in oxidation state and water splitting, respectively. At the reduction potential Q_{O_2} is zero and Q_{ox} is proportional to changes in oxidation state, which can be associated to changes in fluorescence:

$$fluorescence \sim \int I\, dt \qquad (6.2)$$

Therefore, the first derivative of the fluorescence represents the reduction current.

If the derivative of fluorescence is scaled to the current density in the CV, they match very closely the reductive wave of the CV (Figures 6.8 and 6.10). It is also possible to resolve the oxidative wave from the catalytic wave. This data suggests that the redox waves observed in the CV are mostly related to redox and structural changes centered in the Ni metal and not to redox changes in other species (no formation of peroxides or superoxides for example). As Figure 6.10 shows the maximum current, which corresponds to oxidation of nickel atoms (derivative of the fluorescence) is at 1.18 V vs. NHE and at 1.27 V the oxidation process is finished, meaning that the current at high potential than 1.27 V corresponds to water splitting. At 0.67 V the maximum reduction current (derivative of the fluorescence) was observed and the reduction process was finished at 0.38 v vs. NHE.

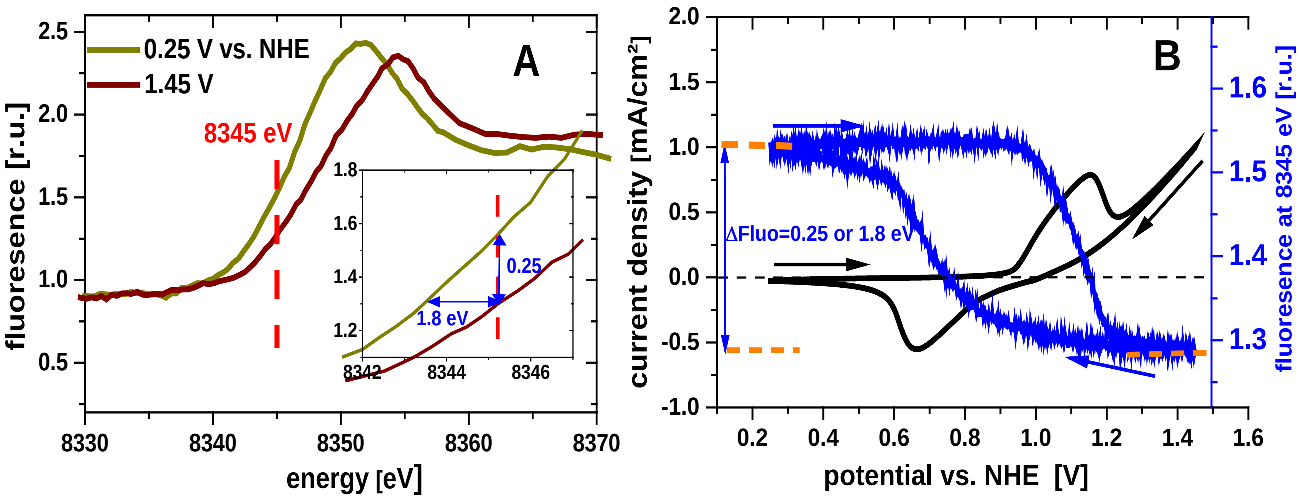

Figure 6.8. (A) In-situ nickel *K*-edge XANES spectra (without normalization) of NiCat samples operated at 0.25 and 1.45 V vs. NHE in 0.1 M B_i, pH 9.2. The deposited charge was 75 mC/cm^2 on carbon paper. The red dotted line marks the energy of 8345 eV, which was selected for monitoring the fluorescence during CV scans. The inset shows the change in the XANES spectra around 8345 eV: **(A)** Fluorescence change of 0.25 units corresponds to a change of 1.8 eV when increasing the potential from 0.25 V to 1.45 V vs. NHE.

(B) The CV of NiCat in 0.1 M B_i, pH 9.2 with a scan rate of 20 mV/s (black line). At the same time, the X-ray fluorescence was detected, which is shown as an average of 44 CV scans. The arrows indicate the scan direction. The decrease in the fluorescence (0.25 units) is related to a shift of 1.8 eV in the edge position.

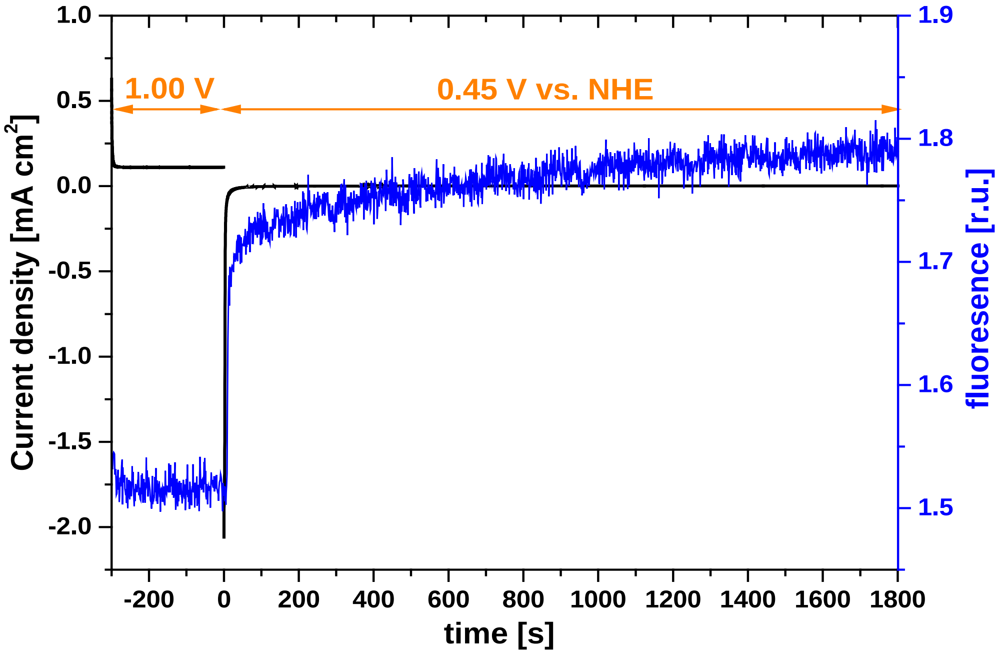

Figure 6.9. Ni *K*-edge fluorescence data when jumping from 1.00 V vs. NHE to 0.45 V vs. NHE of a NiCat electrode (deposited for 75 mC/cm^2 on carbon paper) in 0.1 M B_i, pH 9.2 compared to respective current densities. The X-ray energy was kept constant at 8345 eV.

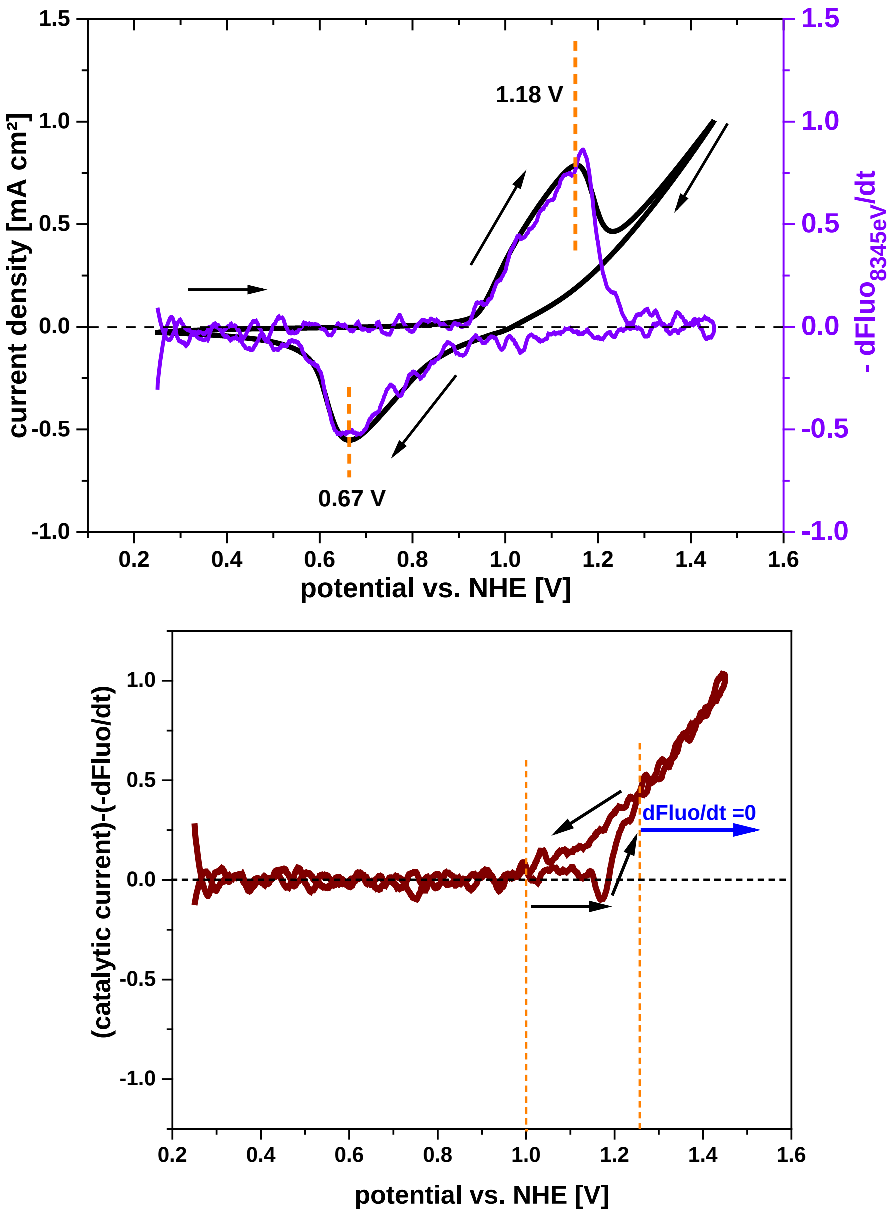

Figure 6.10. In-situ X-ray absorption cyclic voltammetry in 1 M B_i for the NiCat deposited for 75 mC cm^{-2} on carbon paper. The current density is given by the black line. The scan rate of the CV was 20 mVs^{-1}. The red line shows the derivative of the fluorescence in time which is related to the oxidation state changes or the corresponding structural changes. The derivative was calculated from the corresponding Ni *K*-edge fluorescence data at 8345 eV of Figure 6.8 -B.

To provide evidence for changes in the redox kinetics of the NiCat, time-resolved experiments were conducted in which the potential was switched between 1.30 V and 0.45 V versus NHE in 10-second pulses. To track changes in the oxidation state the X-ray fluorescence was recorded at fixed energy, such that this energy is approximately at the middle of the edge position of NiCat (8345 eV). The current and fluorescence for the jump potential were measured simultaneously for 29 repetitions and the averaged results are shown in Figure 6.11. Changes in the fluorescence are directly related to changes in the oxidation state of the metal (Figure 4.7). According to equation (6.2), these changes can be compared to the integral of the current that represents the charge associated with the redox and catalytic process combined (Figure 6.11).

When the potential is switched to a low reductive potential (0.45 V vs. NHE) the rise of fluorescence follows perfectly the integral of the current. As Figure 6.9-B shows, the reduction process first has a fast domain (3 seconds) and then a slower domain. However, the reduction process does not finish within 10 seconds, but gradually rises which means that not all nickel atoms are fully reduced (see as well as Figure 6.9 for comparison). When the potential is switched to catalytic potential (1.45 V vs. NHE) the integral of the current shows a linear behavior in the first 4 seconds only. After 4 seconds the fluorescence amplitude is constant which means that all nickel sites are completely oxidized after this time. After oxidizing some Ni species, water oxidation is possible which leads to an increase in the charge due to the catalytic current. The increase of this charge follows a Faradic linear behavior with time. This behavior indicates that it is strongly affected by the catalytic current. The total change in the nickel fluorescence corresponds to about 0.09 eV, which is less than the changes previously observed in Figure 6.8. However, it is clear from the measurements that after 10 s the reduction process of nickel has not been completed yet. It might be that the redox-processes of the NiCat are mainly dominated by the resistance.

The decay/rise fluorescence data could not be simulated with a sum of linear/exponential or several exponentials (parallel reactions). We simulated the linear parts with the slope to get the rate of oxidation/reduction (slope is in fluorescence units per second).Then the slope was divided by the total amplitude of fluorescence changes to get the rate of oxidation/reduction.

$$F = F_0 + A*t \qquad (6.3)$$

F and t represent the fluorescence and the time in seconds, respectively. F_0 corresponds to an offset. The results from the fittings are shown in Table 6.3.

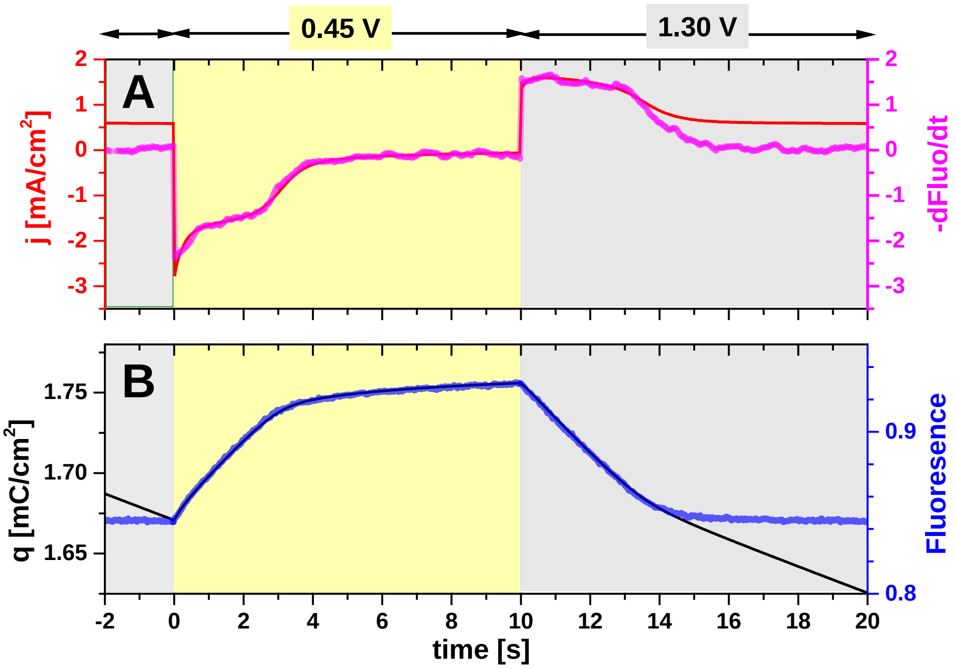

Figure 6.11. In-situ X-ray absorption chronoamperometric step experiment in 1 M B$_i$ for the NiCat deposited for 75 mC/cm^2 on carbon paper. The result corresponds to the average of 29 potential steps. The monochromatic X-ray energy was held at 8345 eV. **(A)** Current density (red line) and negative derivative of fluorescence (magenta line) of 10 s potential jumps between 0.45 V vs. NHE and 1.30 V vs. NHE. **(B)** Charge density (black line) and fluorescence (blue line) of 10 s potential jumps between 0.45 V vs. NHE and 1.30 V vs. NHE.

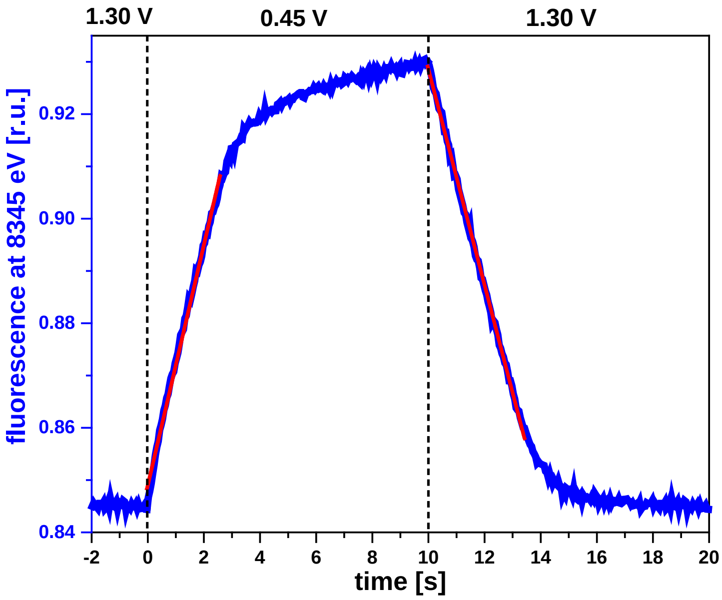

Figure 6.12. Fitted time course fluorescence data of an in-situ X-ray absorption chronoamperometric step experiment of 10 s potential jumps between 0.45 V vs. NHE and 1.30 V vs. NHE in 1 M Bi for the NiCat deposited for 75 mCcm^{-2} on carbon paper. The fluorescence data corresponds to the average of 29 potential steps. The monochromatic X-ray energy was held at 8345 eV.

Table 6.3. Simulation parameters for the fitting of the linear part of the time courses of the fluorescence of jump potential between 0.45 V and 1.30 V versus NHE from Figure 6.12. X-ray energy was fixed at 8345 eV. The number in parenthesis corresponds to the uncertainty in the last digit. Data were fit to the equation: $F = F_0 + A*t$

Parameter	**Ni reduction**	**Ni oxidation**
F_0	0.8490 (4E-4)	0.9292 (2E-4)
A	0.0230 (2E-4)	-0.0207 (1E-4)
R-Square	0.9942	0.9987
Total amplitude	0.085	0.085
A / Total amplitude	0.27	0.24

6.3 Summary

- X-ray absorption spectroscopy analysis of NiCat samples operated at non-catalytic and catalytic potentials indicate both pronounced oxidation state and atomic structural changes in response to applied electrode potentials. In contrast for CoCat, long time operation has a relatively minor effect in the Co coordination and its structure, in general.
- Exposure of NiCat to 0.90 V for 24 h results in a severe shift of the edge position (by 0.9 eV) towards higher energies. This energy difference of 0.9 eV corresponds to a nickel oxidation state of +2.3 for the steady state film and +2.8 for the 24 h operated film. The difference between the NiCat at 1.45 V and the one operated for 24 h at 1.40 V corresponds to a change in integral edge position of 1.1 eV, in other words, nickel oxidation states of +3.0 at 1.45 V and +3.7 for the film operated for 24 h at 1.40 V
- The minimum catalytic activity at operation for 11 hours at non-catalytic potentials (0.8 and 0.9 V vs. NHE) is related to a rather ordered amorphous nickel-oxide. However, after 48 hours operation the catalyst gets more disordered, and the initial Ni-O and Ni-Ni distances are split caused by distortion of the NiO_6 octahedral. On the other hand, operation at catalytic potential (1.4 V vs. NHE) induces a structure similar to γ-NiOOH, which is majorly stable over electrolysis time. These results highlight that long term operation at different electrochemical potentials can induce different nickel-oxide phases, where the most ordered γ-NiOOH phase does not present the most active phase.

- *In-situ* measurement shows that the derivative of the X-ray fluorescence data collected during a CV match very closely the reductive wave of the CV, meaning that the current is mostly related to redox and structural changes of the Ni metal centers and not to changes in other species (no formation of peroxides or superoxides, for example).
- Furthermore, the *in-situ* measurement shows that after 4 seconds operation at 1.3 V, all nickel sites are completely oxidized, however, the reduction process of nickel at 0.7 v vs. NHE has not been completed after 10 s, but continuous for tens of minutes.

Chapter 7

Stability and self-healing of NiFe catalyst

Recently, NiFe oxyhydroxides turned out to be among the most promising electrocatalysts for efficient alkaline water oxidation (Louie and Bell 2013, Görlin, Gliech et al. 2015, Wang, Geng et al. 2015, Gorlin, Chernev et al. 2016). NiFe-oxides catalysts (NiFeCat) have been prepared by several methods: electrodeposition from aqueous solutions, anodically (McCrory, Jung et al. 2013) and cathodically (González-Flores, Klingan et al. 2018) and electrochemical surface oxidation of steels with reasonable long term stability (Schäfer, Sadaf et al. 2015, Loos, Zaharieva et al. 2019).

We prepared NiFeCat by an easy and fast method. In this method, the catalyst was generated from NiFe alloys by several fast cycling CVs (150 mVs^{-1}) in the potential range from -0.4 to 1.8 V vs. RHE in 1 M KOH. After catalyst formation, NiFeCat was operated in different solutions at non-catalytic and catalytic electrode potentials, and after every 30 minutes of chronoamperometry, CVs were recorded in order to diagnose losses in redox-active nickel ions and catalytic activity.

Electrochemical experiments show that NiFeCat is not stable at KPi (0.1 M, pH 7) and 0.1 M KOH as 50 % of the catalytic current is lost after two days of operation.

Operation at catalytic potentials in 1 M KOH is a self-healing process and at least 80 % of catalytic current remained.

Portions of this chapter have been prepared for publication.

7.1. Experimental Section

7.1.1 Materials

Reagents: NiFe alloy ($Fe_{0.64}$ $Ni_{0.36}$, Invar, Goodfellow GmbH, ≥99.0%, 0.25 mm); KOH (Sigma Aldrich, ≥86%), H_2KPO_4 (Roth, ≥99%), K_2HPO_4 (Roth, ≥99%).

All reagents were used without further purification. Solutions were prepared with 18.2 MΩ·cm Milli-Q water.

7.1.2 Formation of NiFe Catalyst

All potentials are given relative to the potential of a normal hydrogen electrode (NHE).

KOH (1 M) solution was prepared from purified and deionized water mentioned above.

Electrochemical cycling and electrochemical analyses were performed using a Gamry potentiostat (Gamry Interface 1000^{TM}, Warminster, USA) with 8 potentiostats, having in total 10 channels (10 simultaneous experiments), and each one in a three-electrode single compartment setup.

The working electrodes ($Fe_{0.64}$ $Ni_{0.36}$ alloy) have been cleaned with Ethanol and MilliQ water. A platinum mesh (25×25 mm^2) served as a counter electrode and an RHE electrode (HydroFlex®, Gaskatel) as a reference electrode. The back side of the NiFe electrodes was covered with Kapton tape (IM301202 polyimid film Goodfellow, 683-465-79), which is stable during catalyst formation but not for long time operation.

The cell geometry was roughly the same for all the following electrochemical characterizations (distance between working and reference electrode ~0.5 cm). Active IR-drop compensation is not possible to conduct with this potentiostat so for both, electrochemical cycling and operation, no IR-compensation was performed. The uncompensated resistance (R_u) was very low (1-1.5 **Ω**), therefore the potential difference between the nominal and the iR-corrected potential was small.

The catalyst was generated by 200 cycles of fast electrochemical cycling (150 mVs^{-1}) in the potential range from -0.4 to 1.8 V vs. RHE in 1 M KOH (75 mL, pH 13.85). The starting and stopping point of the cycling was 1.0 V vs. RHE.

7.1.3 Electrochemical Characterization

After formation of nickel-iron catalyst, it was operated in the following solutions:

a) The same KOH than for catalyst formation (1M, pH 13.85)
b) Fresh KOH, 1M, pH 13.85
c) KOH, 0.1 M, pH 12.85
d) KPi, 0.1 M, pH 7 (approximately 40% KH_2PO_4 and 60% K_2HPO_4)

Counter and reference electrode were cleaned with 30% nitric acid and MilliQ water (18.2 MΩ) except when the same KOH was used for formation and operation catalyst. Then NiFeCat was operated for two days at several selected catalytic and non-catalytic potentials. Cyclic voltammograms (1 - 1.6 V vs. RHE) with scan rate of 20 mVs^{-1} were run every 30 minutes in order to diagnose losses in redox-active nickel-iron ions and catalytic activity. The second of two scans was analyzed.

7.2 Results and discussion

After electrodeposition, the catalytic current and the redox-active NiFe ions of the initial CV of all samples were not completely the same so all data were normalized to the data of initial CV.

7.2.1 The same KOH for catalyst formation and operation

Figure 7.1 shows the normalized redox-active NiFe ions and the catalytic current of the films operated at non-catalytic (0.33-0.86 V vs. NHE) and catalytic electrode potentials (71- 0.86 V vs. NHE) for 48 hours in KOH (1 M, pH 13.85). The results show that the number of redox-active NiFe atoms is increased during operation for all potentials. The slope of increasing for catalytic potentials (≥ 0.66 V) during initial 4 hours operation is higher than the rest time of operation, however, for non-catalytic potentials the redox charge gradually increased by about 20 % after 48 hours operation.

The catalytic current fluctuates during operation. It is decreased during the initial half-day operation and then increased for about 12 hours. After that, it is decreased and at the end of operation, more than 80 % of the initial amount remains. The fluctuation of the catalytic current could be related to temperature changing of the lab during day and night.

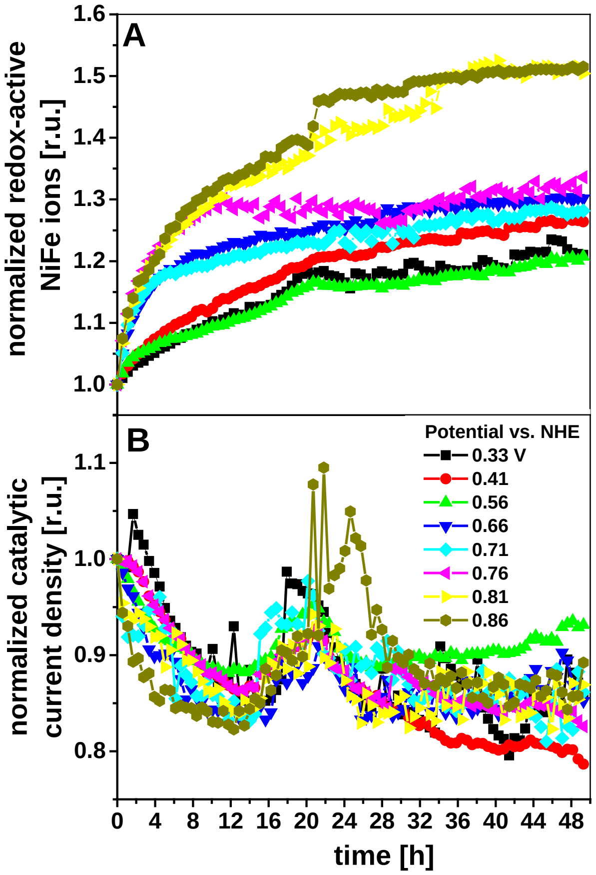

Figure 7.1. Water oxidizing nickel–iron oxide film operated in the same KOH for formation catalyst (1 M, pH 13.85). The amount of redox-active Ni ions **(A)** and the catalytic current **(B)** determined by the integration of negative cathodic CV scan during operation of nickel-oxide films at indicated potentials (0.18 - 0.78 V vs NHE) and the maximum point of CV over the course of two days. Every 30 minutes of chronoamperometry CVs are recorded and the second of two scans with a scan rate of 20 mV s^{-1} was analyzed. The data were normalized to the initial CVs. The mean value of the redox-charge and the catalytic current density of the initial CV of all samples were about 18 mC/cm^2 and 58 mA/cm^2, respectively.

7.2.2 Operation in KOH (pH 13.85, 1 M) – Fresh KOH for operation

After NiFe catalyst formation, we exchanged the KOH to the fresh one (1 M, pH 13.85) and samples were operated for one week. We followed the protocol above described (section 7.1.3) and the time course of the redox-active NiFe ions and the catalytic current of the films were extracted from CV are shown in Figure 7.2.

The results show that the negative area of CV which corresponds to the redox-active NiFe atoms is increased during operation if NiFeCat is operated at catalytic potentials (≥ 0.56 V vs. NHE). Figure 7.2-A shows an unexpected drastic drop in the redox charge during operation, meaning that we could not find any scientific reason for that.

The catalytic current fluctuates a lot during operation, however, after one-week operation it is higher than the initial amount or remains at least 80 % if NiFe is operated at catalytic potentials.

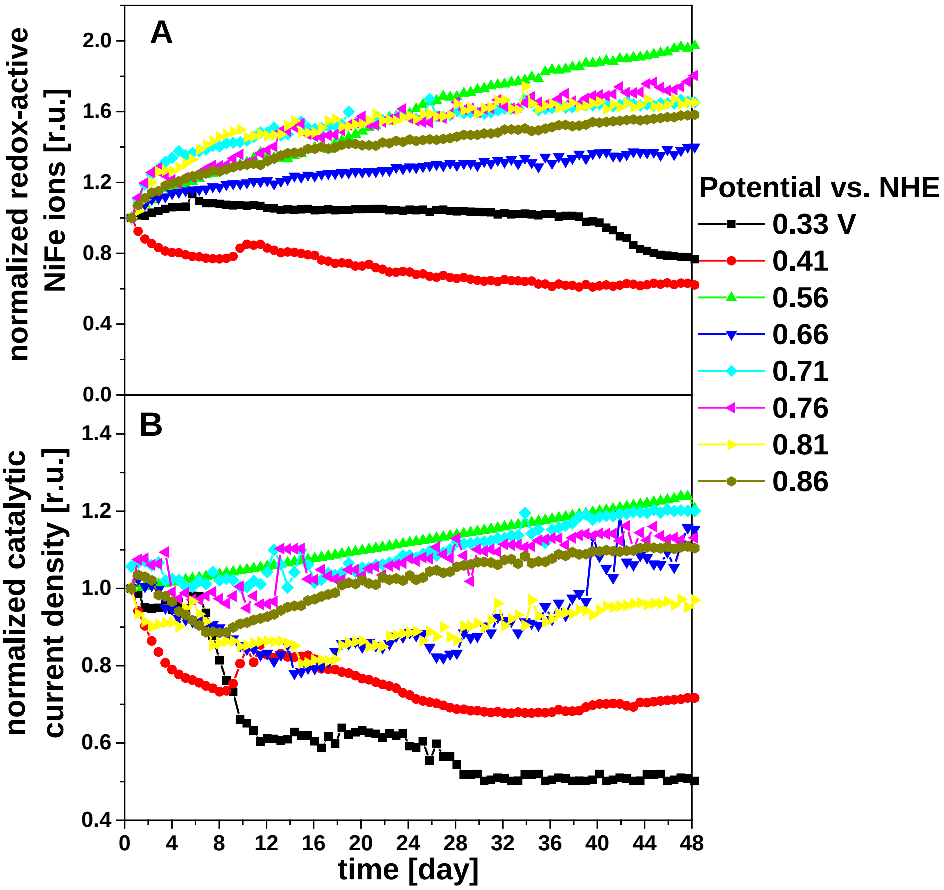

Figure 7.2. Water oxidizing nickel–iron oxide film operated in fresh KOH for formation catalyst (1 M, pH 13.85), meaning that after catalyst formation the KOH was exchanged to the new one. The amount of redox-active Ni ions **(A)** and the catalytic current **(B)** determined by the integration of negative cathodic CV scan during operation of nickel-oxide films at indicated potentials (0.18 - 0.78 V vs NHE) and the maximum point of CV over the course of two days. Every 30 minutes of chronoamperometry CVs are recorded and the second of two scans with a scan rate of 20 mV s^{-1} was analyzed. The data were normalized to the initial CVs. The mean value of the redox-charge and the catalytic current density of the initial CV of all samples were about 17 mC/cm^2 and 64 mA/cm^2, respectively.

7.2.3 Operation in 0.1 M KOH (pH 12.85)

Figure 7.3 shows the normalized redox-active NiFe ions and the catalytic current of the films operated at non-catalytic (0.4 - 0.72 V vs. NHE) and catalytic electrode potentials (0.77 - 0.92

V vs. NHE) for 48 hours in KOH (0.1 M, pH 12.85). When NiFe catalyst is operated at 0.47 V vs. NHE or lower the redox-active sites linearly decreased. However once the catalyst is operated at higher potentials during the initial 4 hours operation, the redox charge is increased and then it is almost stable for one day and after that, it is decreased. On the other hand, the catalytic current is decreased during operation for all potentials and after two days of operation, more than 50% is lost. Therefore, self-healing process is not possible at these conditions.

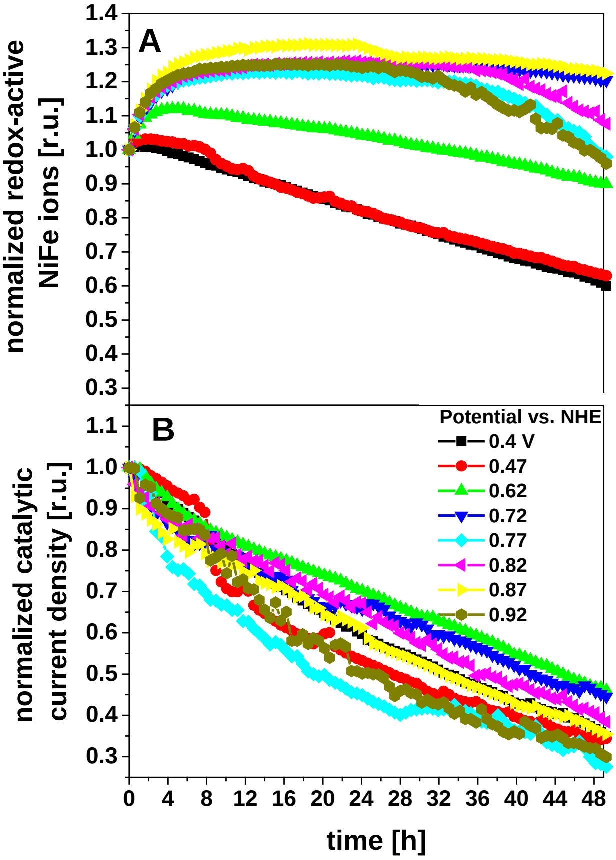

Figure 7.3. Water oxidizing nickel–iron oxide film operated in KOH (0.1 M, pH 12.85). The amount of redox-active Ni ions **(A)** and the catalytic current **(B)** determined by the integration of negative cathodic CV scan during operation of nickel-oxide films at indicated potentials (0.24 - 0.84 V vs NHE) and the maximum point of CV over the course of one week. Every 30 minutes of chronoamperometry CVs are recorded and the second of two scans with a scan rate of 20 mV s^{-1} was analyzed. The data were normalized to the initial CVs. The mean value of the redox-charge and the catalytic current density of the initial CV of all samples were about 13 mC/cm^2 and 12 mA/cm^2, respectively.

7.2.4 Operation in KPi (pH 7, 0.1 M)

Figure 7.4 shows the normalized redox-active NiFe ions and the catalytic current of the films operated at non-catalytic and catalytic electrode potentials for 48 hours in KPi (0.1 M, pH 7; more details are in chapter 2, section 2.1.2). The redox-charge (A) and the catalytic current (B) show that both are logarithmically reduced and after 48 hours, they do not reach a steady state.

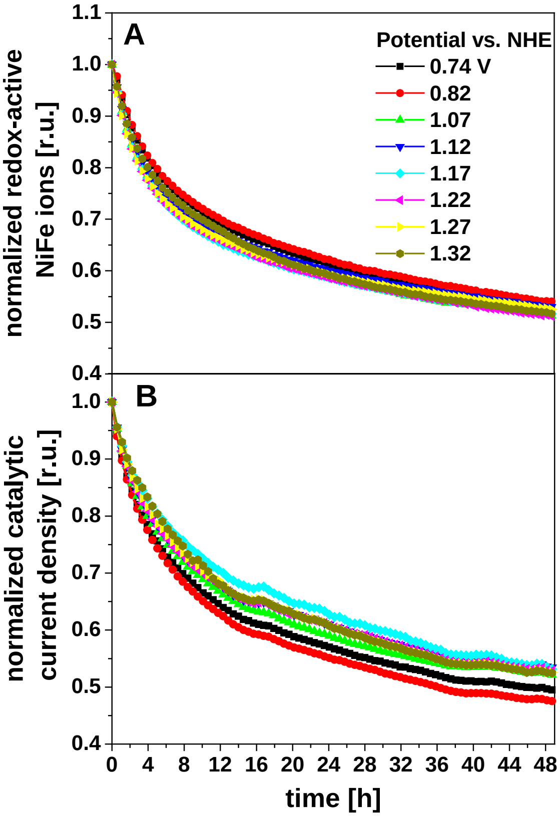

Figure 7.4. Water oxidizing nickel–iron oxide film operated in KPi (0.1 M, pH 7). The amount of redox-active Ni ions **(A)** and the catalytic current **(B)** determined by the integration of negative cathodic CV scan during operation of nickel-oxide films at indicated potentials (0.59 – 1.19 V vs NHE) and the maximum point of CV over the course of one week. Every 30 minutes of chronoamperometry CVs are recorded and the second of two scans with a scan rate of 20 mV s^{-1} was analyzed. The data were normalized to the initial CVs. The mean value of the redox-charge and the catalytic current density of the initial CV of all samples were about 19 mC/cm^2 and 6 mA/cm^2, respectively.

7.3 Summary

- Obtaining a NiFe-oxide from $Fe_{0.64}Ni_{0.36}$ alloy by cyclic voltammograms in 1 M KOH is an easy and fast method to convert NiFe alloy into an electrocatalyst with very good catalytic activity. NiFeCat is not stable at KPi (0.1 M, pH 7) and 0.1 M KOH as 50 % of the catalytic current is lost after two days operation. However, operation at catalytic potentials in 1 M KOH is a self-healing process as the catalytic current is higher than the initial amount or at least 80 % left (depends on the potential) after one-week operation.
- After two days operation, the catalytic current of NiFeCat operated in fresh 1M KOH is higher than the sample was operated in the same solution for formation catalyst.

References

Amendola, V. and M. Meneghetti (2009). "Laser ablation synthesis in solution and size manipulation of noble metal nanoparticles." Physical chemistry chemical physics **11**(20): 3805-3821.

Amendola, V. and M. Meneghetti (2009). "Self-healing at the nanoscale." Nanoscale **1**(1): 74-88.

Amendola, V. and M. Meneghetti (2011). Self-healing at the nanoscale: mechanisms and key concepts of natural and artificial systems, CRC Press.

Ankudinov, A. L., B. Ravel, J. J. Rehr and S. D. Conradson (1998). "Real-space multiple-scattering calculation and interpretation of X-ray-absorption near-edge structure." Physical Review B: Condensed Matter **58**(12): 7565-7576.

Appleby, A., G. Crepy and J. Jacquelin (1978). "High efficiency water electrolysis in alkaline solution." International Journal of Hydrogen Energy **3**(1): 21-37.

Aro, E. M., I. Virgin and B. Andersson (1993). "Photoinhibition of Photosystem II. Inactivation, protein damage and turnover." Biochimica et Biophysica Acta **1143**(2): 113-134.

Barwe, S., J. Masa, C. Andronescu, B. Mei, W. Schuhmann and E. Ventosa (2017). Overcoming the instability of nanoparticle based catalyst films in alkaline electrolysers by self-assembling and self-healing films.

Bediako, D. K., C. Costentin, E. C. Jones, D. G. Nocera and J.-M. Savéant (2013). "Proton–Electron Transport and Transfer in Electrocatalytic Films. Application to a Cobalt-Based O2-Evolution Catalyst." Journal of the American Chemical Society **135**(28): 10492-10502.

Bediako, D. K., Y. Surendranath and D. G. Nocera (2013). "Mechanistic studies of the oxygen evolution reaction mediated by a nickel-borate thin film electrocatalyst." J Am Chem Soc **135**(9): 3662-3674.

Brodsky, C. N., R. G. Hadt, D. Hayes, B. J. Reinhart, N. Li, L. X. Chen and D. G. Nocera (2017). "In situ characterization of cofacial Co (IV) centers in Co4O4 cubane: Modeling the high-valent active site in oxygen-evolving catalysts." Proceedings of the National Academy of Sciences **114**(15): 3855-3860.

Corrigan, D. A. (1987). "The catalysis of the oxygen evolution reaction by iron impurities in thin film nickel oxide electrodes." Journal of The Electrochemical Society **134**(2): 377-384.

Costentin, C. and D. G. Nocera (2017). "Self-healing catalysis in water." Proceedings of the National Academy of Sciences **114**(51): 13380-13384.

Dincă, M., Y. Surendranath and D. G. Nocera (2010). "Nickel-borate oxygen-evolving catalyst that functions under benign conditions." Proceedings of the National Academy of Sciences **107**(23): 10337-10341.

Dincă, M., Y. Surendranath and D. G. Nocera (2010). "Nickel-borate oxygen-evolving catalyst that functions under benign conditions." Proceedings of the National Academy of Sciences, USA **107**(23): 10337-10341.

Dittmer, J. (1999). Linear-Dichroismus-Röntgenabsorptionsspektroskopie zum katalytischen Zyklus des wasserspaltenden Mangankomplexes der Photosynthese in Theorie und Experiment Ph.D., Christian-Albrechts-Universität.

Du, P. W., O. Kokhan, K. W. Chapman, P. J. Chupas and D. M. Tiede (2012). "Elucidating the domain structure of the cobalt oxide water splitting catalyst by X-ray pair distribution function analysis." Journal of the American Chemical Society **134**(27): 11096-11099.

Farrow, C. L., D. K. Bediako, Y. Surendranath, D. G. Nocera and S. J. L. Billinge (2013). "Intermediate-Range Structure of Self-Assembled Cobalt-Based Oxygen-Evolving Catalyst." Journal of the American Chemical Society **135**(17): 6403-6406.

Fedrizzi, L., W. Fürbeth and F. Montemor (2011). Self-healing Properties of New Surface Treatments (EFC 58), Institute of Materials. Minerals and Mining.

Gao, M., W. Sheng, Z. Zhuang, Q. Fang, S. Gu, J. Jiang and Y. Yan (2014). "Efficient water oxidation using nanostructured α-nickel-hydroxide as an electrocatalyst." Journal of the American Chemical Society **136**(19): 7077-7084.

Ghosh, S. K. (2009). Self-healing materials: fundamentals, design strategies, and applications, John Wiley & Sons.

Glikman, S. and I. S. Shcheglova (1968). "Catalytic water oxidation by ions of four-valent cerium [In Russ]." Kinetika i Kataliz **9**.

González-Flores, D., K. Klingan, P. Chernev, S. Loos, M. R. Mohammadi, C. Pasquini, P. Kubella, I. Zaharieva, R. D. L. Smith and H. Dau (2018). "Nickel-iron catalysts for electrochemical water oxidation – redox synergism investigated by in situ X-ray spectroscopy with millisecond time resolution." Sustainable Energy & Fuels **2**(9): 1986-1994.

Gorlin, M., P. Chernev, J. Ferreira de Araujo, T. Reier, S. Dresp, B. Paul, R. Krahnert, H. Dau and P. Strasser (2016). "Oxygen Evolution Reaction Dynamics, Faradaic Charge Efficiency, and the Active Metal Redox States of Ni-Fe Oxide Water Splitting Electrocatalysts." J Am Chem Soc **138**(17): 5603-5614.

Görlin, M., M. Gliech, J. Ferreira de Araújo, S. Dresp, A. Bergmann and P. Strasser (2015). Dynamical changes of a Ni-Fe oxide water splitting catalyst investigated at different pH.

Hall, D. (1983). "Ni (OH) 2-Impregnated Anodes for Alkaline Water Electrolysis." Journal of The Electrochemical Society **130**(2): 317-321.

Halpert, G. (1984). "Past developments and the future of nickel electrode cell technology." Journal of power sources **12**: 177-192.

Haumann, M., A. Porthun, T. Buhrke, P. Liebisch, W. Meyer-Klaucke, B. Friedrich and H. Dau (2003). "Hydrogen-induced structural changes at the nickel site of the regulatory NiFe hydrogenase from Ralstonia eutropha detected by X-ray absorption spectroscopy (vol 42, pg 11004, 2003)." Biochemistry **42**(46): 13786-13786.

Hill, C. L. and X. Zhang (1995). "A'smart'catalyst that self-assembles under turnover conditions." Nature **373**(6512): 324.

Hocking, R. K., R. Brimblecombe, L.-Y. Chang, A. Singh, M. H. Cheah, C. Glover, W. H. Casey and L. Spiccia (2011). "Water-oxidation catalysis by manganese in a geochemical-like cycle." Nature Chemistry **3**(6): 461-466.

Huynh, M., D. K. Bediako and D. G. Nocera (2014). "A functionally stable manganese oxide oxygen evolution catalyst in acid." Journal of the American Chemical Society **136**(16): 6002-6010.

Huynh, M., C. Shi, S. J. Billinge and D. G. Nocera (2015). "Nature of Activated Manganese Oxide for Oxygen Evolution." J Am Chem Soc **137**(47): 14887-14904.

Jiang, S., Y. Chen, J. You, T. Chen and A. Tseung (1990). "Reactive Deposition of Cobalt Electrodes I. Experimental." Journal of The Electrochemical Society **137**(11): 3374-3380.

Jiang, S. and A. Tseung (1991). "Reactive Deposition of Cobalt Electrodes IV. Alkaline Water Electrolysis." Journal of The Electrochemical Society **138**(5): 1216-1222.

Kanan, M. W. and D. G. Nocera (2008). "In situ formation of an oxygen-evolving catalyst in neutral water containing phosphate and Co^{2+}." Science **321**(5892): 1072-1075.

Kanan, M. W., J. Yano, Y. Surendranath, M. Dinca, V. K. Yachandra and D. G. Nocera (2010). "Structure and valency of a cobalt− phosphate water oxidation catalyst determined by in situ X-ray spectroscopy." Journal of the American Chemical Society **132**(39): 13692-13701.

Klingan, K., F. Ringleb, I. Zaharieva, J. Heidkamp, P. Chernev, D. Gonzalez-Flores, M. Risch, A. Fischer and H. Dau (2014). "Water oxidation by amorphous cobalt-based oxides: Volume activity and proton transfer to electrolyte bases." ChemSusChem **7**(5): 1301–1310.

Lee, S. W., C. Carlton, M. Risch, Y. Surendranath, S. Chen, S. Furutsuki, A. Yamada, D. G. Nocera and Y. Shao-Horn (2012). "The nature of lithium battery materials under oxygen evolution reaction conditions." Journal of the American Chemical Society **134**(41): 16959-16962.

Li, X., F. C. Walsh and D. Pletcher (2011). "Nickel based electrocatalysts for oxygen evolution in high current density, alkaline water electrolysers." Physical Chemistry Chemical Physics **13**(3): 1162-1167.

Loos, S., I. Zaharieva, P. Chernev, A. Lißner and H. Dau (2019). Electromodified NiFe Alloys as Electrocatalysts for Water Oxidation: Mechanistic Implications of Time-Resolved UV/Vis Tracking of Oxidation State Changes.

Louie, M. W. and A. T. Bell (2013). "An investigation of thin-film Ni–Fe oxide catalysts for the electrochemical evolution of oxygen." Journal of the American Chemical Society **135**(33): 12329-12337.

Lutterman, D. A., Y. Surendranath and D. G. Nocera (2009). "A self-healing oxygen-evolving catalyst." Journal of the American Chemical Society **131**(11): 3838-3839.

McAlpin, J. G., Y. Surendranath, M. Dinca, T. A. Stich, S. A. Stoian, W. H. Casey, D. G. Nocera and R. D. Britt (2010). "EPR evidence for Co (IV) species produced during water oxidation at neutral pH." Journal of the American Chemical Society **132**(20): 6882-6883.

McCrory, C. C. L., S. Jung, J. C. Peters and T. F. Jaramillo (2013). "Benchmarking heterogeneous electrocatalysts for the oxygen evolution reaction." Journal of the American Chemical Society **135**(45): 16977-16987.

Merrill, M. D. and R. C. Dougherty (2008). "Metal oxide catalysts for the evolution of O2 from H2O." The Journal of Physical Chemistry C **112**(10): 3655-3666.

Morita, M., C. Iwakura and H. Tamura (1977). "The anodic characteristics of manganese dioxide electrodes prepared by thermal decomposition of manganese nitrate." Electrochimica Acta **22**(4): 325-328.

Morita, M., C. Iwakura and H. Tamura (1979). "The anodic characteristics of massive manganese oxide electrode." Electrochimica Acta **24**(4): 357-362.

Murphy, E. and F. Wudl (2010). "The World of Smart Healable Polymers." Prog. Polym. Sci **35**: 223-251.

Najafpour, M. M., M. Kompany-Zareh, A. Zahraei, D. Jafarian Sedigh, H. Jaccard, M. Khoshkam, R. D. Britt and W. H. Casey (2013). "Mechanism, decomposition pathway and new evidence for self-healing of manganese oxides as efficient water oxidizing catalysts: new insights." Dalton Transactions **42**(40): 14603-14611.

Najafpour, M. M., D. J. Sedigh, B. Pashaei and S. Nayeri (2013). "Water oxidation by nano-layered manganese oxides in the presence of cerium (IV) ammonium nitrate: important factors and a proposed self-repair mechanism." New Journal of Chemistry **37**(8): 2448-2459.

Nosonovsky, M. and B. Bhushan (2009). "Thermodynamics of surface degradation, self-organization and self-healing for biomimetic surfaces." Philosophical Transactions of the Royal Society A: Mathematical, Physical and Engineering Sciences **367**(1893): 1607-1627.

Olugebefola, S., A. Aragón, C. Hansen, A. Hamilton, B. Kozola, W. Wu, P. Geubelle, J. Lewis, N. Sottos and S. White (2010). "Polymer microvascular network composites." Journal of composite materials **44**(22): 2587-2603.

Potier, F., A. Guinault, S. Delalande, C. Sanchez, F. Ribot and L. Rozes (2014). "Nano-building block based-hybrid organic–inorganic copolymers with self-healing properties." Polymer Chemistry **5**(15): 4474-4479.

Rehr, J. J., J. J. Kas, M. P. Prange, A. P. Sorini, Y. Takimoto and F. Vila (2009). "Ab initio theory and calculations of X-ray spectra." Comptes Rendus Physique **10**(6): 548-559.

Risch, M., V. Khare, I. Zaharieva, L. Gerencser, P. Chernev and H. Dau (2009). "Cobalt− oxo core of a water-oxidizing catalyst film." Journal of the American Chemical Society **131**(20): 6936-6937.

Risch, M., K. Klingan, F. Ringleb, P. Chernev, I. Zaharieva, A. Fischer and H. Dau (2012). "Water oxidation by electrodeposited cobalt oxides - role of anions and redox-inert cations in structure and function of the amorphous catalyst." ChemSusChem **5**(3): 542-549.

Risch, M., F. Ringleb, M. Kohlhoff, P. Bogdanoff, P. Chernev, I. Zaharieva and H. Dau (2015). "Water oxidation by amorphous cobalt-based oxides: in situ tracking of redox transitions and mode of catalysis." Energy & Environmental Science **8**(2): 661-674.

Rule, J. D., E. N. Brown, N. R. Sottos, S. R. White and J. S. Moore (2005). "Wax-protected catalyst microspheres for efficient self-healing materials." Advanced Materials **17**(2): 205-208.

Schäfer, H., S. Sadaf, L. Walder, K. Kuepper, S. Dinklage, J. Wollschläger, L. Schneider, M. Steinhart, J. Hardege and D. Daum (2015). Stainless steel made to rust: A robust water-splitting catalyst with benchmark characteristics.

Singh, A., S. L. Chang, R. K. Hocking, U. Bach and L. Spiccia (2013). "Highly active nickel oxide water oxidation catalysts deposited from molecular complexes." Energy & Environmental Science **6**(2): 579-586.

Smith, R., C. Pasquini, S. Loos, P. Chernev, K. Klingan, P. Kubella, M. Reza Mohammadi, D. González-Flores and H. Dau (2018). Geometric distortions in nickel (oxy)hydroxide electrocatalysts by redox inactive iron ions.

Surendranath, Y., M. W. Kanan and D. G. Nocera (2010). "Mechanistic studies of the oxygen evolution reaction by a cobalt-phosphate catalyst at neutral pH." Journal of the American Chemical Society **132**(46): 16501-16509.

Ullman, A. M., C. N. Brodsky, N. Li, S.-L. Zheng and D. G. Nocera (2016). "Probing edge site reactivity of oxidic cobalt water oxidation catalysts." Journal of the American Chemical Society **138**(12): 4229-4236.

Wang, L., J. Geng, W. Wang, C. Yuan, L. Kuai and B. Geng (2015). "Facile synthesis of Fe/Ni bimetallic oxide solid-solution nanoparticles with superior electrocatalytic activity for oxygen evolution reaction." Nano Research **8**(12): 3815-3822.

Winkler, J. R. and H. B. Gray (2011). Electronic structures of oxo-metal ions. Molecular Electronic Structures of Transition Metal Complexes I, Springer**:** 17-28.

Wool, R. P. (2008). "Self-healing materials: a review." Soft Matter **4**(3): 400-418.

Youngblood, J. P. and N. R. Sottos (2008). "Bioinspired materials for self-cleaning and self-healing." Mrs Bulletin **33**(8): 732-741.

Yuan, Y., T. Yin, M. Rong and M. Zhang (2008). "Self healing in polymers and polymer composites. Concepts, realization and outlook: A review." Express Polymer Letters **2**(4): 238-250.

Zaharieva, I., D. González-Flores, B. Asfari, C. Pasquini, M. R. Mohammadi, K. Klingan, I. Zizak, S. Loos, P. Chernev and H. Dau (2016). "Water oxidation catalysis – role of redox and structural dynamics in biological photosynthesis and inorganic manganese oxides." Energy Environ. Sci. **9**: 2433-2443.

List of publications

1. H/D Isotope Effects Reveal Factors Controlling Catalytic Activity in Co-Based Oxides for Water Oxidation

Chiara Pasquini, Ivelina Zaharieva, Diego González-Flores, Petko Chernev, **Mohammad Reza Mohammadi**, Leonardo Guidoni, Rodney D. L. Smith* and Holger Dau*

J. Am. Chem. Soc.*, 2019, 141 (7), pp 2938–2948 - (Impact factor: 14.3)*

2. A mononuclear cobalt complex for water oxidation: New controversies and puzzles

Rasoul Safdari, **Mohammad Reza Mohammadi**, Małgorzata Hołyńska, Petko Chernev, Holger Dau and Mohammad Mahdi Najafpour*

*Dalton Trans.***,** *2018,47, 16668-16673 - (Impact factor: 4.1)*

3. Geometric distortions in nickel (oxy)hydroxide electrocatalysts by redox inactive iron ions

Rodney D. L. Smith*, Chiara Pasquini, Stefan Loos, Petko Chernev, Katharina Klingan, Paul Kubella, **Mohammad Reza Mohammadi,** Diego González-Flores and Holger Dau*

*Energy & Environmental Science. 2018,**11**, 2476-2485 - (Impact factor: 30)*

4. Nickel-iron catalysts for electrochemical water oxidation-redox synergism investigated by: In situ X-ray spectroscopy with millisecond time resolution.

Diego González-Flores, Katharina Klingan, Petko Chernev, Stefan Loos, **Mohammad Reza Mohammadi,** Chiara Pasquini, Kubella, Paul Kubella, Ivelina Zaharieva, Rodney D. L. Smith and Holger Dau*

*Sustainable Energy & Fuels. 2018,**2**, 1986-1994*

5. Water oxidation by a manganese–potassium cluster: Mn oxide as a kinetically dominant “true” catalyst for water oxidation

Younes Mousazade, **Mohammad Reza Mohammadi**, Petko Chernev, Rahman Bikas, Robabeh Bagheri, Zhenlun Song, Tadeusz Lis, Holger Dau and Mohammad Mahdi Najafpour*

Catal. Sci. Technol., 2018,8, 4390-4398 - (Impact factor: 5.3)

6. Spectroscopic identification of active sites for the oxygen evolution reaction on iron-cobalt oxides

Rodney D. L. Smith*, Chiara Pasquini, Stefan Loos, Petko Chernev, Katharina Klingan, Paul Kubella, **Mohammad Reza Mohammadi**, Diego Gonzalez-Flores and Holger Dau*

Nature Communications, volume 8, Article number: 2022 (2017)- (Impact factor: 12.3)

7. Water oxidation catalysis – role of redox and structural dynamics in biological photosynthesis and inorganic manganese oxides

Ivelina Zaharieva*, Diego Gonzalez-Flores, Baraa Asfari, Chiara Pasquini, **Mohammad Reza Mohammadi**, Katharina Klingan, Ivo Zizak,, Stefan Loos, Petko Chernev and Holger Dau*

Energy Environ. Sci., 2016,9, 2433-2443 - (Impact factor: 29.5)

8. Electrosynthesis of Biomimetic Manganese-Calcium Oxides for Water Oxidation Catalysis-Atomic Structure and Functionality

Diego Gonzalez-Flores, Ivelina Zaharieva, Jonathan Heidkamp, Petko Chernev, Elías Martínez-Moreno, Chiara Pasquini, **Mohammad Reza Mohammadi**, Katharina Klingan, Ulrich Gernet, Anna Fischer and Holger Dau*

ChemSusChem. 2016, volume 9, Issue 4, 379-387 - (Impact factor: 7.4)

Selbständigkeitserklärung

Hiermit versichere ich, dass die vorliegende Dissertation eigenständig und ausschließlich unter Verwendung der angegebenen Hilfsmittel angefertigt wurde. Alle Literaturquellen sind als solche kenntlich gemacht. Die vorliegende Arbeit ist in dieser oder anderer Form zuvor nicht als Prüfungsarbeit zur Begutachtung vorgelegt worden.

Berlin, den 7. March 2019

…………………………………………….
Mohammad Reza Mohammadi

Appendix

How to clean the Quartz glass?

In the following the procedure of cleaning the Quartz glass discs for TXRF analysis is described:

- Transfer of the sample carriers to a PFTE cleaning cassette
- Transfer of cleaning cassette to glass beaker (500 mL), fill with diluted cleaning solution RBS (50%), and heat in microwave for 15 minutes.
- Rinsing of washing cassette with distilled water.
- Place cleaning cassette in a 500mL glass beaker filled with nitric acid (10 %) and simmer for 2 hours on a heating plate.
- Rinse the cleaning cassette with distilled water and add 500 ml distilled water to glass beaker, heat it in a microwave for about 15 minutes at 800 W.
- Rinsing of washing cassette with Milli-Q water.
- Dry the carriers in an oven for 20 minutes at 90 °C.
- Run a blank measurement of the cleaned discs for about 180 s.
- Pipetting of 10 µL silicone solution onto the center of the quartz glass disk.
- Transfer of the quartz glass disc into the washing cassette, final drying the oven at 90 °C for 10 minutes.

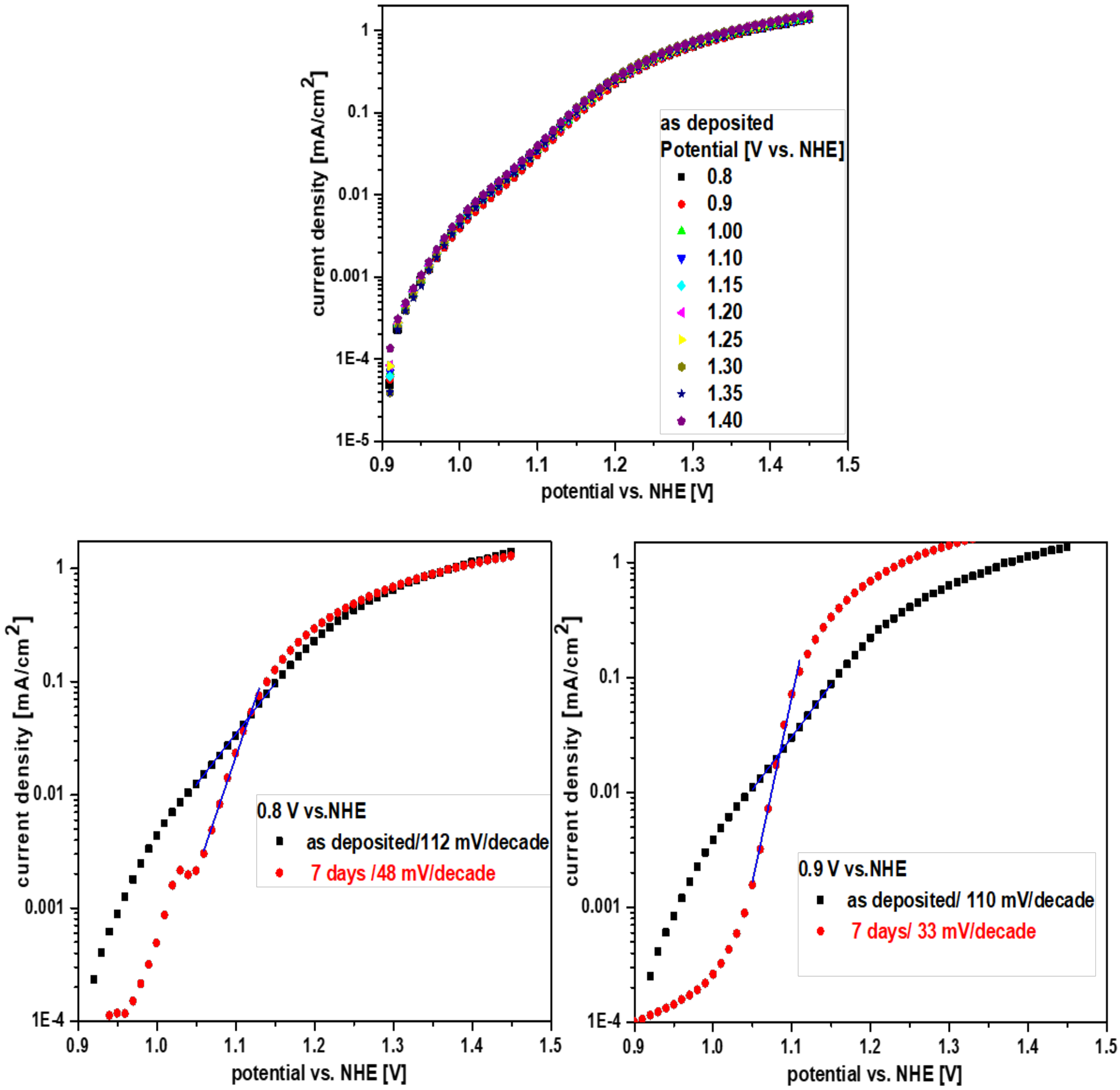

Figure S1-A. Tafel slopes of NiCats as deposited and operated for one week in **Ni-free** borate buffer (0.1 M KB(OH)$_3$ at pH 9.2) at catalytic and non-catalytic electrode potentials. Chronoamperometry measurements (potential jumps) of NiCat for one minute were carried out and the steady state currents were extracted. Potential jumps were applied from 0.9 V to 1.45 V vs. NHE with a step size of 10 mV. The steady state current after 1 min was plotted versus the potential and the linear part of the curve was fitted. The inverse of the slope was extracted as Tafel slope. The potential interval in which the current has a linear relationship with potential was from 1.05 V to 1.15 V vs. NHE.

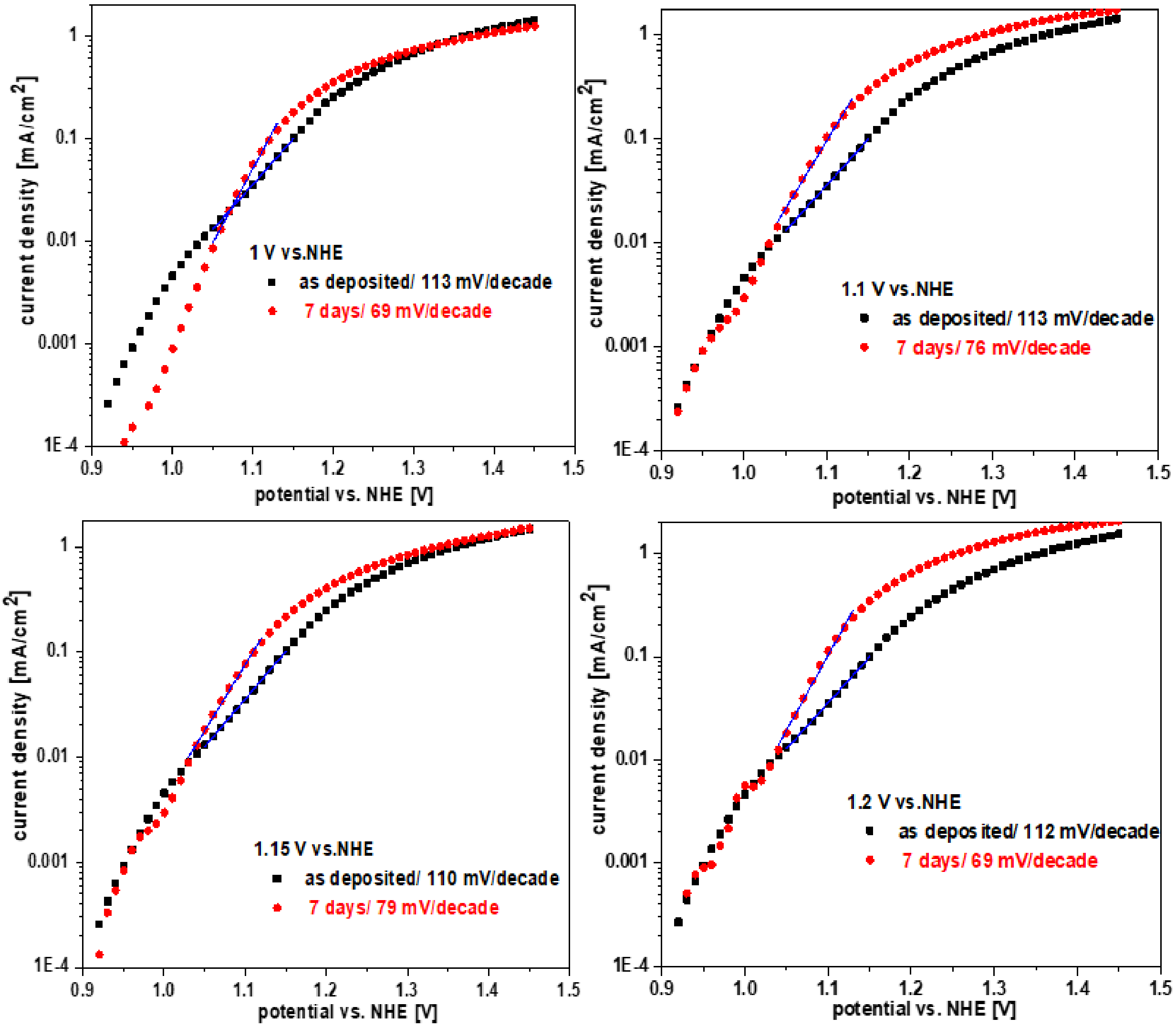

Figure S1-B. Tafel slopes of NiCats as deposited and operated for one week in **Ni-free** borate buffer (0.1 M $KB(OH)_3$ at pH 9.2) at catalytic and non-catalytic electrode potentials. Chronoamperometry measurements (potential jumps) of NiCat for one minute were carried out and the steady state currents were extracted. Potential jumps were applied from 0.9 V to 1.45 V vs. NHE with a step size of 10 mV. The steady state current after 1 min was plotted versus the potential and the linear part of the curve was fitted. The inverse of the slope was extracted as Tafel slope. The potential interval in which the current has a linear relationship with potential was from 1.05 V to 1.15 V vs. NHE.

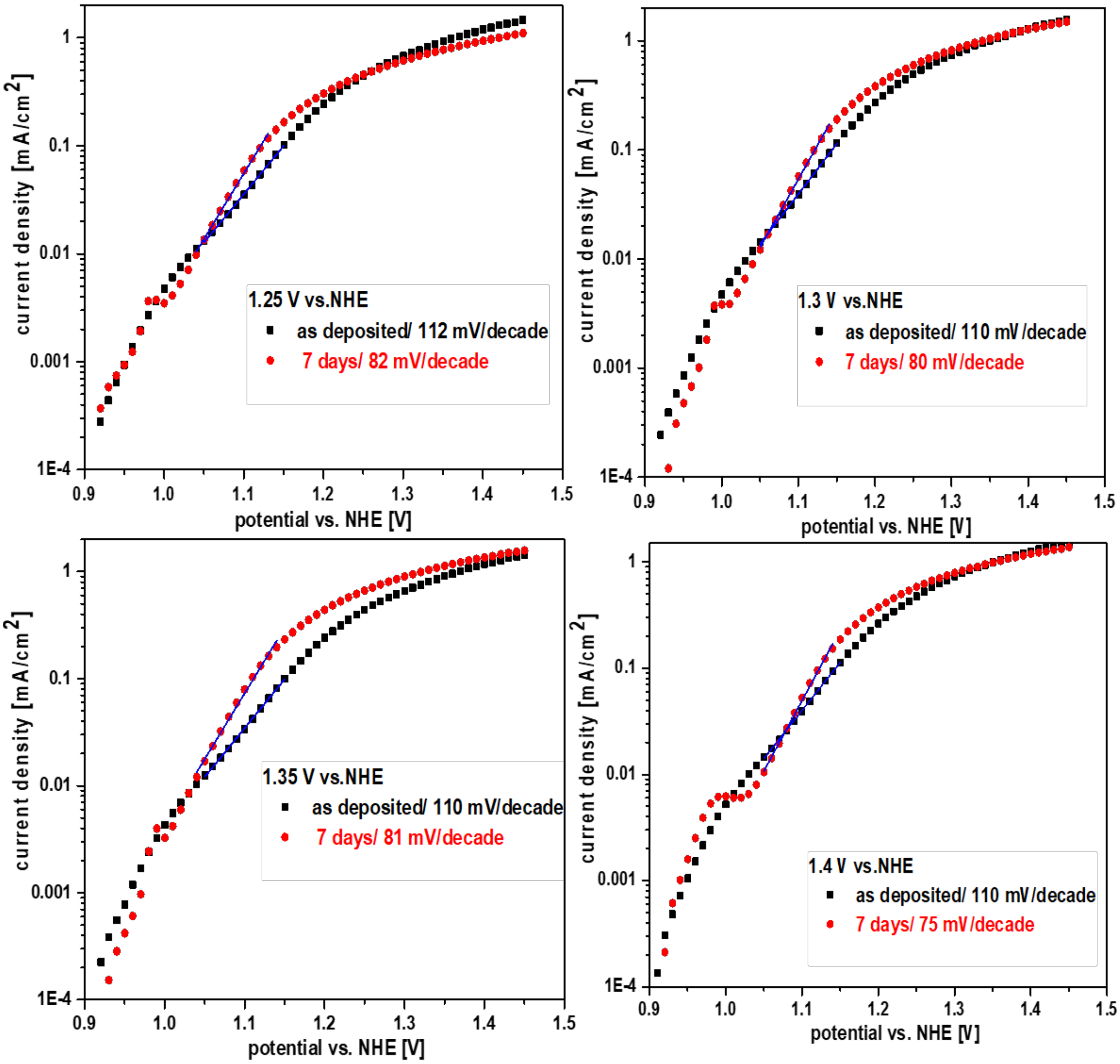

Figure S1-C. Tafel slopes of NiCats as deposited and operated for one week in **Ni-free** borate buffer (0.1 M $KB(OH)_3$ at pH 9.2) at catalytic and non-catalytic electrode potentials. Chronoamperometry measurements (potential jumps) of NiCat for one minute were carried out and the steady state currents were extracted. Potential jumps were applied from 0.9 V to 1.45 V vs. NHE with a step size of 10 mV. The steady state current after 1 min was plotted versus the potential and the linear part of the curve was fitted. The inverse of the slope was extracted as Tafel slope. The potential interval in which the current has a linear relationship with potential was from 1.05 V to 1.15 V vs. NHE.

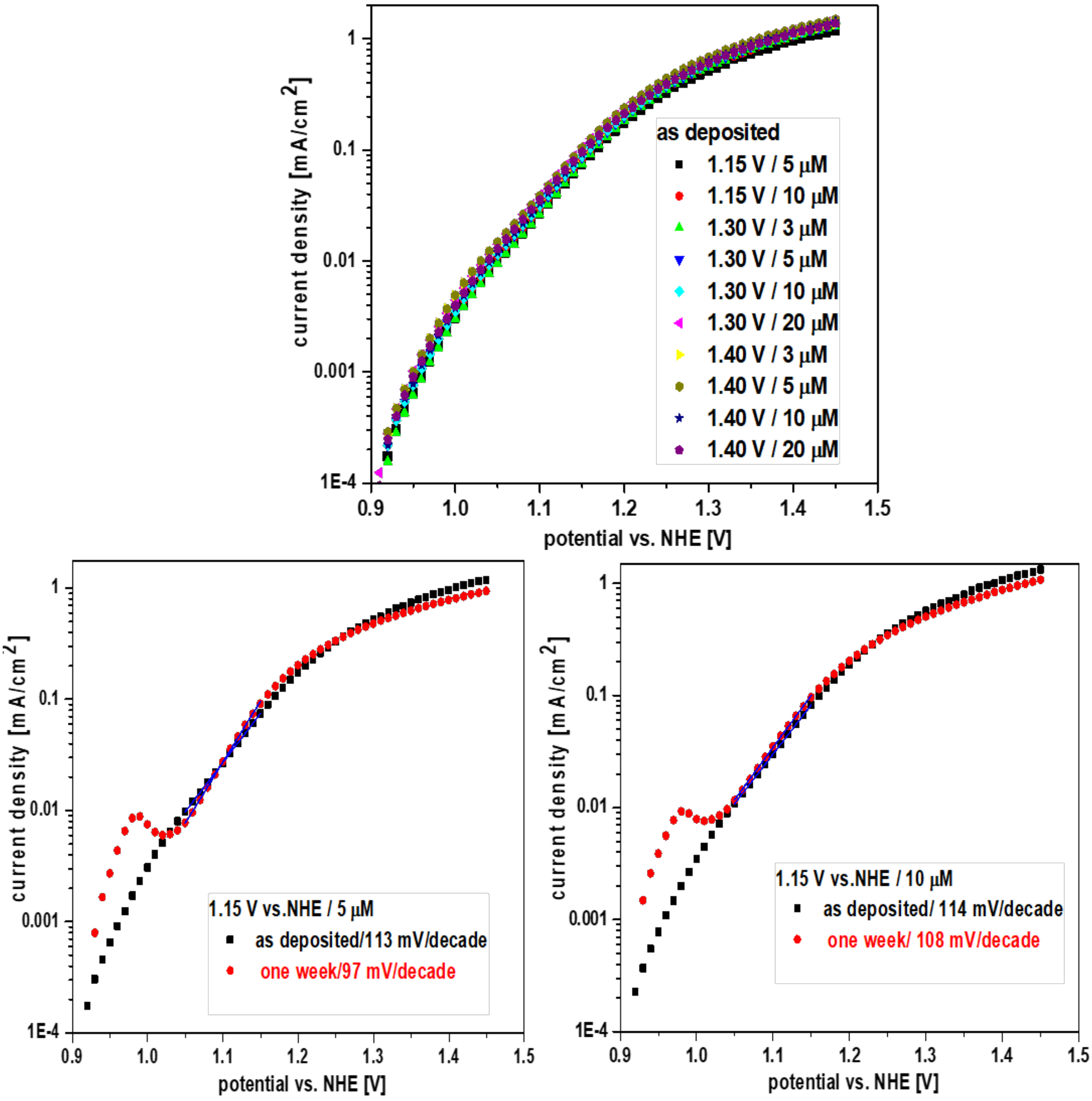

Figure S2-A. Tafel slopes of NiCats as deposited and operated for one week in **Ni-containing** borate buffer (0.1 M $KB(OH)_3$ at pH 9.2) at catalytic and non-catalytic electrode potentials. Chronoamperometry measurements (potential jumps) of NiCat for one minute were carried out and the steady state currents were extracted. Potential jumps were applied from 0.9 V to 1.45 V vs. NHE with a step size of 10 mV. The steady state current after 1 min was plotted versus the potential and the linear part of the curve was fitted. The inverse of the slope was extracted as Tafel slope. The potential interval in which the current has a linear relationship with potential was from 1.05 V to 1.15 V vs. NHE.

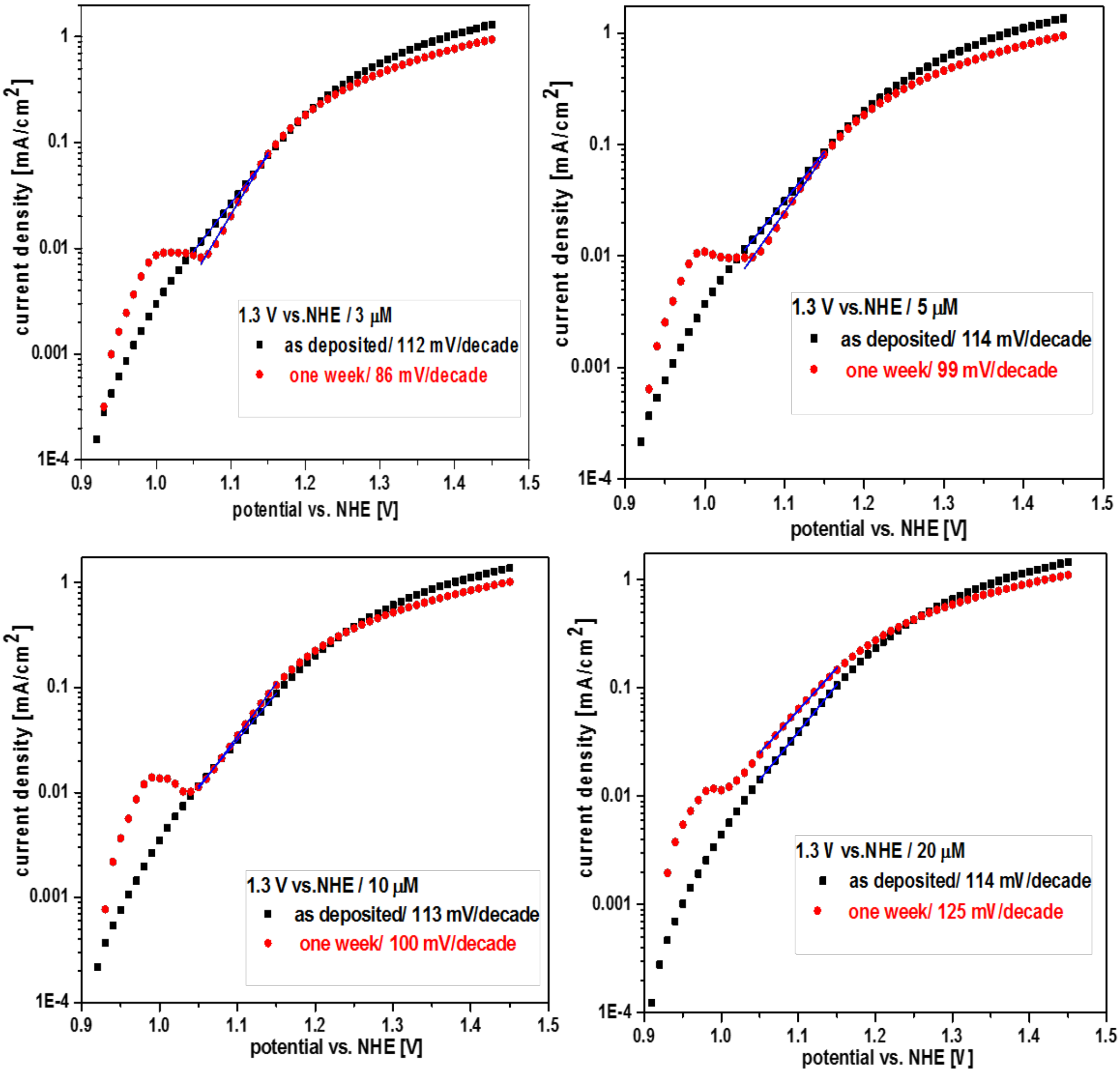

Figure S2-B. Tafel slopes of NiCats as deposited and operated for one week in **Ni-containing** borate buffer (0.1 M $KB(OH)_3$ at pH 9.2) at catalytic and non-catalytic electrode potentials. Chronoamperometry measurements (potential jumps) of NiCat for one minute were carried out and the steady state currents were extracted. Potential jumps were applied from 0.9 V to 1.45 V vs. NHE with a step size of 10 mV. The steady state current after 1 min was plotted versus the potential and the linear part of the curve was fitted. The inverse of the slope was extracted as Tafel slope. The potential interval in which the current has a linear relationship with potential was from 1.05 V to 1.15 V vs. NHE.

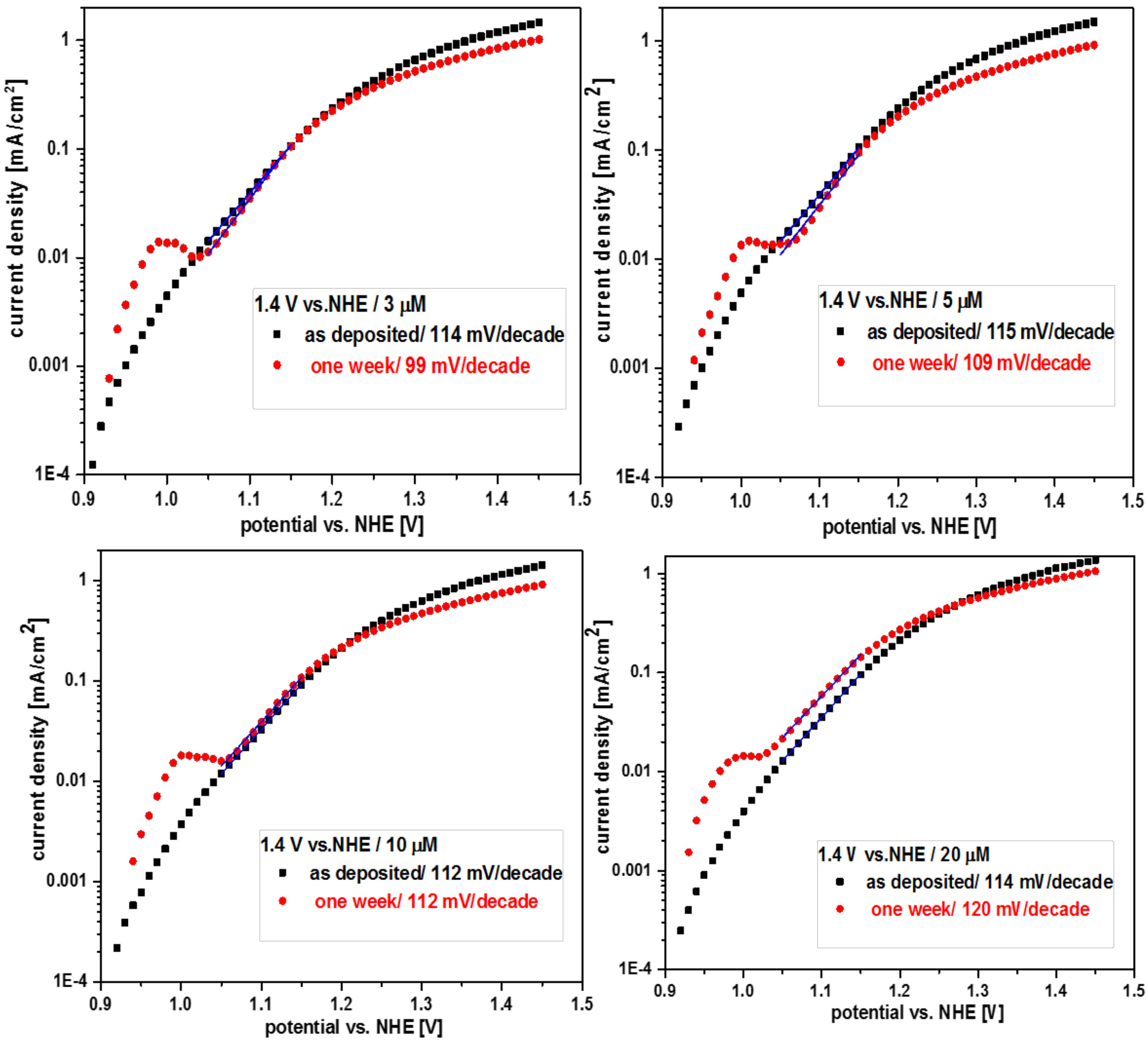

Figure S2-C. Tafel slopes of NiCats as deposited and operated for one week in and **Ni-containing** borate buffer (0.1 M KB(OH)$_3$ at pH 9.2) at catalytic and non-catalytic electrode potentials. Chronoamperometry measurements (potential jumps) of NiCat for one minute were carried out and the steady state currents were extracted. Potential jumps were applied from 0.9 V to 1.45 V vs. NHE with a step size of 10 mV. The steady state current after 1 min was plotted versus the potential and the linear part of the curve was fitted. The inverse of the slope was extracted as Tafel slope. The potential interval in which the current has a linear relationship with potential was from 1.05 V to 1.15 V vs. NHE.